Aerosols and Electrical Discharge: 1. Examination of Potential Climate Impact of Mercury Control in Electrostatic Precipitators (ESPs); 2. Instantaneous Bioaerosol Inactivation by Non-Thermal Plasma

by

Tian Xia

A dissertation submitted in partial fulfillment
of the requirements for the degree of
Doctor of Philosophy
(Environmental Engineering)
in the University of Michigan
2018

Doctoral Committee:

Research Associate Professor Herek L. Clack, Chair
Associate Professor Joseph T. Dvonch
Associate Professor Christian M. Lastoskie
Assistant Professor Krista R. Wigginton

Tian Xia

xiatian@umich.edu

ORCID iD: 0000-0002-0601-0467

Acknowledgements

I would like to express my deepest gratitude to my advisor Professor Herek L. Clack for all his teaching, understanding, mentoring and financial support throughout my PhD study. I am grateful for his constant encouragement, patience, and invaluable suggestions. This work could not be possible without his help and guidance. I would also like to thank my committee members, Professor Joseph T. Dvonch, Professor Christian M. Lastoskie, and Professor Krista R. Wigginton, for the valuable teachings, advices and comments they provided in my progress toward the doctoral degree.

My gratitude also goes to my colleagues and friends in University of Michigan with whom I had the privilege to work and spend time together. I am especially thankful to Abby Kleinheksel, Yinyin Ye and Zhong Qiao in my department for helping me in the plaque assay and RT-qPCR analysis and teaching me experimental techniques. I would also like to thank Prof. John Foster and Selman Mujovic in Nuclear Engineering and Radiological Sciences (NERS) for helping in the design and power consumption measurements of the packed-bed NTP reactor used in this research. I thank Mr. Thomas Yavaraski for all the help he provided and the department technicians for helping me on my experimental setup. I am also thankful to Minmeng Tang, Leyi Yin, Cristina Koss, Alexander Mattia and Akosua Miller for helping obtain the measurements, to Prof. Andre Boehman and Chenxi Sun for conducting the TGA measurements.

Outside of the University of Michigan, I would like to especially thank Dr. Bernard Olson, Professor Montserrat Torremorell, My Yang, Ian Marabella, and Darrick Zarling in University of Minnesota for their priceless suggestions and help in conducting the PRRSv inactivation tests. I would like to sincerely thank Eric M. Lee for his generous mentoring and guidance in my research. I would also like to thank Prof. James Hower, Dr. Kevin Henke (University of Kentucky) and Tony Bassi (DTE Energy) and the engineers at E.W. Brown and Trimble County electric generating stations of Louisville Gas & Electric and Kentucky Utilities Co. for providing plant access and assisting with fly ash collection. I am also thankful to Carl Johnson from Morehouse College for helping me in the light attenuation measurements, and Gavin McMeeking and John Walker at DMT for their technical support in operating the PAX.

Finally, I sincerely thank my parents, Jiguo Xia and Weiqing Hou, and my wife, Xudan Sha, for everything.

Table of Contents

Acknowledgements ii

List of Tables x

List of Figures xi

Abstract xv

CHAPTER I INTRODUCTION 1

1.1 Introduction to Aerosols 1

1.1.1 Definition of Aerosols 1

1.1.2 Particle Size Distribution and Size Classification 1

1.1.3 Particle Source Classification 4

1.1.4 Aerosol Optical Properties 7

1.1.5 Impact of Aerosols and Aerosol Regulations 10

1.2 PM and Mercury Emission Control from Coal-fired Power Plants 12

1.2.1 Coal-fired Power Plants and PM Emission Standard 12

1.2.2 Overview of Stationary Combustion Aerosol Control Technologies 13

1.2.3 Electrostatic Precipitators (ESPs) 18

1.2.4 Mercury control in CFPPs in conjunction with ESPs and its potential climate impact 23

1.2.5 Climate warming of black carbon (BC) and PAC 30

1.2.6 Objective of optical and physical characterization of mixed coal fly ash and particulate carbon 33

1.3 Bioaerosols and Non-thermal Plasma (NTP) 34

1.3.1 Bioaerosols and Indoor Environment 34

1.3.1.1 Introduction of Bioaerosols 34

1.3.1.2 Transmission of Pathogenic Bioaerosols 35

1.3.1.3 Bioaerosols and Indoor Environment 38

1.3.2 Atomization of bioaerosols 40

1.3.2.1 Suspending Viable Microorganisms from Bulk Liquid to Air 40

1.3.2.2 Real-time Monitoring of Atomization Rate by Light Attenuation Measurements 44

1.3.2.3 Objective of Suspending Viral Aerosols in an Airstream through Ultrasonic Atomization 45

1.3.3 Bioaerosol Inactivation and Non-thermal Plasma 46

1.3.3.1 Inactivation of Bioaerosols 46

1.3.3.2 Non-thermal Plasma (NTP) and Packed-bed Dielectric Barrier Discharge Reactor 49

1.3.3.3 Objective of Inactivation of Airborne Viruses by Packed Bed Non-Thermal Plasma 53

1.4 Dissertation Objectives 53

CHAPTER II MATERIALS AND METHODOLOGY 56

2.1 Optical and Physical Characterization of Mixed Coal Fly Ash and Particulate Carbon .. 56

2.1.1 Experimental Setup 56

2.1.2 Measurement Processes 58

2.1.3 Preliminary Testing 60

2.2 Ultrasonic Atomization of Virus Suspended in Bulk Liquid Solution 61

2.2.1 Ultrasonic Atomization of MS2 Suspended in Virus Dilution Buffer 61

2.2.1.1 Experimental Methods 61

2.2.1.4 Testing of MS2 Survival in Humidifier Reservoir during Atomization ... 64

2.2.2 Real-time Ultrasonic Atomization Rate Monitoring by Light Attenuation Measurements 65

2.2.2.1 Experimental Setup 65

2.2.2.2 Experimental Procedure 68

2.3 In-flight Inactivation of Airborne Virus by Packed Bed Non-thermal Plasma 70

2.3.1 In-flight inactivation of MS2 by Non-thermal Plasma 70

2.3.1.1 Experimental Setup 70

2.3.1.2 Non-Thermal Plasma and Reactor Design 72

2.3.1.3 Experimental Procedure 74

MS2 propagation and enumeration 76

RT-qPCR 76

Measurements of System Performance 77

2.3.2 In-flight inactivation of Porcine Reproductive & Respiratory Syndrome (PRRS) virus by Non-thermal Plasma 78

2.3.2.1 Experimental Apparatus 78

2.3.2.2 Experimental Procedure 80

NTP Inactivation Testing Procedure 80

PRRS Virus Preparation, Aerosolization and Collection 82

Quantitative RT-PCR (RT-qPCR) 83

Sample Titration 83

Testing the Effects of Liquid Accumulation on NTP Performance 83

CHAPTER III OPTICAL AND PHYSICAL CHARACTERIZATION OF MIXED COAL FLY ASH AND PARTICULATE CARBON 85

3.1 Short review on the research background and methodology 85

3.2 Preliminary Test Results of the Fluidized Bed 86

3.3 Optical Characterization of Combustion-Generated Soot 89

3.4 Physical and Optical Characterization of FA-PAC Admixtures 90

3.4.1 Physical characterization of FB emissions 90

3.4.2 Optical Characterization of FB emissions 94

3.5 Comparison with Other Research 96

3.6 Estimation of PAC emissions from CFPPs 98

3.7 Conclusions, Limitations and Future Work 100

CHAPTER IV SUSPENDING VIRAL AEROSOLS IN AN AIRSTREAM THROUGH ULTRASONIC ATOMIZATION 102

4.1 Ultrasonic Atomization of Virus Suspended in Bulk Liquid Solution 102

4.1.1 Short review on the research background and methodology 102

4.1.2 Performance of the humidifier 104

4.1.3 MS2 inactivation during the atomization process 106

4.1.4 Performance of MS2 Atomization 107

4.1.5 Conclusions and Future Work 109

4.2 Real-time in situ Monitoring of Ultrasonic Atomization Rate by Light Attenuation Measurements 111

4.2.1 Short review on the research background and methodology 111

4.2.2 Repeatability assurance 112

4.2.3 Real-time *in situ* measurement of atomization rate 113

4.2.4 MS2 Survival during Laser Exposure 117

4.2.5 Conclusion and Future Work 119

CHAPTER V INACTIVATION OF AIRBORNE VIRUSES BY A PACKED BED NON-THERMAL PLASMA REACTOR 120

5.1 In-flight Inactivation of MS2 by Non-thermal Plasma 120

5.1.1 Short review on the research background and methodology 120

5.1.2 Sampling Train Operating Conditions 122

5.1.3 MS2 Inactivation 124

5.1.4 Ozone Generation by the NTP Reactor 129

5.1.5 Conclusion and Future Work 132

5.2 In-flight Inactivation of PRRSv by Non-thermal Plasma 133

5.2.1 Short review on the research background and methodology 133

5.2.2 Droplet Size Distribution 134

5.2.3 PRRSv Inactivation by NTP 137

5.2.4 Conclusion and Future Work 144

CHAPTER VI CONCLUSIONS AND FUTURE WORK 146

6.1 Conclusions 146

6.1.1 Optical and Physical Characterization of Mixed Coal Fly Ash and Particulate Carbon 147

6.1.2 Suspending Viral Aerosols in an Airstream through Ultrasonic Atomization 148

6.1.3 Inactivation of Airborne Viruses by A Packed Bed Non-Thermal Plasma Reactor 149

6.2 Future Work 150

Appendix 155

Bibliography 158

List of Tables

Table 1. 1 China, EU and US CFPP Emission Standards (ChinaFAQs, 2012) 13

Table 3. 1 Calculated MAC and MSC of the combustion generated soot in six tests. 89

Table 5. 1 Summary of PRRSv inactivation efficiency results, normalized by either reactor-off tests or qPCR analysis, at two air flow rates and four NTP voltage settings. 139

List of Figures

Figure 1. 1 Source Appointment of the US 2014 PM_{10} and $PM_{2.5}$ Emissions (USEPA, 2018). 5

Figure 1. 2 Source Appointment of Mobile Black Carbon Emissions in the US (Kuklinski, 2013). 5

Figure 1. 3 Summary and Predictions of PM Control Applications in CFPPs in the US (Bielawski et al., 2013). 17

Figure 2. 1 Experimental setup for the inactivation of viral aerosols (Plotted by Eric M. Lee). 64

Figure 2. 2 Experimental setup for the real-time atomization rate monitoring system. 66

Figure 2. 3 Experimental setup for examining inactivation of viral aerosols by the NTP reactor (Plotted by Eric M. Lee). 72

Figure 2. 4 Schematic of the DBD packed-bed non-thermal plasma reactor (Plotted by Eric M. Lee)..... 73

Figure 2. 5 Schematic of the small-scale wind tunnel setup at Univ. of Minnesota with the NTP reactor mounted in the middle test section. One OPC is in dashed box since only one OPC was applied in this study and was switched between upstream and downstream sampling probes..... 80

Figure 3. 1 Preliminary B_{abs} readings of the emissions from seven different bad mixtures. 87

Figure 3. 2 PAX measurement results of the combustion-generated soot during the first three tests. 90

Figure 3. 3 Mass loading measurement results of the FB emissions from four bed material admixtures. 91

Figure 3. 4 TGA test results of emissions from three different FB materials. 92

Figure 3. 5 SEM images of the particles collected from the FB emission (a) without and (b) with PAC mixed in the bed. 93

Figure 3. 6 Correlation of the obtained MSC and MAC with particles' carbon content. 95

Figure 3. 7 Correlation of the obtained SSA with particles' carbon content. 96

Figure 3. 8 Calculated ESP emission carbon contents as function of η_{FA} assuming (a) η_{FA}-η_{PAC}=const. or (b) η_{PAC}/η_{FA}=const.. 100

Figure 4. 1 Measured performance of the humidifier. (a) Humidifier power consumption and atomization rate as a function of power levels; (b) The final RH upstream of the reactor as a function of atomization rate. 105

Figure 4. 2 Temperature increase of cold (~5℃) VDB inside the humidifier reservoir during the 60-minute atomization tests at three power settings. 106

Figure 4. 3 MS2 Inactivation in humidifier reservoir (a) without and (b) with active cooling. 107

Figure 4. 4 Estimated infectious MS2 concentrations in air stream at the humidifier outlet and the upstream impinger sampling point in seven 30-minute tests. 109

Figure 4. 5 Average V_0 for two groups of three consecutive tests at Position 2. All of these tests reported similar V_0 values and no increasing trend was observed for error bars. 113

Figure 4. 6 Real-time measurements of V/V0 at Position 1 with the consumer-grade humidifier atomizing (a) 200 ml MilliQ water at four power levels, or (b) 200 ml MilliQ + DMEM solution with four mixing ratios at power level H2. Vertical lines indicate the start of atomization. 116

Figure 4. 7 Correlation between $-\ln(V/V_0)$ and the average atomization rate for all tests at both optical bench installation positions. 117

Figure 4. 8 Survival of MS2 during 1s–300s laser exposure. The results proved that the laser radiation applied in this study would not cause detectable MS2 inactivation during up to five minutes exposure. 118

Figure 5. 1 Measured radial velocity profile downstream of the NTP reactor packed bed at different ID fan voltage levels. 122

Figure 5. 2 Change of infectious MS2 concentration in the downstream impinger with either ozone-free air (reactor off) or ozone-loaded air (reactor activated by 20kV) bubbling through the impinger liquid. 124

Figure 5. 3 Concentrations of viruses in air measured with plaque assays and RT-qPCR in the NTP reactor powered by 30kV AC supply at a 170 LPM air flow rate (*: Detection limit)..... 126

Figure 5. 4 Log-reduction of infectious MS2 in airstream due to inactivation of the packed-bed NTP reactor activated by the variable voltage amplifier at 12kV, 16kV and 20kV

(C_D and C_U represent the downstream and upstream concentrations in air, respectively). 128

Figure 5. 5 Measured ozone concentrations upstream of the ozone filter as a function of V_{pp} and air flow rate. 130

Figure 5. 6 Measured ozone concentration upstream and downstream of the single layer ozone filter with either 20 kV or 30 kV power supply at varied air flow rates. Dashed line represents ozone standard for indoor air cleaners set by the state of California (Jakober & Phillips, 2008). 132

Figure 5. 7 Average droplet size distributions both upstream and downstream of the reactor in each phase (May and August) under wind tunnel flow rate of (a) 12 cfm and (b) 5 cfm. 135

Figure 5. 8 Penetration of particles (downstream number concentration / upstream number concentration) in each OPC size bin measured at two flow rates in the two testing phases (May and August)..... 137

Figure 5. 9 Comparison of phase 1 (May) and phase 2 (August) PRRSv inactivation by NTP treatment at two air flow rates (5cfm and 12 cfm) and four voltages (12, 16, 20, and 30 kV), as compared to earlier results for MS2 phage inactivation at the similar conditions (30 kV not shown). 141

Figure 5. 10 Reduction (filtration + inactivation) of viable bacteriophage MS2 in response to 5 ml and 20 ml of DMEM added to and held within the NTP packed bed. 144

Abstract

One common technology for airstream aerosol (or particulate matter) control is through electrical discharge. Electrical discharge within a neutral gas under atmospheric conditions has two major essential applications related to either its physical or chemical properties. Devices such as electrostatic precipitators (ESPs) are widely applied to reduce stationary PM emission utilizing physical properties of electrical discharge. Separately, the chemical properties of the high voltage discharge can be utilized in several chemical processes, including bioaerosol disinfection. This dissertation study had two research focuses related to either the physical or chemical properties of electrical discharge on aerosol control.

The first study focus is on potential impact of mercury emission control by powdered activated carbon (PAC) injection to climate change due to low removal efficiency of PAC in ESPs. The injection into the flue gas of PAC is the most mature technology for controlling mercury emissions from coal combustion. However, carbonaceous particles are known to have poor capture in ESPs. Thus, the advent of mercury emissions standards for power plants has the potential for increased emissions of PAC, whose climate change impact is unclear. The study conducted the first comparative measurements of optical scattering and absorption of aerosols comprised of varying mixtures of coal combustion fly ash and PAC. A partially fluidized bed (FB) containing fly ash-PAC admixtures with varying PAC concentrations elutriates aerosol agglomerates. A photo-acoustic extinctiometer (PAX) extractively samples from the FB flow, providing measurements of optical absorption and scattering coefficients of fly ash (FA) alone

and FA-PAC admixtures. The results indicate that the increase of carbonaceous particles in the FB emissions can cause a significant linear increase of their mass absorption cross sections. Thus, widespread adoption of activated carbon injection in conjunction with ESPs has the potential to constitute a new source of light absorbing (and climate warming) particle emissions.

The second research focus is on packed-bed non-thermal plasma (NTP) discharges and its in-flight inactivation of bacteriophage MS2 and Porcine Reproductive and Respiratory Syndrome virus (PRRSv). To reduce threats of airborne infectious disease outbreaks, there exists a need for control measures that provide effective protection while imposing minimal pressure differential, where NTP can be a solution. In the first part of this study, a low-cost consumer-grade ultrasonic humidifier is proved to consistently suspend dry MS2 aerosols into a constant air flow, and the ultrasonic atomization rate can be monitored in real-time by laser-photodiode light attenuation measurements. In the second part, suspended viral aerosols in a controlled airstream were subjected to NTP exposure within a packed-bed dielectric barrier discharge reactor. Results of plaque assays for MS2 and $TCID_{50}$ (50% Tissue culture infective dose) for PRRSv showed increasing inactivation of aerosolized viruses (42% to >99%) with increasing applied voltage. No evidence showed that the lipid layer of enveloped PRRSv offered any protection against inactivation, and the virus were inactivated comparably to MS2 by the reactor. Increasing the air flow rate did not significantly impact virus inactivation effectiveness. Activated carbon based ozone filters greatly reduced residual ozone, in some cases down to background levels, while adding less than 20 Pa pressure differential to the 45 Pa differential pressure across the packed bed. The study shows promising results that the prototype packed bed NTP reactor has the

potential to reduce airborne infectious disease transmission into indoor environment without significant ozone emission and pressure drop.

CHAPTER I INTRODUCTION

1.1 Introduction to Aerosols

1.1.1 Definition of Aerosols

Aerosols, often used interchangeably with the term particulate matter (PM), refer to solid particles and liquid droplets that are suspended in a gas such as combustion flue gas or the atmosphere (Moretti, Jones, & Asia, 2012). Particulate matter is one of the common air pollutants in the world. In the lower atmosphere, aerosols are one of the major air pollutants and have caused serious environmental and public health problems in urban areas all over the world, especially recently in developing countries like China and India. In the upper atmosphere, aerosols can absorb/scatter solar radiation and affect cloud formation, thus impacting the climate system of the planet. Aerosols or particulate matter with microbial, plant or animal origin are usually defined as bioaerosols (Douwes, Thorne, Pearce, & Heederik, 2003), and aerosols without biological content or origin are often called non-biological aerosols.

1.1.2 Particle Size Distribution and Size Classification

Particle diameter is one of the crucial properties to characterize aerosols since it describes the terminal settling velocity of a particle suspended in air, determines its deposition and lifetime in the fluid, and affects particle agglomeration/coagulation, adsorption/absorption, charge accumulation, and many more behaviors. Both natural and anthropogenic aerosols are not likely to be uniform in size, or monodispersed, and it is generally the case that the particles are

polydispersed and can be represented by log-normal size distribution as a simplified model. Thus, the number/mass/volume fraction of particles are normally distributed over the logarithm of the particle diameter, and a sample distribution equation is shown below (Zender, 2008):

$$\frac{\mathrm{df}}{\mathrm{d}d_p} = \frac{1}{\sqrt{2\pi}d_p \ln(\sigma_g)} \exp[-\frac{(\ln(d_p)-\ln(CMD))^2}{2\ln(\sigma_g)^2}] \quad (1.1)$$

where f is the number/mass/volume fraction of the particles of interest, d_p is the particle size, σ_g is the geometric standard deviation, and CMD is the count median diameter. It is also not uncommon to find bimodal distributed particles, where the particle size distribution (PSD) has two log-normal peaks, especially among soot and fly ash (FA) emitted from oil or pulverized coal combustion (Clack, 2006a; Linak, Miller, & Wendt, 2000).

Particulate matter can be classified by its size, source or chemical composition, and the aerodynamic diameter of a particle is one of the major classification criteria since it describes the transport ability of the particles suspended in air. When a suspended particle is in motion relative to the fluid (air), the fluid exerts a drag force on the particle, which can be represented as

$$F_D = C_D A_p \rho_f v_r^2/2 \quad (1.2)$$

where F_D is the drag force, C_D is the drag coefficient, A_p is the projected area of particle, ρ_f is the fluid density, and v_r is the relative velocity(Cooper & Alley, 2011). When a particle is in still air with zero initial downward velocity and with only gravitational force exerted, its motion will reach steady state when the drag force equals the gravitational force, and the steady-state velocity is the terminal settling velocity of the particle with size d_p. With the definition of terminal settling velocity, one can define the aerodynamic diameter of the particle of interest, which is the diameter of the unit density (1000 kg/m^3) spherical particle that has the same terminal settling velocity as the studied particle. Expressions of the terminal settling velocity and

the particle aerodynamic diameter are shown below and detailed discussion is included in the book by Cooper and Alley (Cooper & Alley, 2011):

$$v_t = \frac{C\rho_p d_p^2}{18\mu} g \tag{1.3}$$

$$d_a = \sqrt{\frac{18\mu v_t}{C\rho_w g}} \tag{1.4}$$

where v_t is the terminal settling velocity, d_a is the aerodynamic diameter, C is the Cunningham correction factor, ρ_p is the particle density, ρ_w is the unit density (water density), μ is the fluid viscosity, and g is the gravitational acceleration. From the equations, it can be seen that both v_t and d_a are related closely to the particle size d_p. Particles that have aerodynamic diameters of 10 micrometers (μm) or less are classified as PM_{10}, or coarse particles. Particles that have aerodynamic diameters of 2.5 micrometers or less are classified as $PM_{2.5}$, or fine particles (Esworthy, 2013). Particles that are less than one micrometer in size are submicron particles, and particles less than 0.1 micrometers in size are generally called ultrafine particles. In 1961, Lapple reported detailed characteristics of particles and particle dispersoids (Lapple, 1961). According to his report, particles emitted from coal-fired power plants burning pulverized coal are generally coarse and 1-1000 μm in size; black carbon particles emitted from fossil fuel or solid fuel combustion are finer and 0.01-1 μm in size; viruses are generally 0.005-0.1 μm in size, which are among the finest natural and anthropogenic aerosols. PM_{10} generally have minutes to hours lifetime in the atmosphere, while $PM_{2.5}$ can remain suspended in air for days to weeks due to the smaller size and lower settling velocity (K.-H. Kim, Kabir, & Kabir, 2015). The fundamental principle of aerosol removal is exerting an external force to particles moving with the airstream and inducing relative motion between the particles and the fluid. When the external force is equal in magnitude and opposite in sign to the drag force described in Eq. 1.2, particles reach their

steady state drift velocity, $U_{drift,ss}$, and move relative to the fluid until collected by the designed collecting device.

1.1.3 Particle Source Classification

Based on sources, non-biological aerosols can be classified as primary particles and secondary particles. Primary particles are particles emitted directly from their sources. Once emitted, the particles may aggregate or react with other species in the atmosphere to form secondary particles (Pöschl, 2005). Primary particulate matter can be emitted from various natural and anthropogenic sources. Forest fires, volcanic activities and fugitive dust are common natural sources of PM. Anthropogenic sources include stationary sources such as power plants and industrial factories; area sources such as cooking emissions and gas station emissions; agricultural sources such as pesticides and dusts; and mobile emissions from on-road/off-road diesel/gasoline engines. Figure 1.1 summarizes US national PM emissions from various sources in 2014 (USEPA, 2018). From the figure, it can be found that the major PM_{10} sources in the US are dust (47%) and agricultural sources (28%). Fuel combustion and mobile sources only contributed to 5% and 3% of PM_{10} emissions, respectively. For $PM_{2.5}$, however, emissions from fuel combustion become a major source (14%) and mobile sources contribute to about 6% of total $PM_{2.5}$ emission. The largest source of $PM_{2.5}$ in the US are fires (32%), which mainly consists of uncontrolled wildfires and agricultural field burning. In large metropolitan regions like Beijing, power plants and large factories are generally relocated to rural areas to improve the city's air quality, and as a result, on-road vehicles, or mobile sources, become the major PM emitter. The source apportionment of mobile black carbon emissions in the US is illustrated in Figure 1.2, which reveals that on-road and off-road diesel engines are major mobile PM emitters and they account for nearly 80% of

mobile source black carbon emissions in the US (Kuklinski, 2013). An in-depth discussion on black carbon emission and their optical properties is included in Section 1.2.5. In summary, fuel combustion sources, especially coal-fired power plants, and mobile sources, especially diesel engines, are major primary anthropogenic $PM_{2.5}$ sources in the US.

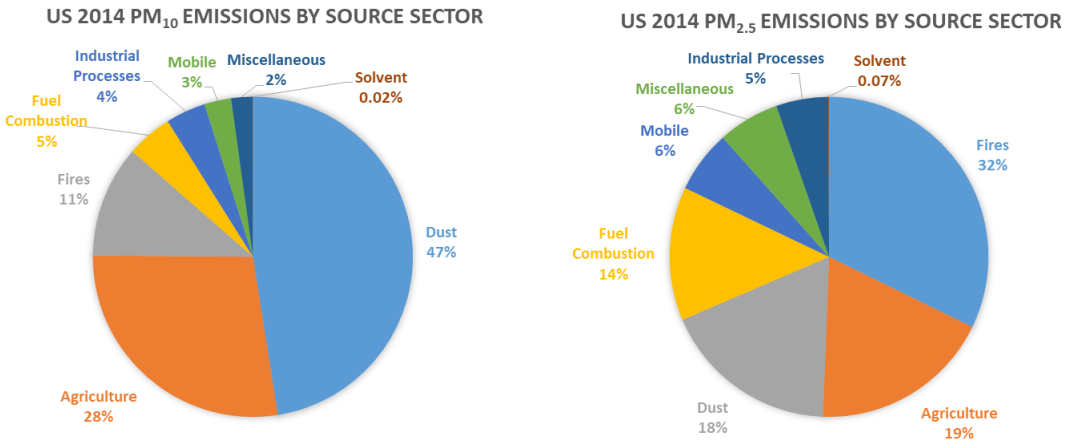

Figure 1. 1 Source Appointment of the US 2014 PM_{10} and $PM_{2.5}$ Emissions (USEPA, 2018).

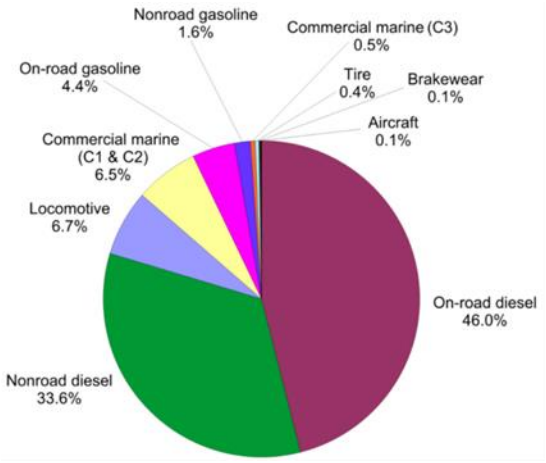

Figure 1. 2 Source Appointment of Mobile Black Carbon Emissions in the US (Kuklinski, 2013).

Secondary particulate matter are particles formed in the air mainly through photochemical reactions of primary gaseous pollutants, or precursors, and are mostly found as fine PM. SO_2, NO_x, NH_3 and volatile organic compounds (VOCs) are common precursors of secondary aerosol formation (Fuzzi et al., 2015). Secondary aerosols, especially secondary organic aerosols (SOA), are one of the dominant PM species in urban and suburban regions since two major precursors for SOA formation, NO_x and VOCs, are relatively abundant in urban areas due to intensive emission from mobile sources. While the atmospheric formation of secondary inorganic particles is relatively well understood, the process of SOA formation is poorly understood due to its complexity and precursor- and regional-dependency. Since 1960s, countless research projects have been conducted, and photochemical formation of secondary aerosols has been observed and studied both in laboratory chamber experiments (Heisler & Friedlander, 1977; Stern, Flagan, Grosjean, & Seinfeld, 1987) and on-site sampling projects (R.-J. Huang et al., 2014; Turpin, Huntzicker, Larson, & Cass, 1991; Z. Xu et al., 2015; Q. Zhang et al., 2007; X. Zhao et al., 2013), but there are still new SOA formation pathways yet to be discovered under different climate conditions and emission inventories. For example, Cheng et al. proposed that in the Northern China Plain, the aerosol water serves as a reactor where SO_2 is oxidized by NO_2, rather than common photochemical oxidant like hydroxyl radicals and ozone, to form sulfate, one of the major secondary aerosols in regional haze. This newly unfolded NO_2 pathway is mainly due to high pH in Beijing haze as compared to haze in Los Angeles and other regions(Y. Cheng et al., 2016).

Compared with non-biological aerosols, sources of bioaerosols are less well classified. Some bioaerosols, such as fungal spores and pollen, can be emitted directly from its biological source

(microbial communities and plants). Human and animal activities, such as respiration and sneezing, can release bioaerosols containing bacteria or viruses, and actually any human and animals movements can potentially re-suspend dust that have biological content into the ambient air (Hospodsky et al., 2015; Prussin & Marr, 2015; Qian, Hospodsky, Yamamoto, Nazaroff, & Peccia, 2012). Oceans, lakes and other natural water body contain high concentrations of microorganisms, and natural air-water interactions such as wave breaking and evaporation can aerosolized these waterborne microorganisms into bioaerosols (Fröhlich-Nowoisky et al., 2016). In addition to natural processes, some human controlled processes, such as wastewater treatment, waste disposal, crop and livestock production, and wood processing, can emit bioaerosols as well (Kummer & Thiel, 2008; Seedorf, 2004). Fröhlich-Nowoisky et al. gave a comprehensive review on emission and transmission of bioaerosols in the Earth system (Fröhlich-Nowoisky et al., 2016), and Prussin and Marr provided a summary on sources of bioaerosols in the built environment (Prussin & Marr, 2015). An in-depth discussion on bioaerosol emission and transmission in both outdoor and indoor environments is included in Section 1.3.1.

1.1.4 Aerosol Optical Properties

Particles suspended in air can scatter and absorb light, causing attenuation of light in the direction of its transmission, also known as light extinction. The optical property of a material is often described by its index of refraction, m, which is defined as the light velocity in a vacuum divided by light velocity in the material and is always greater than 1. For absorbing materials, a complex part is added into the refractive index to describe its absorbing property, and the overall refractive index can be express as:

$$\mathrm{m} = m' - m'ai \tag{1.5}$$

where m' is the real refractive index, and a is related to the material's absorption coefficient (b_{abs}) and wavelength of the incident light (λ) (Hinds, 2012):

$$b_{abs} = \frac{4\pi a}{\lambda} \tag{1.6}$$

Light extinction by particles in air can be described by the Beer–Lambert law:

$$I/I_0 = \exp(-\sigma_e L) \tag{1.7}$$

where I and I_0 are the attenuated light intensity and the initial unattenuated light intensity respectively, and L is the optical path length of the laser beam through the suspension (Hodkinson, 1966). σ_e [m^{-1}] is the extinction coefficient of the particle, and

$$\sigma_e = b_{abs} + b_{scat} \tag{1.8}$$

where b_{abs} and b_{scat} are the absorption and scattering coefficients of the particle, respectively. Another important parameter that characterizes optical properties of aerosols is the single scattering albedo (SSA), which is defined as the fraction of the aerosol light scattering over the total extinction (Montilla, Mogo, Cachorro, Lopez, & Frutos, 2011):

$$\text{SSA} = b_{scat}/\sigma_e = \frac{b_{scat}}{b_{abs} + b_{scat}} \tag{1.9}$$

The scattering ability of aerosols can be accurately predicted by the Mie solution to Maxwell's equations for scattering by spheres (Mie, 1908), known as Mie theory, which gives the scattered light intensity by a spherical particle at angle θ with given values of m, size parameter α, and initial light intensity I_0. Detailed illustration of the theory and its approximations can be found in the book by Hinds (Hinds, 2012). The absorption ability of aerosols, however, is harder to predict numerically. Usually the absorption coefficient or optical depth ($\tau = -\ln(I/I_0)$) of a specific aerosol species is measured experimentally, and the aerosols' imaginary refractive index, mass absorption cross sections [m^2/g] (MAC, equals to the absorption coefficient b_{abs} divided by mass

concentration of aerosol) and single scattering albedo (SSA) are calculated subsequently. Generally, aerosol absorption properties are measured at one or a few wavelengths, while the absorption usually occurs over a large wavelength range. To predict particle light absorption at other wavelengths, Ångström illustrated the spectral dependence of absorption by particles as a power law relationship:

$$MAC=K\lambda^{-Åabs} \quad (1.10)$$

where K is a constant, λ is light wavelength and $Å_{abs}$ is the absorption Ångstrom exponent (AAE)(Ångström, 1929). According to Bergstrom et al., the AAE values for carbonaceous particles are close to one for urban pollution and nearer to two for biomass smoke. The AAE values for dust particles are around 3 and perhaps only approximately fit by Eq. 1.10. In addition, AAE may be different in UV and infrared regions than in the visible spectrum (Bergstrom et al., 2007). Other research has been conducted estimating AAE values for different particle compositions (Bond, 2001; Schuster, Dubovik, & Holben, 2006).

Aerosol optical properties are important and widely applied in atmospheric visibility studies and in the development of aerosol sensing technologies. Visibility refers to the distance at which an object or light can be clearly discerned, and is directly related to light scattering and absorption of particles suspended in the atmosphere. Visibility and aerosol optical property studies have been conducted around the world in regions like Los Angeles (White & Roberts, 1977), Beijing (P. Zhao, Zhang, Xu, & Zhao, 2011) and Grand Canyon (X. Zhang, Turpin, McMurry, Hering, & Stolzenburg, 1994) where haze or smog pollution can become serious. Light extinction properties of aerosols are commonly applied in industry to continuously monitor their particulate matter emissions from smoke stacks (USEPA, 2000), and for global aerosol remote sensing

systems like Aerosol Robotic Network (AERONET) and the Moderate Resolution Imaging Spectroradiometer (MODIS) (Levy, Remer, & Dubovik, 2007). In laboratory studies, particle light scattering properties are applied by condensation particle counters to measure number size distribution of aerosols (Hinds, 2012; Sem, 2002), and the light absorption properties of black carbon (BC) are commonly used to measure mass concentration of soot emitted from a sooting flame (Yelverton, Hays, Gullett, & Linak, 2014). Detailed literature review on the light absorption properties of black carbon is included in Section 1.2.5.

1.1.5 Impact of Aerosols and Aerosol Regulations

Aerosols can have serious impacts to human health and the environment. People exposed to high concentrations of non-biological aerosols may suffer from various acute and chronic health effects, including cardiovascular and respiratory diseases as well as lung cancer, and it has been long believed that fine particles are more toxic to human than coarse particles (Harrison & Yin, 2000). In addition to $PM_{2.5}$, more and more recent research results indicate that ultrafine particles, particles less than 100 nm in diameter ($PM_{0.1}$), appear to have considerably increased toxicity per unit mass and the toxicity increases as particle size decreases (MacNee & Donaldson, 2003). As a result, ultrafine particles are now drawing more and more research interest. Aerosol health effects have been summarized and discussed in detail by the World Health Organization (WHO) (WHO, 2013) and Kim et al.(K.-H. Kim et al., 2015). Exposure to bioaerosols containing microorganisms may induce allergy, respiratory diseases and more seriously, cause outbreaks of airborne infectious diseases such as Sudden Acute Respiratory Syndrome (SARS), Middle East Respiratory Syndrome (MERS), and highly pathogenic strains of influenza. Non-biological aerosols are also believed to have several positive and negative

effects on the climate system. Some aerosols can serve as cloud condensation nuclei (CCN) and promote cloud formation in the troposphere (Ramanathan, Crutzen, Kiehl, & Rosenfeld, 2001). PM can also directly affect the process of climate change by scattering or absorbing light in the atmosphere. Aerosols like sulfate can scatter light and have a negative net radiative forcing in the solar wavelength region (Ramanathan et al., 2001), while other aerosols like black carbon (BC) are strong light absorbers that can have a positive radiative forcing effect (a deeper review is included in Section 1.2.5) (Stocker et al., 2013).

As one of the most significant air pollutants, PM concentrations in the ambient environment (in the low-level troposphere) are widely regulated in the world. The US Environmental Protection Agency (EPA) publishes its National Ambient Air Quality Standards (NAAQS) which requires that the 24-hour averaged surface level $PM_{2.5}$ concentration should not exceed 35 $\mu g/m^3$, and the same concentration of PM_{10} should not exceed 150 $\mu g/m^3$ (USEPA, 2016). The World Health Organization (WHO) 24-hour averaged regulations for $PM_{2.5}$ and PM_{10} are 25 $\mu g/m^3$ and 50 $\mu g/m^3$ respectively (Krzyzanowski & Cohen, 2008). In 2012, China updated its NAAQS with two-class standards. Class 1 requires that the 24-hour averaged ambient $PM_{2.5}$ and PM_{10} concentrations should not exceed 35 $\mu g/m^3$ and 50 $\mu g/m^3$ respectively, and for Class 2 the 24-hour averaged ambient $PM_{2.5}$ and PM_{10} concentrations should not exceed 75 $\mu g/m^3$ and 150 $\mu g/m^3$ respectively (MEP, 2012). There are no standards or guidelines published specifically for regulating bioaerosol concentrations in ambient outdoor or indoor environment.

1.2 PM and Mercury Emission Control from Coal-fired Power Plants

1.2.1 Coal-fired Power Plants and PM Emission Standard

Coal is burnt as the major heating and electricity source all over the world. In the US, the national annual consumption of coal rapidly increased since 1960s and peaked in 2005-2008 (around 1,120 million short tons per year), after which it dropped significantly possibly due to the rise of renewable energies and cheap natural gas (EIA, 2012). It is reported that in the US in 2012, the combustion of coal produced 26% of total energy, and 37% of electricity (EIA, 2014a). Developing countries like China rely more on coal for energy. EIA reported that in 2013, 66% of total primary energy consumed in China was produced by coal and 63% of China's installed electricity capacity was from coal combustion at the end of 2013 (EIA, 2016b). Coal-fired power plants (CFPPs) may emit large amounts of NOx, SO_2, PM and mercury into the atmosphere. Table 1.1 compares China, EU and the US standards for coal-fired power plant emissions (ChinaFAQs, 2012). From the table, it can be found that the US has the strictest PM emission limit (22.5 mg/m^3) and the EU limit is 50 mg/m^3. In 2011, China updated its regulations that set very low emission limits for SO_2, NOx and PM from CFPPs. The new PM emission limit presented in the table, 30 mg/m^3, is much lower than EU's standard and comparable to the US standard. This standard is complied with by all new power plants started after July 2014, and most existing plants have become in compliance with the standard as well (Moretti et al., 2012). In 2015, the Chinese government proposed its new ultra-low emission standards for CFPPs, which requires that the PM emission from CFPPs should be reduced to 5-10 mg/m^3 by 2020, while the mercury emission limit remains at 0.03 mg/m^3 (Q. Wu, 2018). Unlike particles emitted from mobile internal combustion engines, the main composition of which is black carbon (BC), PM emitted from CFPPs, known as coal fly ash (FA), generally have very low carbon content

(<1%), or loss on ignition (LOI) values, and mainly consist of SiO_2, Al_2O_3 and other metal oxides (Fisher, Chang, & Brummer, 1976; Page, Elseewi, & Straughan, 1979). This is because the furnace in power plants has been well developed to efficiently combust nearly all carbon content in fuel. Due to its low carbon composition, coal FA emission has been normally ignored or considered as scattering minerals in climate models rather than light-absorbing particles. Recently widely adopted powdered activated carbon (PAC) injection in conjunction with ESPs for mercury control from CFPPs, however, may increase the amount of carbonaceous particles emitted from the power plants and make CFPPs potentially a new source of light-absorbing particle emission (Section 1.2.4 and 1.2.5).

Table 1. 1 China, EU and US CFPP Emission Standards (ChinaFAQs, 2012)

CHINA, EU, AND U.S. COAL-FIRED POWER PLANT STANDARDS (All units mg/m³)

		China	European Union	United States	
NO_x	**New Plants**	100	500 until 12/31/2015, then 200	117	
	Existing Plants (defined in China as built 1/1/04-12/3/11) (defined in US as built after 2/28/05)	100	500 until 12/31/2015, then 200	117	
	Existing Plants (defined in China as built before 1/1/04) (defined in US as built before 2/28/05)	200	500 until 12/31/2015, then 200	160 (built between 1997-2005)	640 (built between 1978-1996)
SO_2	**New Plants**	100	200	160 (built after 2005)	
	Existing Plants (28 provinces) (four provinces with high sulfur coal)[7]	200 400	400	160 (built between 1997-2005)	640 (built between 1978-1996)
Particulates	**New and Existing Plants**	30	50, with an exception of 100 for low quality coal (eg lignite)	22.5	
Mercury	**New and Existing Plants**	0.03	0.03 (A German standard only. No EU wide standard)	**New:** 0.001 (bituminous, gangue), 0.005 (lignite) **Existing:** 0.002 (bituminous, gangue), 0.006 (lignite)	

1.2.2 Overview of Stationary Combustion Aerosol Control Technologies

Aerosol emission control from stationary sources such as coal-fired power plants have been well developed with several available and effective technologies, including cyclones, wet scrubbers,

fabric filters, and electrostatic precipitators (ESPs). Cyclones apply centripetal/centrifugal force to remove particles. Cyclones have simple design with low capital and maintenance costs, but can induce large pressure drop across the device at high flue gas flow rates in CFPPs and is generally not very effective to remove coarse and fine particles in CFPPs to meet the emission standards (Cooper & Alley, 2011). It is estimated that conventional single cyclones generally have 70-90% total aerosol removal efficiency, while the PM_{10} and $PM_{2.5}$ removal efficiencies are only 30-90% and 0-40% respectively (USEPA, 2003). New cyclone design in agricultural processing industry can increase its fly ash (11.34 μm in mass median diameter (MMD)) removal efficiency to around 95%, which is still relatively low for CFPPs and the pressure drop across the device at 3200 sfpm fluid velocity is three to five inches of H_2O (750-1250 Pa) (L. Wang, Buser, Parnell, & Shaw, 2003). For the application in CFPPs, an array of cyclones is often installed in series to achieve desired aerosol removal, while in this case the pressure drop across the system can be significant and not acceptable. In wet scrubbers, aerosols are collected by contact with co-entrained liquid droplets, which are heavier and larger in size and thus have higher drift velocities relative to the flue gas flow.. Wet scrubber may have low removal efficiencies for fine particles from the flue gas in CFPPs. Danzomo et al. showed that a spray tower scrubber system can have over 99.6% removal efficiency of particles equal or larger than 5 μm (Danzomo, Salami, Jibrin, Khan, & Nor, 2012), while another research study showed that a similar system only has 30-50% removal efficiency of fine particles. Addition of steam can promote heterogeneous condensation on aerosols and improve PM removal, but the resulting fine particle removal efficiency would still be below 90% (L. Yang et al., 2010). Wet scrubber system in CFPPs, mainly known as the wet flue gas desulfurization (FGD) system, can also have drawbacks of high water consumption and hazardous wastewater discharges. It was reported that

a wet FGD system in CFPP consumes an average of 0.06 gallon/kWh of water (Feeley III et al., 2008), which can limit wet FGD system application in regions with water scarcity. Suspended particles and trace metals in the FGD wastewater can pollute regional ground and underground water systems (Lamminen et al., 2001), and the concentrations of total suspended solid (TSS), mercury, arsenic, selenium, and nitrate/nitrite as N in the discharge of FGD wastewater are regulated by the Effluent Limitations Guidelines and Standards (ELGs) published by US EPA (Roberts, 2013). In all, wet scrubbers may not have desired removal rate of fine particles and are usually installed as the secondary PM control device at CFPPs. Fabric filters applied for aerosol removal from CFPPs, often known as baghouses, utilize filters and the retained dust layer to remove particles from flue gas through a combination of impaction, interception and diffusion effects. Its particle removal efficiency can be extremely high (>99.9%) for all particle types and sizes, and would increase during operation as more particles are collected on filter surfaces to form a dust cake and reduce overall filter porosity. The pressure drop across the device, however, is huge for the high flue gas flow rate in CFPPs and the equipment's operational and maintenance (O&M) cost is high due to the need of periodical filter replacements (Cooper & Alley, 2011; Merritt & Bush, 1997). Pressure drop, rather than removal efficiency, is the major concern in the design of baghouses. Ellenbecker and Leith varied the filtration velocity from 50-150 mm/s and reported 1.4-40.8 in of H_2O pressure drop (0.35-10.2 kPa), and the formation of dusk cake would significantly increase the pressure drop at all tested filtration velocities (Y.-H. Cheng & Tsai, 1998; Ellenbecker & Leith, 1980). In addition to stationary PM control, one of the most efficient fabric filters, high efficiency particulate air (HEPA) filters, are also widely applied for PM removal in building heating, ventilation, and air conditioning (HVAC) systems, in indoor air cleaners, and for the prevention of airborne pathogen transmission. According to the US

Department of Energy (DOE) standard, HEPA filters should have a minimum efficiency of 99.97% when tested with particles of 0.3 μm in diameter (DOE, 2015). Similar to baghouses, pressure drop across HEPA filters is significant (up to 2-6 kPa at 0.03-0.1m/s filtration velocity with up to 10 g/m^2 dust cake area density) and would increase during operation due to dust cake formation (Thomas et al., 1999).

The last common technology for PM control from stationary combustion sources is charging the aerosols by high voltage discharges and removing charged aerosols by the existing electrical field. Electrical discharge within a neutral gas under atmospheric conditions has two major essential applications related to either its physical or chemical properties. When considering the physical properties of a high voltage discharge, devices such as electrostatic precipitators (ESPs) are commonly used to collect particles or droplets from the flue gas and prevent their emission into the atmosphere. The operation of an ESP involves gas ionization by corona discharge, which enables particle charging by ion bombardment. The charged particles then migrate toward ESP collection electrodes and are held there due to electrostatic forces. Separately, the chemical properties of the high voltage discharge can be utilized in several chemical processes, including bioaerosol disinfection, where electrical discharges within a neutral gas under atmospheric conditions form a non-thermal plasma (NTP) consisting of electrons, ions, and highly reactive radicals. These reactive plasma species, together with the discharging process, can react with various airborne pathogens and achieve real-time disinfection of the air flowing through the plasma region. Details of ESP and NTP are discussed in the following sections. Figure 1.3 illustrates the PM control applications in CFPPs greater than 50MW in the US in 2012 and 2016 (Bielawski, Schmeida, White, & Internafional, 2013). From the figure, it can be found that in

2012 about 74% of CFPPs in the US chose ESPs as the PM control device and only about 20% of power plants installed baghouses. From 2012 to 2016, development of new filter materials and optimized cleaning technologies brought down the O&M cost of baghouses, and the removal of fine and ultrafine particles became increasingly stressed in the context of air pollutant emissions. As a result, Bielawski et al. predicted that the installations of baghouses would slightly increase to 24.9% during the 4-year period and the installation of ESPs would decrease by 6%. In China, it was reported that about 90% of coal-fired power plants installed ESPs as the major PM control device in 2010 (S. Wang & Hao, 2012). In 2014 over 85% of CFPPs in China installed ESPs and it was predicted that by 2020, this percentage would remain above 85% (S. Wang & Hao, 2012; Q. Wu, 2018). In India, all CFPPs were reported to have ESPs installed in 2014 (Guttikunda & Jawahar, 2014).

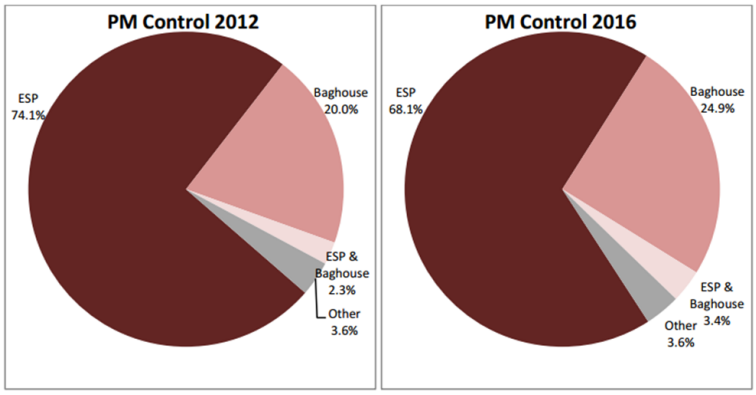

Figure 1. 3 Summary and Predictions of PM Control Applications in CFPPs in the US (Bielawski et al., 2013).

1.2.3 Electrostatic Precipitators (ESPs)

The first ESP was designed and constructed by Dr. F. G. Cottrell in 1907. In 1923 ESP was firstly installed in a coal-fired power plants(Cooper & Alley, 2011) and later became the major PM control device in CFPPs. ESPs use electric fields to charge and remove particles from a gas flow; in the context of this dissertation the gas is the flue gas produced from coal combustion. Arrays of grounded collecting plates (collection electrodes) are installed inside the ESP compartment, between which are installed separate arrays of discharge electrodes (wires) energized by high voltages (~-50kV) to induce air ionization and generate corona discharge. PM loaded gas flows through the gap between adjacent collection electrodes and the strong electric field created by the discharge electrodes negatively charge the particles in the flue gas. The charged particles, driven by the electric field, migrate towards the grounded plates (collecting surface) and are removed through impaction, leaving the cleaned flue gas exiting through the outlet. Collected particles form a dust layer on the surface of collecting electrodes. If the dust layer is too thick and/or has high resistivity, charges have difficulty reaching the grounded collecting electrode and would accumulate on the dust layer surface. As a result, high voltage can accumulate on the dust layer surface, reducing the aerosol removal efficiency of the ESPs by reducing electric field between the electrodes or creating back corona (Bäck, 2009). Low resistance particles, on the other hand, may lose their charge rapidly on the collecting electrodes and re-enter the flue gas stream. To maintain desired ESPs' removal efficiency, dust layer on the collecting electrodes has to be removed periodically. This is achieved by installing rappers to knock off collected particles from each of the collection electrodes. Knocked-off particles fall into the hopper below the compartment and be discharged as solid wastes. ESPs can achieve very high particle removal efficiency with low pressure drop across the device. Once installed in

CFPPs, the device can be operated to remove PM from the flue gas continuously, with very low O&M cost. It can handle heavy particulate loads, and have a relatively long service life. The disadvantages of ESPs include high capital cost, large space consumption, and low efficiency to remove particles with small electrical resistivity(Cooper & Alley, 2011).

PM removal efficiency in ESPs is determined by many mechanisms, including electrostatics, fluid dynamics, particle dynamics, and particle charging mechanism. In the electric field in ESPs, particles can be charged by field changing (dominant for particles with $d_p > 1$ μm) and diffusion charging (dominant for particles with $d_p < 0.1$ μm). The theoretical saturation charge of a spherical particle is given by equation 1.11:

$$q_{sat} = \frac{3\varepsilon}{\varepsilon+2}\pi d_p^2 \varepsilon_0 E_{ch} \tag{1.11}$$

where ε is the particle dielectric constant, d_p is the particle diameter, ε_0 is the constant of vacuum permittivity, and E_{ch} is the charging field strength in V/m. The electric field exerts an electrical force, F_{elec}, to charged particles. When F_{elec} equals to the fluid drag force described by Eq. 1.2, one can estimate the steady state migration velocity of the charged particle:

$$\omega_{ss} = \frac{qEC}{3\pi\mu d_p} \tag{1.12}$$

where q is the particle charge, E is the collecting electric field strength, C is the Cunningham correction factor, and μ is the fluid viscosity. By assuming 2D flow, constant gas velocity, constant electric field, infinitely fast transverse mixing, no longitudinal mixing, and no re-entrainment of collected particles, the ESPs removal efficiency can be estimated using the Deutsch-Anderson Equation:

$$\eta = 1 - exp(-\omega A/Q) \tag{1.13}$$

where η is the PM collection efficiency in ESPs, ω is the particle drift velocity determined by particle size, particle charge and the electric field strength, A is the area of the collection plate, and Q is the volumetric air flow rate through the device (Cooper & Alley, 2011). From Eq. 1.11 – 13, it can be seen that the PM removal efficiency of ESP is related to particle dielectric constant, particle size, electric field strength, and ESP electrodes design. ESPs generally have 90%-99.9% PM removal efficiency, but there is report that the device may be only 70-90% efficient in removing submicron particles, especially in the 0.1-1 μm range (McCain, Gooch, & Smith, 1975; Ylätalo & Hautanen, 1998) due to the low particle charges and high particle mobility. Zhuang et al. reported experimental and theoretical estimations of submicron and ultra-fine particle removal efficiencies by single stage and two stage ESPs. The experimental data showed 40-90% particle removal efficiencies, lower than theoretically predicted values (Zhuang, Kim, Lee, & Biswas, 2000). A similar study by Huang and Chen reported that with 26.4 kV applied voltage, particles with 0.1-1 μm diameter have penetrations (complement of collection fractions) as large as 15%, and particles smaller than 20 nm can also have significantly high penetrations (up to 40%) through two stage ESPs (S.-H. Huang & Chen, 2002).

Wet ESPs, which apply water spray or flow to clean collection electrode rather than rappers, can have higher efficiency on removal of submicron and ultrafine particles. By removing the dust layer from the collecting electrode periodically or continuously using water flow, particle re-entrainment, dust layer surface voltage build up and back corona are prevented (Altman, Offen, BUCKLEY, BUCKLEY, & RAY, 2001). In addition, due to more humid environment, the operating power in wet ESPs can be 4-20 times of the power deposited into similar dry ESPs, and the elevated discharge power improved wet ESPs removal efficiency of submicron particles.

(Altman, Offen, et al., 2001). Lin et al. showed that wet ESP with over 3.9 kV applied voltage can achieve 80-99% removal efficiency for 10-600 nm particles (G.-Y. Lin, Tsai, Chen, Chen, & Li, 2010), which is proved by the modified Deutsch-Anderson Equation proposed by the same group for predicting dry and wet ESP nanoparticle collection efficiencies (G.-Y. Lin, Chen, & Tsai, 2012). A novel pilot scale wet ESP developed by Bologa et al. showed >98% removal of particles with d_p>1 μm and 95%-98% removal of 0.3-1 μm particles with low operating voltages (10-20 kV), and low pressure drop (<200 Pa) (A. Bologa, Paur, Seifert, Wäscher, & Woletz, 2009; A. M. Bologa, Paur, Seifert, & Wascher, 2005). Chen et al. showed that by adding an upstream condensation chamber to promote particle condensational growth, the wet ESPs can achieve 99.2–99.7% removal of nanoparticles (30 nm $\leqslant d_p \leqslant$ 100 nm) (T.-M. Chen, Tsai, Yan, & Li, 2014). Jeong et al. reported that nanomaterial coating is necessary to achieve uniform water distribution over the collecting electrode surface, and the constructed pilot scale wet ESP can achieve >99% removal of sulfuric acid aerosols at 65 kV (Jeong et al., 2013). Another report by Anderlohr et al., however, showed that the non-thermal plasma generated in wet ESPs may oxidize SO_2 to SO_3 and thus increase the sulfuric acid aerosol emission (Anderlohr, Brachert, Mertens, & Schaber, 2015). The design considerations of wet ESPs are discussed in detail by Altman et al. (Altman, Buckley, & RAY, 2001). In Chinese ultra-low emission CFPPs, wet ESPs are often installed as a secondary aerosol control device downstream of ESPs to further remove sub-micron particles from the flue gas (Cui et al., 2018; C. Zheng et al., 2017). Another novel ESP technology developed most recently is low-low temperature ESPs (LLT ESPs), which applies a low-temperature gas-gas heat exchanger to reduce the flue gas temperature to 85–95 °C before entering the ESPs (Sui et al., 2016). By reducing the flue gas temperature, the electric resistivity of the dust decreased significantly to 10^{11}-10^{12} ohm-cm, which improves the aerosol

removal efficiency by the ESPs (Bäck, 2009). In addition, reducing flue gas temperature increases the ESPs breakdown field strength and gas density while reducing the flow velocity and gas viscosity, which can improve the ESPs aerosol collection efficiency as well (Sui et al., 2016). Since the operation temperature is below the acid dew point, LLT ESPs can also remove condensable compounds, such as SO_3 and polycyclic aromatic hydrocarbons (PAHs), from the flue gas by cooling and condensing the condensable compounds onto FA (Bayless, Jewmaidang, Tanneer, & Birru, 2000; X. Li et al., 2018). Qi et al. showed that the LLT ESPs installed in a 100 MW CFPP can achieve 96.5-98.2% removal of $PM_{2.5}$ and 99.85% removal of total PM. The device can also remove > 60.9% condensable particulate matter (CPM) (Qi et al., 2017). Sui et al. reported that the LLT ESPs with a high-frequency electric source installed in a 300 MW CFPP in China can achieve 98.7%, 99.5% and 99.3% removal of PM_{10}, $PM_{2.5}$ and PM_1 respectively (Sui et al., 2016). Regular ESPs can be transformed to LLT ESPs relatively easily by installing a gas-gas heat exchanger upstream, and LLT ESPs have been widely installed in Chinese CFPPs to meet the new ultra-low emission standard (C.-h. Zheng et al., 2018; C. Zheng et al., 2017).

ESPs particle removal efficiencies and mechanisms can also be estimated by computational fluid dynamics (CFD) models such as FLUENT and COMSOL Multiphysics®. The fluid flow can be calculated by Navier-Stokes equations and the electric field produced by the corona discharge are governed by the Poisson equation and charge conservation equation:

$$\nabla^2\Phi = -{}^{q}/_{\varepsilon_0} \tag{1.14}$$

$$\nabla \mathrm{q}(k_i\nabla\Phi + \mathbf{u}) = k_i\,{}^{q^2}/_{\varepsilon_0} \tag{1.15}$$

where Φ is the scalar electric potential, q is the space charge density, k_i is the ion mobility, and **u** is the fluid flow velocity field. One example of applying current continuity and Poisson equations in ESP modelling is presented in Zhao and Adamiak (L. Zhao & Adamiak, 2008). One important mechanism that needs to be considered by all ESP modelers is electrohydrodynamic (EHD) phenomena. In the ESP electric filed, gas ions driven by the field would impact otherwise neutral gas molecules, transferring momentum from the ions to the surrounding flue gas. Meanwhile, charged gas flow can modify the electric field by ion-convection effect. The interaction between electric field and fluid flow can induce electrohydrodynamic (EHD) flow. The EHD phenomena were firstly simulated by Yamamoto & Sparks (T. Yamamoto & Sparks, 1986) and Elghazaly & Castle (Elghazaly & Castle, 1987), and more simulation work can be found by Zhao and Adamiak (L. Zhao & Adamiak, 2008), Farnoosh et al. (Farnoosh, Adamiak, & Castle, 2010) and Clack (Clack, 2015). One of the most recent models by Clack shows that the EHD phenomena can accelerate the fluid by electric body forces effectively and thus increase average fluid velocities through the ESP channel with a commiserate reduction in PM removal efficiency (Clack, 2017).

1.2.4 Mercury control in CFPPs in conjunction with ESPs and its potential climate impact

Mercury (Hg) is an environmental pollutant of concern due to its tendency to cycle between soil, air, and water; its bioaccumulation within the food chain; and its toxic effects on human and wildlife health. The transportation, deposition and environmental impacts of anthropogenic mercury is discussed in detail by the United Nations Environment Programme (UNEP) (UNEP, 2013) and global researchers (Amos, Jacob, Streets, & Sunderland, 2013; Gibb & O'Leary, 2014; Sherman, Blum, Keeler, Demers, & Dvonch, 2011; H. Zhou et al., 2017). Coal-fired

power plants (CFPPs) are one of the major sources of anthropogenic mercury emissions. According to UNEP, coal combustion accounts for 24% of anthropogenic mercury emissions, which is the second largest source (UNEP, 2013). In the US, about 50% of anthropogenic mercury emission is from electric generating units (EGUs), mostly CFPPs (USEPA, 2011). In China, coal combustion is responsible for 37% of mercury emissions of which only 14% is from CFPPs and the remainder attributable to uncontrolled industrial and household burning of coal (Y. Wu et al., 2006). Anthropogenic mercury emission is regulated by several countries in the world. In 2013, the Governing Council of the UNEP agreed on the Minamata Convention on Mercury, which is a global treaty that countries voluntarily signed on to reduce their anthropogenic mercury emissions from all sources. In 2012, the US EPA finalized its Mercury and Air Toxics Standard (MATS), which requires existing CFPPs to reduce their mercury emissions by approximately 90% on average starting in 2015. Although the standard was rejected by the US Supreme Court in June, 2015 due to insufficient consideration of the costs of the regulation, most electric utilities in the US are continuing with their plans to comply with the regulation, including an estimated 30 GW of small or old units being retired (EIA, 2014b) partially due to the regulation and partially due to the rise of cheap natural gas energy. In China, a revised national emission standard for CFPPs, which took effect in 2012, limits mercury emissions from CFPPs to 0.03 mg/m^3 (MEP, 2011).

Mercury can exist in CFPP flue gas as elemental mercury (Hg^0), oxidized mercury (Hg^{2+}) and particle bonded mercury (Hg(p)). Water-soluble oxidized mercury (Hg^{2+}) can be removed by wet scrubbers, and particle bound mercury (Hg(p)) can be removed by aerosol control devices. Hg^0, however, mainly exist as mercury vapor in flue gas and is insoluble in water, and thus is difficult

to capture. During combustion of mercury-containing coal, elemental mercury is generated as Hg^0, some of which can be oxidized to Hg^{2+} downstream due to cooling and oxidative environment in pollutant control devices. Gas-phase Hg^0 in the flue gas can be oxidized homogeneously by gas-phase chlorine, a reaction that is slow and highly dependent upon available chlorine (Strivastava, 2010). Heterogeneous mercury oxidation can occur on surfaces of suspended particles (e.g. FA). It was reported that Cl adsorbed onto the surface of FA can subsequently oxidize mercury in the gaseous phase, and unburned carbon in the FA plays a significant role in this process of oxidation and adsorption of elemental mercury from the flue gas (F. Wang et al., 2016; Y. Yang et al., 2016). The catalyst used in selective catalytic reduction (SCR) system for NO_x abatement can also promote oxidization of elemental mercury in addition to reduction of NO_x (Srivastava, Hutson, Martin, Princiotta, & Staudt, 2006; Stolle, Koeser, & Gutberlet, 2014). The mercury oxidation and emission from CFPP flue gas have been extensively studied and reported by global researchers (Presto & Granite, 2006) (Meij, Vredenbregt, & Winkel, 2002; Pudasainee, Seo, Sung, Jang, & Gupta, 2017; Senior, Sarofim, Zeng, Helble, & Mamani-Paco, 2000; Stolle et al., 2014; S. Wang et al., 2010; Z.-J. Zhou et al., 2015).

Several technologies, such as coal cleaning, wet scrubbers, and sorbent injection, are available for mercury removal from conventional CFPPs. Coal cleaning removes mercury from coal prior to combustion. The method is effective for removing mercury associated with inorganic elements, but is relatively ineffective for those that have strong organic affinities, and the overall mercury removal efficiency is unlikely to exceed 70% (Pavlish et al., 2003). Wet FGD can remove up to 90% of oxidized mercury (Hg^{2+}) from flue gas by dissolving it into liquid droplets,

which are then removed by gravitational settling or collected by mist eliminators. The liquid absorption process, however, cannot remove any insoluble Hg^0 vapor as discussed above, and thus limiting the overall efficiency of the device (Pavlish et al., 2003). In addition, research has shown that removed Hg^{2+} in wet scrubber may be reduced to Hg^0 by aqueous S(IV) (sulfite and/or bisulfite) species, leading to re-emission and increase of elemental mercury downstream (Chang & Ghorishi, 2003). Among the most mature technologies that have been developed for controlling mercury emissions from CFPPs, the injection into the flue gas of powdered activated carbon (PAC) adsorbents is attractive for its low capital costs, the small footprint of each installation, and smaller ancillary impacts on other pollutants or pollutant control processes as compared to other Hg control technologies. Detailed descriptions and comprehensive discussions of PAC injection as well as other mercury control technologies can be found in several reports (Granite, Pennline, & Senior, 2015; Srivastava et al., 2006) (Strivastava, 2010). PAC particles are injected into the flue gas right upstream of the CFPPs' aerosol control device to adsorb vapor phase mercury, and the mercury-loaded PAC particles are subsequently removed from the flue gases in the downstream aerosol control device, either fabric filters or more predominately, electrostatic precipitators (ESPs). The contact time between PAC particles and the flue gas mercury is only a few seconds in ESPs, and mercury removal is limited by the short contact time. In fabric filters, however, the contact time is much longer as the PAC particles remain in the dust cake on the bag filter and keep absorbing mercury from the passing flue gas between cleaning cycles (Strivastava, 2010). Standard PAC injection can remove both Hg^0 and Hg^{2+}, but the removal efficiency is higher for Hg^{2+}. If the flue gas has low chlorine levels to oxidize Hg^0, the higher concentration of Hg^0 and relatively lower concentration of Hg^{2+} in the flue gas lead to lower removal efficiency by standard PAC and increased standard PAC injection rate to achieve

desired mercury removal. Halogenated PAC products have chemically treated surfaces designed to rapidly oxidize and adsorb Hg^0, and the injection of these chemically treated PAC increases mercury absorption capacity of each PAC particle and thus reduces required PAC injection rate (Downs & Farthing, 2007). It was reported that compared with standard PAC, which can achieve 10-15% flue gas Hg^0 removal, Cl-impregnated PAC have significantly higher, 80-90%, flue gas Hg^0 absorption (Ghorishi, Keeney, Serre, Gullett, & Jozewicz, 2002). Scala and Clack compared mercury removal efficiency by PAC injection in conjunction with either fabric filters or ESPs, and showed that while the fixed sorbent bed formed in fabric filters can promote mercury capture per unit mass of PAC, ESPs can achieve better mercury removal per unit pressure drop. Thus, ESPs for mercury removal may require higher PAC injection rate, but can lower the overall operational cost as compared with fabric filters (Scala & Clack, 2008). Clack published a series of modeling studies that numerically examined mechanisms of mercury removal through gas-particle mass transfer within ESPs (Clack, 2006b, 2006c, 2009, 2015). In 2011, the US EPA estimated that 148 GW (out of the total 318 GW) of coal combustion EGUs would install activated carbon injection (ACI) technologies in order to comply with MATS (USEPA, 2011), and according to US Energy Information Administration's (EIA) annual report, 106 GW (out of the total 280 GW coal combustion capacity) of ACI has been installed in CFPPs by 2015 (EIA, 2016a). There is no dedicated mercury emissions control technology being installed in CFPPs in China. According to Zhu et al., coal washing in China could reduce 50% of mercury emission from CFPPs and the application of SCR + ESP + wet FGD could remove 74.8% of mercury from the flue gas (Zhu et al., 2016). The new ultra-low emission standard published in China encourages CFPPs to widely install LLT ESPs and wet ESPs to meet the fine PM emission requirements, which is believed to have co-benefits of promoting mercury removal from the flue

gas. Zheng et al. illustrated that both LLT ESPs and wet ESPs can promote Hg-FA combination to form Hg(p), which can be removed at high efficiency by LLT ESPs and wet ESPs (C. Zheng et al., 2017). Zhang et al. reported that wet ESPs can generate free radicals and reactive species like O, OH, O_3, Cl and Cl_2, which can oxidize Hg^0 to Hg^{2+}, and the water soluble Hg^{2+} can be removed by the water film over the collecting electrode (Y. Zhang et al., 2017). The paper reported 29.48%–46.42% removal of Hg^0 and 53.85%–56.25% removal of Hg^{2+} by wet ESPs installed downstream of two 300-330 MW coal boilers, which are comparable to the values reported by the U.S. Department of Energy (DOE) (Reynolds, 2004). Few studies have been conducted on mercury removal in LLT ESPs. Zheng et al. illustrated that the condensation of SO_3 might offer active adsorption sites for Hg to form $HgSO_4$ on the fly ash surface, which leads to Hg removal in LLT ESPs with relatively high efficiencies (63.9-91.3%) (C.-h. Zheng et al., 2018). Although LLT ESPs and wet ESPs can reduce mercury emission from CFPPs, ACI is still believed to be a promising technology for CFPPs in China to meet more stringent mercury emission standards in future (J. Zhou, Luo, Zhu, & Fang, 2013). According to Ancora et al., 30% of CFPPs in China need to install ACI by 2030 to reproduce the mercury emission goal of MATS in the US (Ancora, Zhang, Wang, Schreifels, & Hao, 2016). The drawback of ACI is that the efficiency of PAC removal in ESPs is lower than fly ash since the electrical resistivity of PAC ($< 10^4$ ohm-cm (Espinola, Miguel, Salles, & Pinto, 1986; E. M. Lee & Clack, 2016)) is far below the range for optimal ESP removal efficiency (10^8–10^{12} ohm-cm (Calvert & Englund, 1984; Davis & Buonicore, 2000)). As a result, it would be expected that PAC would be preferentially emitted from CFPPs during the application of ACI, at a rate that is as yet unknown. In early 2000's, US Dept. of Energy funded a series of pilot-scale testing on ACI injection and the darkened particulate filters collected at the ESP outlet at Stanton Unit 1 (a 150-MW Foster

Wheeler wall-fired boiler that has been operational since 1966 and is equipped with three coal feeders and pulverizers and two cold-side ESPs in parallel (SCA = 470 ft^2/1000 afcm)) confirmed PAC emissions from the ESP during ACI (Dombrowski et al., 2008). This emerging PAC emission reduces the actual mercury removal efficiency since more Hg(p) would be emitted with PAC particles. It should be noted that compliance with MATS is only based on measured vapor phase Hg^0 and Hg^{2+} emissions, while the Hg(p) emission is not considered, thus the increased Hg(p) emission with PAC particles may potentially make compliant CFPPs emit more mercury than regulated. Further, sub-micron, black-colored PAC aerosols (which account for ~4% in total aerosol volume (Prabhu, Kim, Khakpour, Serre, & Clack, 2012)) would be expected to have optical properties similar to submicron black carbon (BC, i.e. soot, average size of 0.15-0.40 μm (Clague, Donnet, Wang, & Peng, 1999; Hitzenberger & Tohno, 2001; J. Schneider, Kirchner, Borrmann, Vogt, & Scheer, 2008)) that can form during incomplete combustions. In climate modeling, CFPPs without ACI installed were generally considered by modelers to have little contribution to BC emission. Bond et al. estimated that only 0.6% of PM emitted from pulverized coal combustors were black carbon (Bond et al., 2004), and Cao et al. reported that power generation only contributed to 0.5% of BC emission in China (Cao, Zhang, & Zheng, 2006). Clack developed estimates indicating that the contributions of CFPPs to total US anthropogenic BC emissions (i.e., excluding wildfires) could increase from less than 6% to 8% in 2020, and from less than 8% to 11% by 2030, due to the emitted PAC and concurrent decreased emissions from diesel engines during the same time period (Clack, 2012). While the percent of CFPPs adopting ACI was a primary factor in the variability of the estimates, the unknown degree to which ESPs collect PAC less efficiently than fly ash was the principal uncertainty. Another simulation study by Clack projected increase of US anthropogenic BC

emissions due to mercury control as a function of ACI installation percentage or PAC injection rate, showing that PAC injection can increase US particulate carbon emissions by tens of percent to over 150% in the worst-case scenario (Clack, 2014).

1.2.5 Climate warming of black carbon (BC) and PAC

The definition of black carbon is relatively vague. Fine BC particles, the composition of which is usually dominated by elemental carbon, are strongly light-absorbing particles generally emitted from incomplete combustions. Black refers to the color and optical property of the particles. According to Bond et al., "Black carbon is a distinct type of carbonaceous material that is formed primarily in flames, is directly emitted to the atmosphere, and has a unique combination of physical properties" (Bond et al., 2013). Other names of BC include soot, graphitic carbon, and light-absorbing carbon. Recent studies stressed the presence and importance of atmospheric brown carbon (BrC), which is generally brown in color, mainly liberated from low-temperature combustion processes such as biomass burning or lignite combustion, and contain more organic components with less strong light absorption properties (Andreae & Gelencsér, 2006). It is therefore proposed by the author that the term light-absorbing carbon (LAC) should represent the sum of BC and BrC rather than BC alone (Andreae & Gelencsér, 2006). In the US, it is estimated that BC accounted for approximately 12% of all primary $PM_{2.5}$ emissions in 2005. Among the BC emissions, 52.3% is from the transport sector and 35.3% is from open biomass burnings including wildfires (USEPA, 2012). In developing counties where coal or biomass is burned for cooking and indoor heating, domestic/residential combustion becomes a major source of BC, which accounts for about 25% of BC emission globally (USEPA, 2012). In a laboratory environment, BC is usually generated by a diffusion flame, which is a valuable tool for the study

of soot formation and measurements of BC optical properties (Dobbins, Fletcher, & Chang, 1998; Haynes & Wagner, 1981). Kirchstetter and Novakov showed that the inverted methane/air diffusion flame is stable and effective in generating BC, the emitted particles contain no organic carbon, and thus reduce uncertainties in the BC thermal and optical analysis (Kirchstetter & Novakov, 2007). The light-absorbing property of BC is commonly applied for the measurement of BC mass concentration in the flue gas or ambient air. Yelverton et al. gave a detailed and comprehensive review describing and comparing all methods for BC mass concentration measurements (Yelverton et al., 2014). One of the earliest developed instruments is the aethalometer, which collects BC on a filter and measures light attenuation through the filter and accumulated BC as an indication of BC mass concentration (Hansen, Rosen, & Novakov, 1984). In addition to light absorption, other BC concentration measurement methods include thermal-optical methods, laser-induced incandescence (LII) and photoacoustic spectroscopy. Optical, thermal-optical and photoacoustic approaches only measure light absorption by aerosol, and mass absorption cross section (MAC in m^2/g) should be estimated to yield actual BC mass concentration. The LII method, however, measures particle incandescence rather than absorption, which is proportional to BC concentration, and no MAC value has to be assumed. A relatively new instrument that was not considered by Yelverton et al. is the photoacoustic extinctiometer (PAX, Droplet Measurement Technologies, Boulder, CO), which can measure both absorption (b_{abs}) and scattering (b_{scat}) coefficients of sampled aerosols simultaneously at a single wavelength (870 nm in this study). In the PAX, the sampled flow is divided into two chambers: the absorption chamber applies photoacoustic method and measures light absorption by the suspended aerosols by a sensitive microphone, and the scattering chamber uses a reciprocal nephelometer to measure intensity of light scattered by the suspended aerosols. Recently, Deng

et al. used PAX at 870 nm to measure ambient $PM_{2.5}$ optical properties in Xiamen, China, and reported ~10 m^2/g MAC of BC (Deng et al., 2016), which is comparable with MAC estimations by other instruments (Yelverton et al., 2014).

Suspended BC in the atmosphere can influence global climate by directly absorbing light or interacting with clouds. In addition, deposited BC on snow and ice can reduce the ground reflectivity (albedo), leading to increased solar radiation absorption on the Earth's surface. The climate warming effect of atmospheric BC, commonly described by MAC, SSA and radiative forcing (i.e. climate forcing), is far less understood than that of CO_2. Bond et al. suggested a 7.5 ± 1.2 m^2/g mass absorption cross section (MAC) for black carbon at 550 nm, and a 0.2-0.3 single scattering albedo (Bond & Bergstrom, 2006). The 2013 Intergovernmental Panel on Climate Change (IPCC) report estimates the direct forcing effect of BC to be 0.05-0.8 Wm^{-2}, and illustrates that BC can have the second largest effect on climate forcing behind CO_2 (Stocker et al., 2013). BC optical and physical properties, emissions, and potential climate effects are fully summarized and discussed by the 2013 IPCC report (Stocker et al., 2013) and two outstanding reviews by Bond et al. (Bond & Bergstrom, 2006; Bond et al., 2013). It is believed that the addition of PAC emissions from CFPPs due to ACI would further increase the overall BC radiative forcing in the atmosphere unintentionally. According to the model developed by Lin et al, the submicron PAC emissions from ACI, if applied globally to CFPP particulate emissions, could cause a global warming of 2.10 mW m^{-2} at the top of atmosphere and a cooling of −2.96 mW m^{-2} at the surface (G. Lin, Penner, & Clack, 2014). In addition, comparing the warming effects of emitted CO_2 and PAC, each normalized by its respective rate of carbon input (as fuel for CO_2; as carbon in PAC for ACI), it was determined that emitted submicron PAC has eight

times larger climate forcing per unit carbon input than CO_2. These results, however, assume that the emitted PAC has the same optical properties as that of BC, while the actual optical properties of PAC are unknown. Furthermore, most simulations of BC climate forcing, including that of Lin et al., assume that emitted coal combustion fly ash (FA) is entirely mineral and entirely scattering, while in fact, fly ash varies widely in color and carbon content, and PAC injection can enhance those variations. In order to better understand the actual climate forcing potential of incidentally emitted PAC, it is necessary to better understand PAC emission rates (complement of collection rates in particulate control devices) and the optical properties of PAC, FA and PAC-FA agglomerates.

1.2.6 Objective of optical and physical characterization of mixed coal fly ash and particulate carbon

The objective of this research project is to investigate the optical and physical properties of various admixtures of coal combustion fly ash (FA) and PAC that may be emitted from coal-fired power plants employing PAC for mercury emissions control. The research is aimed to provide the first comparative measurements of optical scattering and absorption of aerosols comprised of varying mixtures of FA and PAC, in an effort to better constrain the potential climate forcing effects of emitted PAC resulting from ACI used to reduce mercury emissions. Soot is also collected and analyzed to provide a black carbon (BC) standard against whose optical properties the fly ash and PAC mixtures could be compared. A photoacoustic extinctiometer (PAX, Droplet Measurement Technologies, Boulder, CO) is used to optically characterize both the combustion soot and the effluent from a partially fluidized bed (FB) of prepared mixtures of PAC and FA samples obtained from the hoppers of power plant ESPs.

Extracted aerosol samples from the FB effluent provide the particulate mass loading measurements. Thermogravimetric analysis (TGA) is applied to evaluate the carbon content of the mixed aerosols in the FB effluent.

1.3 Bioaerosols and Non-thermal Plasma (NTP)

1.3.1 Bioaerosols and Indoor Environment

1.3.1.1 Introduction of Bioaerosols

By definition, bioaerosols are particles of biological origin or activity which may affect living things through infectivity, allergy, toxicity, and pharmacological or other processes (Cox & Wathes, 1995). Common bioaerosols include airborne viruses, bacteria, fungal species and pollens. Bioaerosols have a wide particle size range, with pollens (10-100 μm) as the largest particles and viruses (0.05-0.1 μm) as the smallest (Lapple, 1961). Reports have shown that airborne bacteria are generally 1-10 μm in size and fungal spores generally have diameters of 2-20 μm (Hospodsky et al., 2015; Qian et al., 2012). Particle size distribution and number concentrations may not be good parameters characterizing bioaerosols, especially for viruses and bacteria, since they can easily aggregate with non-biological aerosols that co-exist in the studied air volume. Górny et al. showed that the dominant bacteria in the studied indoor air is present mostly as single particles when there was no additional emission sources, while the particle size may grow due to aggregation when a smoker lived in the dwelling (Górny, Dutkiewicz, & Krysinska-Traczyk, 1999). Instead of particle size distribution measurements, culture-based methods, such as colony-forming unit (cfu) measurements and plaque assay analysis, are often applied to quantify viable bioaerosol concentration in air, and non-culture-based methods, such as electron microscopy and quantitative polymerase chain reaction (qPCR), are common analysis

quantifying the concentration of both viable and inactivated bioaerosols present in air. Advantages and disadvantages of the two types of methods are discussed by Douwes et al. (Douwes et al., 2003). Sources of bioaerosols are quite diverse, including but not limited to direct emission from biological origin, transmission in air as single or aggregated particles, emission from bodies of water through evaporation or atomization, and exhalation and resuspension by human activities. Sources of indoor bioaerosols will be discussed in a later section. Exposures to bioaerosols may lead to a wide range of health effects that are of major public concern, including infectious diseases, acute toxic effects, allergies, respiratory illnesses, and cancer. Bioaerosol health effects are comprehensively reviewed by Douwes et al. (Douwes et al., 2003) and transmission of pathogenic bioaerosols is discussed in the following section.

1.3.1.2 Transmission of Pathogenic Bioaerosols

Various bacteria, fungi and virus pathogenic species can be transmitted through air. Substantial attention from the media and public has been drawn to disease outbreaks resulting from the airborne transmission of pathogens, in part, due to perceptions that these existing threats are unseen and diffusely distributed. Diseases such as tuberculosis (TB) and influenza have a long history of confirmed airborne transmission, and recent outbreaks of respiratory diseases such as measles, sudden acute respiratory syndrome (SARS), and Middle East respiratory syndrome (MERS) have gained substantial attention as acute public health threats. A review by Tang et al. showed that the survival of aerosolized pathogens depends upon environmental conditions, such as temperature and relative humidity (RH), and these bioaerosols can be transmitted over either short (<1 m between individuals) or long (governed by air flow and survival conditions) distances in air. In addition, evaporation may reduce the size of large droplet bioaerosols to form

fine nuclei, which have longer life time suspended in air and can be transmitted over longer distances. As a result, some pathogens, which are believed to have only short range transmission in air, may occasionally cause distant outbreaks (JW Tang, Li, Eames, Chan, & Ridgway, 2006). Some air pollutants can also influence survival and transmission of airborne pathogens. As discussed above, pathogenic viruses and bacteria can aggregate with suspended fine particles, which may enable them to survive and travel longer in air flow. Bailey et al. showed that air containing trace concentrations of ozone and a cyclic monoterpene exposed to solar spectrum radiation produced substantially higher inactivation of aerosolized bacterium *micrococcus luteus* than air containing ozone alone (Bailey, Fielding, Young, & Griffith, 2007). Airborne transmission of influenza viruses has been extensively studied due to its persistent threats to public health. Study by Lowen et al. showed that transmission of influenza A virus is highly efficient at 20%-35% and 65% RH, while the efficiency reduced greatly at intermediate RH (50%) and high RH (>80%) (Lowen, Mubareka, Steel, & Palese, 2007). The results agreed well with a previous virus stability study, which reported that the survival of airborne influenza virus is maximal at low RH (20%–40%), minimal at intermediate RH (50%), and high at elevated RH (60%–80%)(Schaffer, Soergel, & Straube, 1976). More recent research efforts have shown that compared with RH, absolute humidity (AH) may constrain more on the survival and transmission of influenza virus in air (Shaman & Kohn, 2009). Air temperature can also affect influenza virus transmission efficiency, which should be mainly due to effects on the hosts rather than on bioaerosols (Lowen et al., 2007). The airborne transmission and infection control of influenza A virus are reviewed by Tellier (Tellier, 2006).

In addition to human diseases, airborne transmission of livestock diseases or zoonotic disease such as Newcastle disease, avian influenza, hoof-and-mouth disease, porcine reproductive and respiratory syndrome (PRRS), African swine flu, etc. threaten global food security since animals experience a greater degree of exposure to ambient air or ambient atmospheric conditions. This is particularly significant in the face of ongoing climate change, especially for pathogens whose efficiency of transmission through the atmosphere may change in counterintuitive ways. For example, the virus that causes PRRS (PRRS virus) is understood to be transmitted with greater efficiency through the atmosphere under cool, damp, and cloudy weather conditions (Dee et al., 2003). Thus, unlike vector-borne transmissions that become more prominent as annual average temperature increases and vector species populations expand, warmer weather with potentially greater solar radiation would likely decrease long-distance PRRS virus transmission. Livestock diseases pose significant threats to food security, agricultural industry, and public health. Foot and mouth disease is considered as the top foreign animal disease threat to US agriculture (Colby, 2013), and the 2014-2015 outbreak of highly pathogenic avian influenza in the US caused an average of 50,000 bird losses per operation for turkeys and over 1 million bird losses per operation for table-egg laying chickens where the disease was confirmed (Ramos, MacLachlan, & Melton, 2017). In the case of swine, porcine reproductive and respiratory syndrome virus (PRRSv), an enveloped virus that appeared in the US in the 1980s (Keffaber, 1989), has drawn increasing research attention due to its significant impact on pork production and ability to be transmitted in air over long ranges. It was estimated that in 2011 the outbreaks of PRRSv in the US national breeding- and growing-pig herd totally cost $664 million annually due to productivity losses, 45% of which occur in the breeding herd (Holtkamp et al., 2013). PRRSv can be released from infected pig barns and has been found in aerosols generated when

swine manure collection tanks are pumped out (Millerick-May, 2016). Once released, the virus can be transmitted in ambient air over several kilometers (up to 9.1 km as reported) from the source (Dee, Otake, Oliveira, & Deen, 2009; Otake, Dee, Corzo, Oliveira, & Deen, 2010) and can potentially cause outbreaks in distant barns. Outbreaks of PRRS in China caused great economic losses and gained public concern due to the emergence of highly pathogenic strains. In 2006, a highly pathogenic PRRS disease emerged in China, which can lead to prolonged high fever, red discoloration of the body, and blue ears associated with high mortality of infected pigs, quickly spread to 12 provinces and significantly impacted the country's pork industry (Tian et al., 2007). The highly virulent PRRSv can be characterized by the deletion of 30 amino acids in the non-structural protein 2 (NSP2) (Y. J. Zhou et al., 2008). In 2014, a novel NADC30-like strain of PRRSv emerged in China (L. Zhou et al., 2015), which was virulent to pigs but is less pathogenic than the highly virulent PRRSv discovered in 2006 (Sun et al., 2016). The clinical signs, pathogenesis, pathology, structure and immunology of PRRSv were reviewed by Done et al. (Done, Paton, & White, 1996). The history of PRRS outbreaks in China, the molecular characterization of the Chinese highly pathogenic PRRSv, and the current control status of PRRS in China were reviewed by Zhou and Yang in 2010 (L. Zhou & Yang, 2010).

1.3.1.3 Bioaerosols and Indoor Environment

Bioaerosols have drawn extensive research focus in indoor environmental studies rather than outdoor studies. Humans spend more than 90% of their time in indoor environments (Jordan Peccia & Kwan, 2016) and it was reported that the indoor concentration of biological agents is greater than the outdoor concentrations (Hospodsky et al., 2015). Major sources of airborne microorganisms in the indoor environment include humans, pets, plumbing systems, heating,

ventilation, and air-conditioning (HVAC) systems, resuspension of settled dust, indoor plants, mold, and outdoor air, as summarized and fully reviewed by Prussin and Marr (Prussin & Marr, 2015). Humans are a significant source for indoor bioaerosols. According to Lax et al., the microbiota in each studied home were identifiable by the family occupants, and after a house move, the microbial communities in the new house rapidly converged on the community carried by the family occupants (Lax et al., 2014). Outdoor bioaerosols can to some degree affect indoor bioaerosol concentration. Early studies showed that bioaerosol pollution in outdoor air can penetrate walls of houses and appear in occupational indoor environments (Herr et al., 2003). While actinomycetes are proven to be mainly generated indoors, fungal spores and a small fraction of pollen grains can penetrate from outdoor to indoor environment (T. Lee et al., 2006). A more recent study showed that about 34% of indoor fungi and 17% of indoor bacteria have outdoor sources (Hospodsky et al., 2015). Some indoor bioaerosols have been proved to have beneficial effects on human health. A study comparing Amish and Hutterites children (two US farming populations that have similar European origin but either avoid (Amish) or embrace (Hutterites) modern farming technology) showed that the prevalence of asthma and allergic sensitization was four and six times lower among the Amish Children, who are exposed to median endotoxin levels in house dust 6.8 times as high as the exposure received by Hutterites children (Stein et al., 2016). In addition, it is reported that exposure to dog-associated household dust results in protection against airway allergen challenge and induces protective effects against a variety of respiratory insults (Fujimura et al., 2014). Indoor pathogenic bioaerosols, on the other hand, can promote transmission of some infectious diseases. One transmission pathway of *Legionella* involves aerosolization of bacteria from water into air in an indoor environment during practices like showering. The SARS outbreak within the Amoy Gardens housing complex

in Hong Kong was spread between apartments in the same building by poorly designed and maintained plumbing systems, and the viruses were transported by the prevailing wind to adjacent buildings (McKinney, Gong, & Lewis, 2006; Yu et al., 2004). Bioaerosol exposure and its beneficial/pathogenic health effects in the built environment are comprehensively reviewed by Peccia and Kwan (Jordan Peccia & Kwan, 2016) and Dai et al. (Dai et al., 2017), and indoor aerosol dynamics are reviewed by Nazaroff (Nazaroff, 2016). In agricultural industry, indoor aerosol research have been mainly focused on adverse health effects of bioaerosols suspended in animal confinements on exposed workers (Thedell, Mull, & Olenchock, 1980), and prevention of infectious livestock disease outbreaks as discussed in the former section.

1.3.2 Atomization of bioaerosols

1.3.2.1 Suspending Viable Microorganisms from Bulk Liquid to Air

Studying bioaerosol transmission and the spontaneous or engineered inactivation of airborne pathogens requires suspension of the pathogen in air, which can be non-trivial. Compared with solid microorganism particles, most viruses and bacteria prepared and cultured in bulk solutions can be somewhat more easily suspended in air by a conventional spray drying process, or atomization/aerosolization process, in which the pathogen is dispersed in a volatile liquid solution, the liquid solution is atomized after which the liquid phase of the resulting droplets rapidly evaporates, leaving the viral or bacterial pathogen suspended in air along with any dissolved minerals. Widely used for such purposes are the air-jet atomizers, such as the Collison nebulizer, which uses a high velocity gas flow to shear the solution into a liquid film that breaks up into a spray. Compared with air-jet nebulization, another atomization process, ultrasonic atomization, has several advantages. Droplets produced by air-jet nebulizers are generally

polydisperse in size and have large mean diameters, while droplets produced by ultrasonic nebulizers are smaller and more monodisperse. For air-jet nebulizers, Lorenzetto and Lefebvre (Lorenzetto & Lefebvre, 1977) reported 20μm to 120μm Sauter mean diameters of droplets emitted from a plain-jet airblast atomizer atomizing various solutions, while the mean diameters of droplets generated by ultrasonic nebulizers were reported be 2μm to 6μm with relatively narrow size distributions (Barreras, Amaveda, & Lozano, 2002; Bittner & Kissel, 1999; Steckel & Eskandar, 2003). Steckel and Eskandar reported 4μm to 7μm volume mean droplet diameters with an air-jet nebulizer atomizing various solutions, but proved that when atomizing the same solution, the volume mean diameter of droplets produced by an ultrasonic nebulizer was mainly around 2μm (Steckel & Eskandar, 2003). McCallion et al. reported larger droplet mass mean diameters when the same liquid was atomized by ultrasonic nebulizer as compared to air-jet nebulizer, but proved that the span of the droplet size distribution was one to three times smaller in ultrasonic nebulization (McCallion, Taylor, Thomas, & Taylor, 1995). Smaller and more monodisperse droplets are preferred when suspending biological agents dispersed in a bulk liquid into an airstream because the droplet transportation and evaporation process is more uniform and therefore easier to predict numerically. In addition, relatively uniformly dispersed droplets lead to more uniform environmental exposure experienced by suspended pathogens in bioaerosols, which reduces variation in microorganism survival or other factors related to suspension in air of airborne pathogens. Once emitted, the small and nearly monodisperse droplet suspensions evaporate quickly, finally forming dry bioaerosols with relative uniformity of size, after which the chosen method of inactivation can be applied. Cyclones, impactors and other low-pass filtering techniques can reduce the size and polydispersity of droplet suspensions emitted from air-jet nebulizers, but in doing so these waste large fractions of the solution while not eliminating

polydispersity in the droplet suspensions. In addition to droplet size considerations, air-jet nebulizers may induce greater damage to aerosolized microorganisms. A study examining the pressure of airblast atomization in spraying beneficial microbes as organic alternative to pesticides showed that bacterial cells can be 100% damaged during air-jet atomization with 10^6 MW/m^3 energy dissipation rate (Fife, Ozkan, Derksen, & Grewal, 2006). In another research, ultrasonic nebulization was reported to have lower enzyme inactivation as compared to air-jet nebulization during the first 10 minutes (Niven, Ip, Mittelman, Prestrelski, & Arakawa, 1995).

Ultrasonic nebulization of viable bioaerosols, however, has its own disadvantages, among which heating can be a major problem. During ultrasonic atomization, the temperature of bulk liquid solution may increase significantly, causing inactivation of viruses and bacteria sensitive to temperature change. Phipps et al. (Phipps, Pharm, & Gonda, 1990) and Niven et al. (Niven et al., 1995) both reported about 20 ℃ temperature increases with ultrasonic nebulizers atomizing saline solution or enzyme stabilizing solution for 15-30 minutes, and Niven et al. also observed the inactivation effect of heating on enzyme viability. The heating problem can be mitigated by installing an active cooling system, where cooling water is directed through the bulk liquid solution in a system of tubing and extracts heat at a controlled rate, but it should be noted that some heat-conductive tubing materials, especially metals, can cause unintentional virus or bacteria inactivation in the bulk liquid. Yamamoto et al. (N. Yamamoto, Hiatt, & Haller, 1964) submerged metal cups in 50ml of water for 5 hours, and the resulting solution ("cup extract") was tested for virus inactivation. The study showed that cup extracts of aluminum, zinc, and magnesium inactivate viruses, and the inactivation is believed to result from the simultaneous action of traces of Cu^{2+} and electrolytically formed H_2O_2. Another research illustrated a 3-log

reduction of viable Phi6 on a copper surface over 60 minutes, while on a steel surface the reduction was about 1-log (J. Li & Dennehy, 2011). Another disadvantage of ultrasonic nebulization is its viable atomization efficiency. Ultrasonic atomization efficiency is mainly controlled by the piezoelectric transducer vibration frequency (Lang, 1962), but liquid viscosity, surface tension and density can also affect the process. Data reported by McCallion et al. (McCallion et al., 1995) showed that increasing liquid viscosity generally led to decreasing ultrasonic atomization rate, while the change of surface tension did not have an obvious effect on atomization rate. In many virus/bacteria aerosolization studies, buffer saline solutions, usually with tens or hundreds of millimole per liter of salts dissolved in pure water, are selected as the bulk solution being atomized (Heidelberg et al., 1997; Owen, Al-Kaysi, Bardeen, & Cheng, 2007; Turgeon, Toulouse, Martel, Moineau, & Duchaine, 2014). The addition of millimoles of salts into one liter of water should not significantly change the viscosity and surface tension of the bulk liquid (Tavana et al., 2009), and the resulting solution should be ultrasonically atomized similarly to the atomization of water. There are still cases, however, when the studied microorganism has to be suspended in minimum essential medium (MEM) or nasal secretion for aerosolization (Elazhary & Derbyshire, 1979) (Heimbuch et al., 2011; Woo, Hsu, Wu, Heimbuch, & Wander, 2010), whose viscosity and surface tension can be significantly different from properties of water and may experience lower rates during ultrasonic atomization. The change of temperature during ultrasonic atomization may change viscosity and surface tension of the bulk liquid (discussed in detail in Section 4.2.3), which can in turn affect the atomization rate. In all, it is important to have some real-time atomization rate monitoring system when ultrasonically aerosolizing virus or bacteria from bulk liquid solution into air as fine droplets, which is one objective of this dissertation research (see Section 4.2).

1.3.2.2 Real-time Monitoring of Atomization Rate by Light Attenuation Measurements

To achieve real-time *in situ* atomization rate monitoring, the most common and nondestructive method is measurement of light extinction. As a laser beam passes through a particle or droplet loaded airstream, the light intensity is attenuated due to light scattering and absorption by particles. The light attenuation or extinction is dependent on the particle number and size, thus the measurement of light extinction can be a real-time nondestructive indication of concentration and size distribution of particles suspended in the sampled airstream. In 1984, Gundel et al. (Gundel, Dod, Rosen, & Novakov, 1984) measured the attenuation (ATN) of visible light passing through black carbon (BC) samples collected on quartz-fiber filters and illustrated that ATN (≤ 200) is directly proportional to BC concentration and the relationship is independent of origins of carbonaceous particles. Another research project (Baker & Lavelle, 1984) examining particles suspended in water also proved that light attenuation is proportional to particle mass concentration, and the slope of the regression line varies systematically with the mean particle size. Szymanski and Wagner (Szymanski & Wagner, 1990) compared light attenuation measurements with conventional scattered light flux measurements in determining absolute number concentrations of fine droplets suspended in air, which proved that the light attenuation measurement is a simple and reliable method for aerosol number concentration determination and particle growth monitoring. The laser-based attenuation measurements have been comprehensively studied to examine fuel spray characteristics and size distribution in spray combustion studies. In 1976, Swithenbank et al. described a laser diagnostic technique for the measurement of droplet size distribution and showed that the technique is extremely rapid to conduct and could easily be automated to calibrate a fuel nozzle in a few seconds (Swithenbank,

Beer, Taylor, Abbot, & McCreath, 1976). Yule et al. showed that laser tomography is rapid and accurate in mapping spray structure in terms of droplet sizes and concentration, and the system can also detect spray vaporization (Yule, Seng, Felton, Ungut, & Chigier, 1982). Hirleman et al. illustrated that the particle size distribution measurements by laser scattering may have variations due to detector calibration errors and non-ideal lens effects, and provided calibration factors for the studied detectors and lenses (Hirleman, Oechsle, & Chigier, 1984). Laser scattering measurements were commonly applied to characterize size distribution of fuel sprays generated by different atomization processes (A. Lefebvre & Wang, 1987; A. Lefebvre, Wang, & Martin, 1988), and more recent studies combined laser scattering measurements with charge-coupled device (CCD) imaging to visualize the structure of the sprays (Z. Wu, Zhu, & Huang, 2006; Y.-y. Zhang, Yoshizaki, & Nishida, 2000). To calculate corresponding particle number concentrations from light attenuation data, Beer–Lambert law (Eq. 1.7) can be used even without forward scattering correction. A recent research result by Lee and Clack (E. M. Lee & Clack, 2010) illustrated that a simple *in situ* laser-photodiode system is sensitive and accurate to measure mass concentration and size distribution of suspended carbonaceous particles for detecting particle agglomeration. In industry, opacity (derived from light extinction measurement, $opacity = 1 - I/I_0$) sensors are installed as standard equipment to continuously monitor particulate matter (PM) concentrations in smoke stacks (USEPA, 2000).

1.3.2.3 Objective of Suspending Viral Aerosols in an Airstream through Ultrasonic Atomization

The objective of the present study is to describe the method and necessary conditions required to successfully use a consumer-grade ultrasonic (aka “cool mist”) air humidifier to suspend viral aerosols in flowing airstreams in the service of studying airborne pathogen inactivation; and

develop a *in situ* monitoring system measuring real-time virus solution atomization rate from the humidifier and demonstrate a simple and low cost method for *in situ* sensing of atomized bioaerosols for various bioaerosol studies. MS2 phage suspended in virus dilution buffer (VDB) was aerosolized using a consumer-grade ultrasonic humidifier, and performance of the humidifier, MS2 survival in the humidifier reservoir, and the resulting viable MS2 bioaerosol concentration suspended in the controlled air flow were examined. In addition, laser-photodiode light attenuation measurements similar to the one developed by Lee and Clack (E. M. Lee & Clack, 2010) was adopted, and Arduino, a novel open-source electronic prototyping platform, was installed as the data logger. Various virus solutions were atomized by the humidifier with the real-time atomization rate monitored by light attenuation measurements and average atomization rate estimated by measuring volume reduction in the humidifier reservoir over a certain time period. The voltage signal across the photodiode circuit was measured by the Arduino built-in voltmeter and the data were acquired and analyzed using the Arduino programming software.

1.3.3 Bioaerosol Inactivation and Non-thermal Plasma

1.3.3.1 Inactivation of Bioaerosols

Airstream disinfection and airborne pathogen inactivation have received much less attention than drinking water and wastewater treatment for waterborne pathogens, direct disease transmission through person-to-person contact, or disease transmission via vector species. Transmission of diseases such as influenza can occur through different routes including contact transmission, droplet transmission (droplets > 10 μm, e.g. sneeze droplets), and airborne transmission (bioaerosols generally < 5 μm) (JW Tang et al., 2006; Weinstein, Bridges, Kuehnert, & Hall,

2003). Short distance transmission, like direct person-to-person transmission, mainly involves contact transmission and droplet transmission, which is hard to control with engineering solutions since the transmission distance is too short and most people/animals are able to move and interact with each other freely. Facemasks can prevent droplet transmission, but the technology does not involve charged aerosols and will not be discussed in detail in this dissertation. Long range airborne transmission through outdoor air is impractical to control using engineering methods due to the large volume of the ambient air and the complexity of regional and global meteorology. Long range pathogen transmission from outdoor to indoor environment, however, is possible to control by preventing the pathogen from entering animal confinements or human occupied spaces. Some livestock such as chickens and pigs are kept in an enclosed indoor environment and have limited opportunity to directly contact outdoor air. In this case, sterilizing ventilation air can significantly reduce risks of airborne disease outbreaks. Humans, on the other hand, are usually free to enter and exit buildings and interact with other humans, which makes disinfecting ventilated air much less effective in preventing the overall airborne disease outbreaks. Instantaneous air disinfection can be beneficial in some special human indoor environment, for example passenger aircrafts and hardened military buildings, where human interactions or movements in and out are restricted.

The most commonly applied technologies to control airborne pathogens in buildings and animal confinements are the collection of bioaerosols on HEPA filters followed by UV germicidal irradiation (UVGI). The definition, efficiencies and drawbacks of HEPA filters are briefly discussed in Section 1.2.2, and the technology has been widely applied in HVAC systems to clean indoor air (R. K. Schneider, 2001). HEPA filtration has been proven to be very effective in

removal of bioaerosols from airstreams. Farnsworth et al. (Farnsworth et al., 2006) reported 96.5 ± 1.5% bacterial collection efficiency of *B. subtilis* by HEPA filtration. The study also examined HEPA filtration of three virus species, and reported no viable virus recovered from the downstream sampler. A study by Dee (Dee, 2011) found that new PRRSv outbreaks were recorded at 20% of farms with ventilation air filters installed as compared to 92% of farms without such filters in the control group. The use of HEPA filters comes with several limitations, including high filter replacement costs; high pressure drops, and the associated elevated energy consumption of the HVAC system to maintain desired ventilation rate. In the case of agricultural buildings, there are also high reconstruction costs to achieve an air-tight building envelope and eliminate potential air infiltration (Pitkin, Otake, Dee, & ACVM, 2009; Pohl, 2012). Lastly, collection of bioaerosols on HEPA filters does not actually inactivate the pathogens, which can be re-emitted into ambient air during filter replacement and disposal processes (Miaskiewicz-Peska & Lebkowska, 2012).

UV germicidal irradiation (UVGI) alone can be applied for airborne pathogen inactivation as well. Effective UV disinfection requires a sufficiently high light intensity, achieved through a combination of a number of bulbs and exposure time in a carefully designed ventilation system. UV inactivation efficiency is also to some degree influenced by the susceptibility of the pathogen (Bolashikov & Melikov, 2009). UVGI has been shown to diminish the transmission of TB between hospital wards (Riley, 1961) and prevent the spread of rubella within army barracks (Wheeler et al., 1945). The application of UVGI in indoor air disinfection is limited by the need to avoid the adverse health effects of UV on humans and livestock. In the indoor environment, UV lights can be installed in the upper regions of the room near the ceiling to avoid exposing the

occupants to UV light. The process, however, is passive in nature and can only inactivate pathogens transported by upward air currents into the UVGI treatment zone. Effectiveness of this upper-room UVGI treatment is determined by UV light intensity, air mixing conditions in the room, and vertical temperature gradients affecting upward transport of pathogens (Riley, Permutt, & Kaufman, 1971). In addition, room RH can also have significant impact on UVGI efficiency. According to Xu et al., the performance of upper-room UV irradiation is optimized at 50% RH, and degraded significantly when the relative humidity was increased from 50% to 75−90% (P. Xu et al., 2005). In many cases, UV radiation alone is not effective in instantaneous air disinfection, and is often applied in conjunction with HEPA filters: airborne pathogens are collected on filter surfaces and inactivated by UV radiation (Memarzadeh, Olmsted, & Bartley, 2010). However, UV light is unable to penetrate deeply into HEPA filters, where collected pathogens may survive and re-enter the air flow. The energy consumption of the UV system is also significant, and broken bulbs should be detected and replaced periodically. UVGI disinfection has been comprehensively reviewed by Memarzadeh et al. (Memarzadeh et al., 2010) and Kesavan and Sagripanti (Kesavan & Sagripanti, 2012). In all, UVGI and HEPA filtration both have limitations on indoor bioaerosol inactivation, and relatively novel technologies such as non-thermal plasma (NTP) can offer new solutions to this issue.

1.3.3.2 Non-thermal Plasma (NTP) and Packed-bed Dielectric Barrier Discharge Reactor

Plasma usually refers to the partially or fully ionized gas mainly consisting of electrons, ions, molecules and radicals. When sufficient voltage is applied to a background gas, free electrons in the gas are accelerated under the electric field, increasing their kinetic energy. When sufficient energy is acquired by an electron, the collision of the electron with neutral gas molecules induces

ionization of the gas molecule, emitting secondary free electrons which can cause further ionization, a process known as electron avalanche. With sufficient voltage and favorable discharging environment, electron avalanche can sustain the ionization continuously, generating plasma in the background gas (Brown, 1966). Unlike thermal plasma, which is in a state where all constituents are in thermal equilibrium, a non-thermal plasma (NTP) is always in a state of non-equilibrium where the electrons with a much lighter mass can reach higher temperatures (10^4-$2.5x10^5$ K) and attain higher kinetic energy (1-20 eV), while the rest of the NTP constituents are much heavier and remain at lower temperatures (H. H. Kim, 2004). On these bases, an NTP is also known as non-equilibrium plasma or cold plasma. NTP can be generated by different types of electrical discharge with various high voltage power sources. In terms of electrical discharge, NTP can be classified as corona discharge, dielectric barrier discharge (DBD), and ferroelectric packed-bed discharge. NTP high voltage power supply includes direct current (DC), alternating current (AC), and pulsed current supply. Dielectric barrier discharge (DBD), or silent discharge, refers to the electrical discharge through a dielectric barrier in between the discharge and ground electrode. Various materials can be selected to make the dielectric barrier, including glass, Al_2O_3, and TiO_2 (Holzer, Kopinke, & Roland, 2005). In gases at atmospheric pressure, the dominant electrical discharge mode in a DBD reactor is that of a microdischarge, which is in a form of filaments with lifespan of nanoseconds (Falkenstein & Coogan, 1997). Generally, high voltage AC supply is utilized as the power source for DBD reactors, since the changing polarity of high voltage AC supply is essential in sustaining microdischarges. Compared with a wire-plate DBD reactor, a packed-bed DBD reactor provides a more effective way of treating trace air pollutants by adding pellets in between the electrodes, and the electron-impact reactions serve as the main plasma chemistry for air pollutant

decomposition (Vandenbroucke, Morent, De Geyter, & Leys, 2011). In a packed-bed DBD reactor, dielectric pellets are very close to each other at the contact points, where the electric field becomes significantly higher than the average field between the electrodes, and as a result microdischarges and surface discharges are promoted. Electron generation takes place through microdischarges and surface discharges near the contact points, which subsequently induces the electron-impact reactions (Tu, Gallon, & Whitehead, 2011). The dielectric constant of the pellet material can significantly affect the DBD discharge scenario in a packed-bed. Ferroelectric materials, such as barium titanate ($BaTiO_3$), have high dielectric constants (2,000–10,000) and as a result lower critical breakdown voltages, which leads to more microdischarge generations at the same applied voltages (Xiao et al., 2014). Another commonly used dielectric material, Al_2O_3, has a dielectric constant of ~10. Glass beads generally have dielectric constants of 4-6, which is much lower than the dielectric constant of $BaTiO_3$ and may not be able to generate as many microdischarges as desired in some studies (Xiao et al., 2014). Kuwahara et al. added $BaTiO_3$ pellets to the previously developed DBD reactor and proved that compared with the DBD reactor alone, the DBD reactor with ferroelectric packed-bed pellets could decompose NH_3 at a much faster rate (Kuwahara, Okubo, Kuroki, Kametaka, & Yamamoto, 2011).

During the electrical discharge of an NTP, highly reactive radicals will form which can initiate the decomposition and oxidation of gaseous pollutants. It is reported that excited and ionized species and radicals formed during NTP discharge are orders of magnitude more reactive than ozone (O_3) (Xiao et al., 2014). The chemistry of NTP discharge with examples of radical reactions are summarized by Gaunt et al. (Gaunt, Beggs, & Georghiou, 2006). The use of an NTP as a chemical process is non-selective, meaning that it can be applied to treat multiple

pollutants concurrently. NTPs have been thoroughly studied for destruction of gaseous pollutants, and the radicals and excited species having been shown to destroy a wide variety of volatile organic compounds (VOCs) such as those emitted from industrial processes (Xiao et al., 2014) as well as gaseous pollutants such as nitrous and sulfurous oxides (NO_x and SO_x) emitted from combustion (McAdams, 2001). Kuwahara et al. developed a DBD reactor using polyester-laminated electrodes to evaluate the removal characteristics of odor, including NH_3 and NH_3 mixed with CH_3CHO (Kuwahara et al., 2011). Reactive plasma species, such as OH· radicals and ozone, together with the discharging process, can be toxic to various airborne pathogens, which makes NTPs a potential technology to achieve instantaneous disinfection of the airstream. NTP has already been proven to be effective for food surface disinfection (Noriega, Shama, Laca, Díaz, & Kong, 2011; Perni, Liu, Shama, & Kong, 2008) and treatment of skin diseases (Heinlin et al., 2010). NTP airstream disinfection, however, is less studied. In the NTP environment, viruses and bacteria act as charged bioaerosols suspended in the gas stream, which can in turn affect the distribution of electric fields and flow of charged species that form the foundation of NTPs. In addition, charged aerosols and gas species in the air flow may respond separately to the NTP, and may experience different chemical reactions and fluid motions during the treatment. Vase et al. constructed a dielectric barrier discharge (DBD) NTP reactor and showed an approximate 97% *E. coli* inactivation by 10-second plasma exposure at a very high air flow rate (25L/s) (Nachiket D Vaze et al., 2007). Vase et al. has proven that the synergetic action of short-lived plasma species, such as hydroxyl radicals, and plasma-generated ozone, can achieve 97% in-flight inactivation of aerosolized *E. coli*. (Vaze et al., 2010). Another research group constructed a 12 mm diameter DBD NTP device and reported >95% inactivation of bacteria and 85–98% inactivation of fungal spores with 24 W reactor energy output at 28.3 LPM

flow rate (Liang et al., 2012). Later, the same group also examined NTP inactivation of MS2 and reported over 95% MS2 airstream inactivation with 28 W reactor energy output at 12.5 LPM flow rate (Y. Wu et al., 2015).

1.3.3.3 Objective of Inactivation of Airborne Viruses by Packed Bed Non-Thermal Plasma

The objective of this research project is to develop a non-thermal plasma in-flight airstream disinfection system and contribute to the scientific understanding of generating non-thermal plasma at atmospheric pressure, and the spontaneous inactivation of airborne viruses in a plasma environment. A dielectric barrier discharge (DBD) non-thermal plasma reactor was designed and constructed. MS2 in VDB were atomized by a consumer-grade ultrasonic humidifier and PRRSv suspended in DMEM were atomized by an air-blast nebulizer. The aerosolized virus droplets were suspended into a controlled air flow passing through the packed-bed NTP reactor. Two impingers sampled the virus-loaded air flow at both upstream and downstream positions in the reactor, and the samples were subjected to plaque assay/$TCID_{50}$ analysis and quantitative polymerase chain reaction (qPCR) analyses to determine the pre- and post-treatment abundance of infective viruses (plaque assay/$TCID_{50}$) as compared with the abundance of the viral genomes (qPCR), which gives estimations of the in-flow virus inactivation efficiency of the reactor.

1.4 Dissertation Objectives

This dissertation thesis focuses on two major research projects related to aerosol control and corona discharge and contains three topics. The first research project (one topic) is focused on powdered activated carbon (PAC) injection into the flue gas to remove mercury from the exhaust of coal-fired power plants (CFPPs) and its potential impact to climate change due to low removal

efficiency of PAC in ESPs. The second research project (two topics: virus aerosolization and NTP inactivation) is focused on packed-bed non-thermal plasma (NTP) and the experimental examination of in-flight inactivation of two airborne viruses, MS2 and PRRSv, by NTP. The aims of the work included in this thesis are summarized below:

1. Optical and physical characterization of mixed coal fly ash and particulate carbon:
    a) To provide the first comparative measurements of optical scattering and absorption coefficients of aerosols comprised of varying mixtures of FA and PAC.
    b) To investigate the optical and physical properties of various admixtures of coal combustion fly ash (FA) and PAC that may be emitted from coal-fired power plants employing PAC for mercury emissions control.
2. Suspending Viral Aerosols in an Airstream through Ultrasonic Atomization:
    a) To describe the method and necessary conditions required to successfully use a consumer-grade ultrasonic air humidifier to suspend viral aerosols in flowing airstreams in the service of studying airborne pathogen inactivation.
    b) To demonstrate the effectiveness of simple and economic light attenuation measurements in real-time *in situ* monitoring of virus solution atomization rates from the consumer-grade ultrasonic humidifier.
3. Inactivation of Airborne Viruses by Packed Bed Non-Thermal Plasma:
    a) To demonstrate effectiveness of a packed-bed dielectric barrier discharge non-thermal plasma in-flight disinfection system on inactivating aerosolized non-enveloped virus MS2, and enveloped virus PRRSv.

b) To contribute to the scientific understanding of generating non-thermal plasma at atmospheric pressure and the spontaneous inactivation of airborne viruses in a plasma environment.

CHAPTER II MATERIALS AND METHODOLOGY

2.1 Optical and Physical Characterization of Mixed Coal Fly Ash and Particulate Carbon

2.1.1 Experimental Setup

For this experiment, fly ash samples were collected from the first three rows of hoppers of a utility ESP at DTE's Belle River (BR) Power Plant in Michigan. At the time of fly ash collection, the Belle River station burned a low-sulfur, western sub-bituminous coal. Because of the cohesive properties of the finer ash taken from the second and third rows, only fly ashes from the first row of hoppers were used here, with the result being that these ash samples are a coarser fraction of the overall size distribution of ash collected in the ESP. Unburned carbon content was determined from loss on ignition (LOI) measurements conducted by DTE Central Chemical Lab. Norit Darco FGD used in previous studies of fly ash-activated carbon behavior (E. M. Lee & Clack, 2016; Prabhu et al., 2012; Prabhu, Lee, & Clack, 2011) was the powdered activated carbon (PAC) product added to the fly ash to form the particulate admixture, mixed on a mass per mass basis. The PAC particles had a lognormal size distribution, with a Sauter mean diameter of 5.9 μm and a long tail in the low end (Prabhu et al., 2012). It should be noted that PAC samples used in this research had relatively large size distributions as compared to freshly emitted BC, which may affect the particles' optical properties. Bond et al. (Bond & Bergstrom, 2006) and Martins et al. (Martins et al., 1998) have shown that the volume and/or mass

absorption cross sections would decrease with increasing particle size for particles that are larger than 0.1 μm. Particle's scattering properties are governed by the ratio of the particle size to the light wavelength, and generally for particles larger than 1 μm, the scattering coefficient would decrease with increasing particle size (Hinds, 2012). Admixtures consisted of BR FA samples amended with 0%, 0.5%, 1% and 2% (by mass) PAC. The two constituents were added to PTFE bags and the bags were tumbled inside the barrel of a rock tumbler (Thumler's Tumbler, Model B), for 10 minutes to ensure thorough mixing and uniform distribution of the PAC in the fly ash.

During measurements of optical properties, the FA-PAC aerosols were elutriated from the partially fluidized bed. Before fluidization, an empty fluidization vessel was loaded with 1,000 grams of each prepared admixture. Facility-supplied dried (10% RH) compressed air entered the vessel from below at five liters per minute (LPM) to partially fluidize the loaded admixture, a fraction of which was continuously elutriated, from which real-time optical characterization and aerosol integrated average mass loading determinations were made. Two sampling probes were installed in the top of the fluidized bed: one was connected to the PAX which sampled a portion of the elutriate (1 LPM) and took readings of scattering coefficients and absorption coefficients simultaneously; the other probe was connected to a particulate filter (filter cases: Savillex, Model No. 401-21-47-10-21-2; Polycarbonate filter: Whatman, 131135012E) used to determine the average aerosol mass loading of the elutriate which was weighed before and after collecting samples using an analytical balance. A rotameter (Omega, Model No. FL3840-ST) connected downstream of the PM filter indicated the air flow rate through the filter. The air flow rate needed to establish partial fluidization of the admixture varies with particle size (i.e., changing fluidization regime, based on Geldart classification (Geldart, 1973)), and in all cases exceeds the PAX sampling flow rate. As a result, most of the elutriated flow from the fluidized bed was

directed to an auxiliary PM filter and only 1LPM flow was directed into PAX. This auxiliary filter was not used for mass loading measurements but rather to maintain the same exhaust flow rate, and thus the same fluidization air flow rate and fluidized bed behavior, inside the vessel.

For the optical characterization of combustion-generated soot, an oil lamp (TIKI® Molded Glass Table Torch, Model No. 114109, burning TIKI® Brand Citronella Torch Fuel) was positioned at the bottom of a brick chimney built with four equally spaced openings around its periphery to promote a swirling updraft to stabilize the flame. A sampling probe connected to a vacuum pump sampled from the plume of the sooting flame at the top of the chimney at a rate of 12 LPM, a flow which was divided into two streams: one (1 LPM) directed to the PAX and the other (11 LPM) directed to the PM filter for aerosol mass loading determination.

2.1.2 Measurement Processes

In this experiment, the duration of the PAX measurement cycle was set to 500 seconds. In each measurement cycle, the first 70 seconds were devoted to automated flushing of the PAX measurement chamber with clean air and zeroing all sensors. The remaining 430 seconds were devoted to taking optical property measurements (referred to as the measurement stage).

For each new FA-PAC admixture, the fluidized bed was allowed to freely and continuously elutriate for at least 90 minutes before any measurements were taken to reduce aerosol mass loading so that the measured absorption and scattering coefficients were within the measurement range of PAX (<1 Mm^{-1} to 100,000 Mm^{-1}). Next, the PAX optical characterization and aerosol mass loading measurements were obtained separately. Only optical characterization occurred

during the first 120 seconds of this measurement stage, followed by switching the aerosol flow from the PAX to the PM filter to collect aerosol mass loading data over the next 180 seconds. This operational procedure was determined to be effective in avoiding any potential PAX measurement errors caused by sudden pressure changes when switching between the aerosol mass loading measurement and bypass filters during the measurement stage. For each FA-PAC admixture, three PAX and six mass loading measurements were taken in series to reveal the decay trends of measured optical properties with decreasing aerosol mass loading in the elutriate. For the soot measurements, samples were extracted promptly after the flame stabilized and PAX and mass loading data were acquired simultaneously for 300 seconds during the measurement stage.

In this experiment, PAX split the sampled flow into two chambers, one measured the absorption coefficient (B_{abs}) by in-situ photoacoustic technology and the other used a wide-angle integrating reciprocal nephelometer to measure the scattering coefficient (B_{scat}) of the generated aerosols simultaneously. The average B_{abs} or B_{scat} [m^{-1}] divided by the correlated mass loading [g/m^3] yields the estimates of mass absorption cross section (MAC) and mass scattering cross section (MSC) [m^2/g] of the sampled aerosol, after which the single scattering albedo (SSA) can be calculated using the equation:

$$SSA=MSC/(MSC+MAC) \quad (2.1)$$

MAC, MSC and SSA are parameters characterizing the optical properties of the particle emission, and are commonly applied by climate models when the emission factors are known or estimated. The laser wavelength used by PAX is 870nm and it was assumed that the obtained MACs depend inversely on light wavelength when comparing the results with other researches

(Bond et al., 2013). Scanning electron microscopy (SEM) images were taken of partially loaded PM filters to examine the agglomeration conditions of FA-PAC particles and estimate the average sizes of PAC and FA particles. The two types of particles can be distinguished by their shape in SEM images, since FA particles are spherical while PAC particles are generally irregularly shaped. Thermogravimetric analysis (TGA) of the elutriated aerosols provided measures of emitted aerosol carbon content (PAC plus unburned carbon on FA) as compared to initial admixtures loaded into the vessel.

2.1.3 Preliminary Testing

Before the start of measurements described above, one preliminary measurement was conducted. One thousand grams of seven different admixtures (Sand alone; Sand+0.01% PAC; Sand+1% Kentucky Utility [KU] FA; Sand+0.99% KU FA+0.01% PAC; Sand+1% Big River [BigR] FA; Sand+0.99% BigR FA+0.01% PAC and Sand+1% PAC) were prepared and loaded into the FB vessel separately and the dried compressed air entered the vessel from below at 18 LPM to partially fluidize the admixture. The PAX measurements were started during the early stage of fluidization, and the mass loading measurements were conducted from 130 s to 230 s during the PAX measurement period. Sand was used as the basic bed material in the preliminary test as a means of maintaining the bed fluidization behavior as that of Geldart Group B (Geldart, 1973), which can achieve stable and predictable fluidization easily with small volumetric expansion of the bed.

2.2 Ultrasonic Atomization of Virus Suspended in Bulk Liquid Solution

2.2.1 Ultrasonic Atomization of MS2 Suspended in Virus Dilution Buffer

2.2.1.1 Experimental Methods

Figure 2.1 (Plotted by Eric M. Lee) shows the setup used for the generation and collection of viral aerosols before and after exposure to a non-thermal plasma (NTP) reactor, the 11-component setup having five main components: an induced draft (ID) fan (1), an ultrasonic cool-mist humidifier, (3 & 8), separate upstream and downstream impingers (10 & 11), and the non-thermal plasma reactor (2). The present discussion focuses on components upstream of the reactor (3,8,9, & 10), and the remainder of the experiment is discussed in detail elsewhere (Xia, Kleinheksel, Wigginton, & Clack, 2018). A cool mist ultrasonic humidifier (Vicks V5100-N) generated a continuous flow of fine aerosols that was combined with the supply air in a short tee connector. The downstream induced draft fan controlled the flow rate (volumetric) of the supply air and the aerosols are drawn past the upstream impinger at 1 LPM (3.7 m distance from the introduction of mist into the air supply) and through the reactor, the supply air comprised of a mixture of ambient air (relative humidity, *RH*, typically 25-36%) and dry compressed air (*RH* typically <10%). Supplementing ambient air with dry compressed air substantially accelerated rate of droplet evaporation compared to ambient air alone.

2.2.1.2 Ultrasonic Humidifier Performance Testing

During the tests, the temperature and relative humidity of the air stream inside the sampling train was measured by a portable humidity/temperature pen (Traceable 4093), and the power consumption of the humidifier was measured by an electricity usage monitor (P3 International

P4460) over the range of eight built-in power settings (labeled as H1-H8 in this paper) of this humidifier model. To quantify the atomization rate and mimic the actual virus testing conditions, chilled virus dilution buffer (VDB, ~5°C, 0.78 g NaH_2PO_4/L, 0.58 g NaCl/L, ~0.2 g/L NaOH to adjust pH to 7.5) was added into the humidifier reservoir and atomized at three power levels (H2, H4 and H5) for 60 minutes. The VDB volume change before and after atomization was measured for each test and the average hourly atomization rate was estimated accordingly. The testing also included the measurement of VDB temperature increase inside the reservoir during atomization: cold VDB (~5°C) was atomized at three power levels (Humidifier_Off, H2 and H5) for 60 minutes, and the solution temperature was measured for every 20 minutes by a thermometer (TrueTemp 3516).

2.2.1.3 MS2 Aerosolization Testing

MS2 (a single-stranded RNA bacteriophage) was used to generate viral aerosols from the ultrasonic humidifier. Each trial involved adding to the ultrasonic humidifier reservoir 200 mL of the virus dilution buffer (VDB) containing ~$1x10^8$ pfu/mL of MS2. In the virus aerosolization tests, the humidifier was set to H2 and the atomization rate was approximately 117 mL/hr over a 30 minute experiment period. The air flow rate through the sampling train was maintained at 170 liter per minute (LPM). During each trial an electric vacuum pump (McMaster-Carr model #4176K11) drew sample from the air streams through the impinger (ACE Glass 7533-13) upstream of the reactor at 1 LPM over a 30 minute period, resulting in collection of the viral aerosols in the VDB used as impinger collection fluid. In addition, samples were collected directly from the ultrasonic humidifier reservoir before each trial. A plaque assay (described in section 2.3.1.3) was performed on each sample to determine the concentration of infectious MS2

in the collected VDB solution. To compare the humidifier reservoir samples with the upstream impinger samples, all of the acquired infectious MS2 concentrations in aqueous VDB solutions were converted to concentrations in the air stream using the following two mass balance equations:

$$C_{8,air} = \dot{m} \times \frac{C_3}{\dot{Q}_{air}} \tag{2.2}$$

$$C_{10,air} = \frac{V_{impinger} C_3}{\dot{Q}_{sample} t_{sample}} \tag{2.3}$$

Where C_3 and C_{10} are MS2 concentrations from plaque assays of the VDB solutions in the humidifier reservoir (3 in Figure 2.1) and the upstream impinger (10 in Figure 2.1), respectively. $C_{8,air}$ and $C_{10,air}$ are converted infectious MS2 concentrations in the air stream at the humidifier outlet and at the upstream sampling point, respectively. $\dot{Q}_{air}$ is the air flow rate through the apparatus, $V_{impinger}$ is the volume of VDB in each of the impingers (20 ml), and $\dot{Q}_{sample}$ and t_{sample} are, respectively, air flow rates through the impingers (1 LPM) and the standard elapsed time allowed for sampling (30 minutes). It should be noted that the MS2 inactivation in the VDB in the reservoir during atomization is not considered in the calculation of $C_{8,air}$, so the calculated results should be good approximations rather than true values.

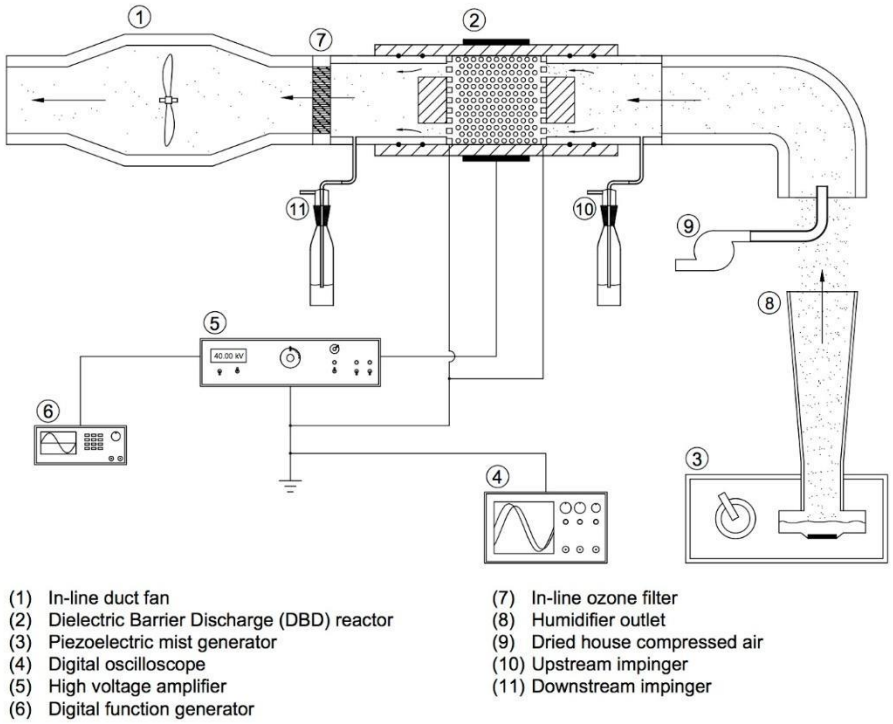

Figure 2. 1 Experimental setup for the inactivation of viral aerosols (Plotted by Eric M. Lee).

2.2.1.4 Testing of MS2 Survival in Humidifier Reservoir during Atomization

The concentrations of infectious MS2 were compared between the humidifier reservoir samples to determine the degree of inactivation occurring due to ultrasonic aerosolization. Beginning 5 minutes after the humidifier was turned on, samples were taken every 10 minutes for 60 minutes, the duration of the longest trial attempted in the study. When each sample was collected, the temperature in the reservoir was measured by a thermometer (TrueTemp 3516). Based on the increasing temperatures observed for the reservoir contents, a second series of trials was conducted with supplemental cooling provided by adding a Ziploc bag containing a cube of approximately 150 mL of ice to the reservoir, the largest volume of ice that the humidifier reservoir could accommodate with a maximum of 300 mL of VDB solution containing MS2.

2.2.2 Real-time Ultrasonic Atomization Rate Monitoring by Light Attenuation Measurements

2.2.2.1 Experimental Setup

The experimental setup of the *in situ* measurement technique for monitoring real-time virus solution atomization rate from the consumer-grade humidifier is shown in Figure 2.2. The procedure of suspending viral aerosols in an airstream by ultrasonic atomization has been described in detail previously (Xia et al., 2018). An optical bench was constructed with an inline HeNe laser beam (Coherent, model 31-2017-000, 0.46 mm diameter, $\lambda = 632.8$ nm) traversing the aerosol-laden airstream emitted from the humidifier and received by an unbiased photodiode (Thorlabs, model SM05PD1A). The optical bench was installed either immediately downstream of the humidifier outlet (Position ① in Figure 1) or upstream of the humidifier outlet (Position ② in Figure 2) with the laser beam passing through two 3 mm diameter apertures drilled in the outlet chimney wall. The apertures were drilled so that the chimney wall and droplets potentially accumulated on the inner wall would not cause unexpected laser light attenuation during the tests. The photodiode circuit, powered by a 25 V DC power supply (Lavolta BPS-305) was built according to the specifications provided by Thorlabs and the output voltage signal was measured by the built-in voltmeter of an Arduino platform (Arduino Duemilanove). Software code written using the open-source Arduino software (Arduino IDE) transmits data from the Arduino platform into the lab workstation (program code is included in the Appendix).

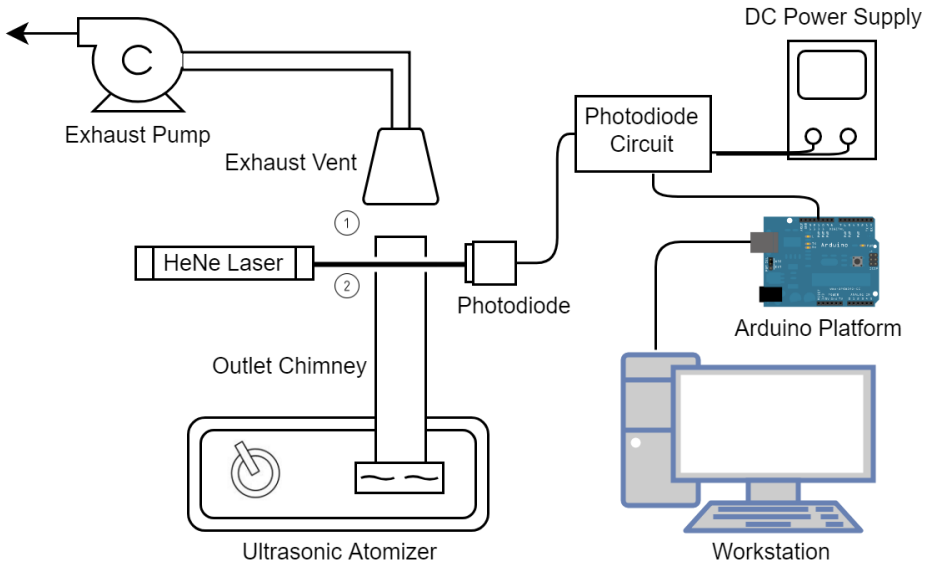

Figure 2. 2 Experimental setup for the real-time atomization rate monitoring system.

The laser applied in this study was a 632.8 nm Class 3B laser, which should not significantly inactivate aerosolized MS2 during the short (<1s) exposure time. To justify this assumption, 1 ml MS2 solution (~10^8 pfu/ml MS2 in VDB) was exposed to the same laser radiation for 1s, 5s, 20s, 60s and 300s respectively, and viable MS2 concentration in each sample after exposure was determined through plaque assay analysis. Two control tests, with 1 ml MS2 solution exposed to the air without laser radiation for 60s and 300s respectively, were conducted as well and the plaque assay results were compared with the corresponding laser exposure test results. Procedures of the plaque assay analysis have been described previously (Xia et al., 2018).

Light extinction by atomized droplets was measured *in situ* as an indication of real-time atomization rate (ml/min) of the humidifier at different power levels or atomizing various virus solutions. Light extinction can be described by the Beer–Lambert law:

$$I/I_0 = \exp(-\sigma_e L) \tag{2.4}$$

where I and I_0 are the attenuated light intensity and the initial unattenuated light intensity respectively, and L is the optical path length of the laser beam through the suspension. σ_e is the extinction coefficient of the droplets. For spherical droplets, σ_e can be determined by Eq. 2 below:

$$\sigma_e = \sum N_i A_i Q_{ei} = \frac{3m}{2\rho} \sum \frac{P_i Q_{ei}}{d_i} \tag{2.5}$$

For each particle size (d_i), N_i is the corresponding number concentration, A_i is the cross sectional area, and Q_{ei} is the extinction efficiency (Hodkinson, 1966). Eq. 2.5 can be further transformed to the right hand side format, where P_i is the mass fraction of the droplets with size d_i, m is the total mass concentration of spherical droplets across the light path, and ρ is the density of the droplets. By assuming that all droplets emitted from the ultrasonic atomizer have similar mass fractional size distributions (P_i is constant for each d_i), and the droplets of each size d_i have similar light extinction efficiency, Q_{ei}, σ_e will be proportional to m. At a constant flow rate of aerosols crossing the laser beam, m is proportional to the real-time atomization rate (mass of atomized liquid/time), $\dot{m}$. Thus, the combination of Eq. 1 and Eq. 2 indicates that, for a given optical path length L:

$$-\ln\left(I/I_0\right) \propto \dot{m} \tag{2.6}$$

Eq. 2.6 proves that the *in situ* measurement of I/I_0 can be a representation of the real-time mass (or volume, assuming constant density) atomization rate from the ultrasonic atomizer. In this study, the V/V_0 is equivalent to I/I_0 (where V and V_0 are the voltage signal output by the photodiode with and without light attenuation respectively), since the unattenuated HeNe laser intensity (0.8 mW) is within the range where the output voltage of the photodiode is linear with the incident light intensity.

2.2.2.2 Experimental Procedure

In this study before each test, 200 ml of virus solution was added into the humidifier reservoir. The HeNe laser and photodiode circuit were then turned on without light attenuation for 400s during the first group of tests with the optical bench installed at Position 1 in Figure 1 examining the atomization rate of the humidifier at different power levels, and for 500s during the rest of tests. The average voltage output over this unattenuated measurement period was calculated as the initial unattenuated signal, V_0, for each test. The unattenuated tests ensured that the laser source and photodiode were accurately aligned and the liquid accumulation on the outlet chimney (as shown in Figure 2.2) wall would not affect subsequent light attenuation tests. After the unattenuated tests, the humidifier was turned on, atomizing various virus solutions at different power levels for 30 minutes, and the real-time voltage signal, V, was acquired by Arduino for the estimation of real-time V/V_0. At the end of each test, the average atomization rate of the humidifier (ml/min) was estimated by measuring the total liquid volume reduction in the reservoir. The average atomization rate and average V/V_0 at different humidifier settings were used to develop a correlation between atomization rate and V/V_0.

As showed in Figure 2.2, the optical bench was installed at two positions. Initially, it was installed at Position 1 in Figure 2.2, a setup similar to the one developed by Lee and Clack (E. M. Lee & Clack, 2010). The setup had suspended droplets emitted into the open lab air before recollection by an exhaust vent, which may raise biosafety concerns when aerosolizing viral pathogens. To solve this problem, two 3 mm openings/apertures were drilled into the outlet chimney wall and the optical bench was moved to Position 2 in Figure 2.2 with the laser

traversing the chimney through the pinholes. The humidifier outlet chimney was designed to operate at partial vacuum relative to the ambient environment, so droplets will not escape through the openings/apertures, and the system would not emit bioaerosols into the ambient environment as long as the humidifier outlet was connected with an air-tight seal to the rest of the experimental setup. At each optical bench position, two groups of tests were conducted both with 200 ml of virus dilution fluid initially added into the humidifier reservoir. The first group of tests had fixed fluid composition and varied atomization rate: H2, H4, H6 and H8 were tested at Position 1, and H2 H3 and H4 were tested at Position 2 (the humidifier had eight built-in power settings, labeled as H1 to H8 in this paper). The second group of tests had a fixed atomization rate at H2 and varied fluid composition: MilliQ water + Dulbecco's Modified Eagle Medium (DMEM) solutions were tested with different volumetric mixing ratios (0%, 10%, 30% and 50% DMEM tested at Position 1, 0%, 10%, and 30% DMEM tested at Position 2). The two types of tests examined both the performance of the light attenuation system at different atomization rates and the impact on ultrasonic atomization of different potential compositions of virus solution having different liquid properties. Ultrasonic atomization is mainly influenced by ultrasonic frequency (Lang, 1962), but liquid viscosity, surface tension and liquid density can also affect the process. A correction equation proposed by Rajan and Pandit (Rajan & Pandit, 2001) predicted how liquid viscosity, surface tension and density would affect the diameter of aerosolized droplet, and data reported by McCallion et al. (McCallion et al., 1995) showed that increasing liquid viscosity generally led to decreasing ultrasonic atomization rate, while the change of surface tension did not have obvious effects on atomization rate. In this study, the piezoelectric transducer in the humidifier had a constant vibration frequency at each power level, optimized for pure water at room temperature. Two virus dilution buffer solutions were used in

our previous virus atomization experiments: virus dilution buffer (VDB) (0.78 g NaH2PO4/L, 0.58 g NaCl/L, ~0.2 g NaOH to adjust pH to 7.5) for aerosolizing Bacteriophage MS2, and MEM (which has similar ingredients to DMEM) for aerosolizing Porcine Reproductive and Respiratory Syndrome (PRRS) virus. VDB consisted mainly of MilliQ water with less than 2 g/L of total salts dissolved; viscosity and surface tension should be similar to those of MilliQ water. The addition of MEM or DMEM into VDB, MilliQ water or other inorganic salt solution, however, would significantly change the liquid viscosity and surface tension due to the introduction of glucose and other organic compounds. In this study, DMEM was mixed into VDB at different volumetric ratios to represent changing liquid properties by addition of organic compounds. The atomization rates of these mixtures produced by the humidifier at power level H2 were measured.

2.3 In-flight Inactivation of Airborne Virus by Packed Bed Non-thermal Plasma

2.3.1 In-flight inactivation of MS2 by Non-thermal Plasma

2.3.1.1 Experimental Setup

The experimental apparatus (Figure 2.3, which is the same as Figure 2.1) for non-thermal plasma (NTP) inactivation of viral aerosols includes: (1) an induced draft (ID) fan, (2) a dielectric barrier discharge (DBD) reactor, (3) an aerosol generator, (4) a digital oscilloscope, (5) a high voltage amplifier, and (6) a digital function generator. The aerosol generator is a modified consumer-grade cool-mist humidifier (Vicks V5100-N) piezoelectrically atomizing virus buffer solution containing MS2 phage, a single-stranded RNA bacteriophage. A 4-inch induced draft (ID) fan at

the end of the apparatus draws ambient air (25-36 % RH) into a flexible duct (4-inch OD and 13-ft in length), where mixing occurs between the air and the droplets, allowing for droplet evaporation and thus bioaerosol generation. The droplet evaporation process is further enhanced by the addition of a facility-supplied stream of dry compressed air (<10% RH) as shown in Figure 2.3 (label 9). The DBD reactor is powered by one of the two AC voltage amplifiers: A variable 0 to 20 kV (peak-to-peak) high voltage amplifier (Trek Model-610E) and a 30 kV fluorescent lighting transformer (France 15030 P5G-2UE ServiceMaster). The variable 0 to 20 kV high voltage amplifier is coupled with a digital function generator (BK Precision Model-4052) and the input and output signals were monitored by a digital oscilloscope (BK Precision Model-2190D). A honeycomb-structured ozone filter (Figure 2.3, label 7) (Burnett Process Inc. BP-4810) is placed downstream of the reactor to remove ozone from exhaust. Two impingers installed upstream (Figure 2.3, label 10) and downstream (Figure 2.3, label 11) of the reactor enabled the quantification of virus inactivation by the NTP reactor.

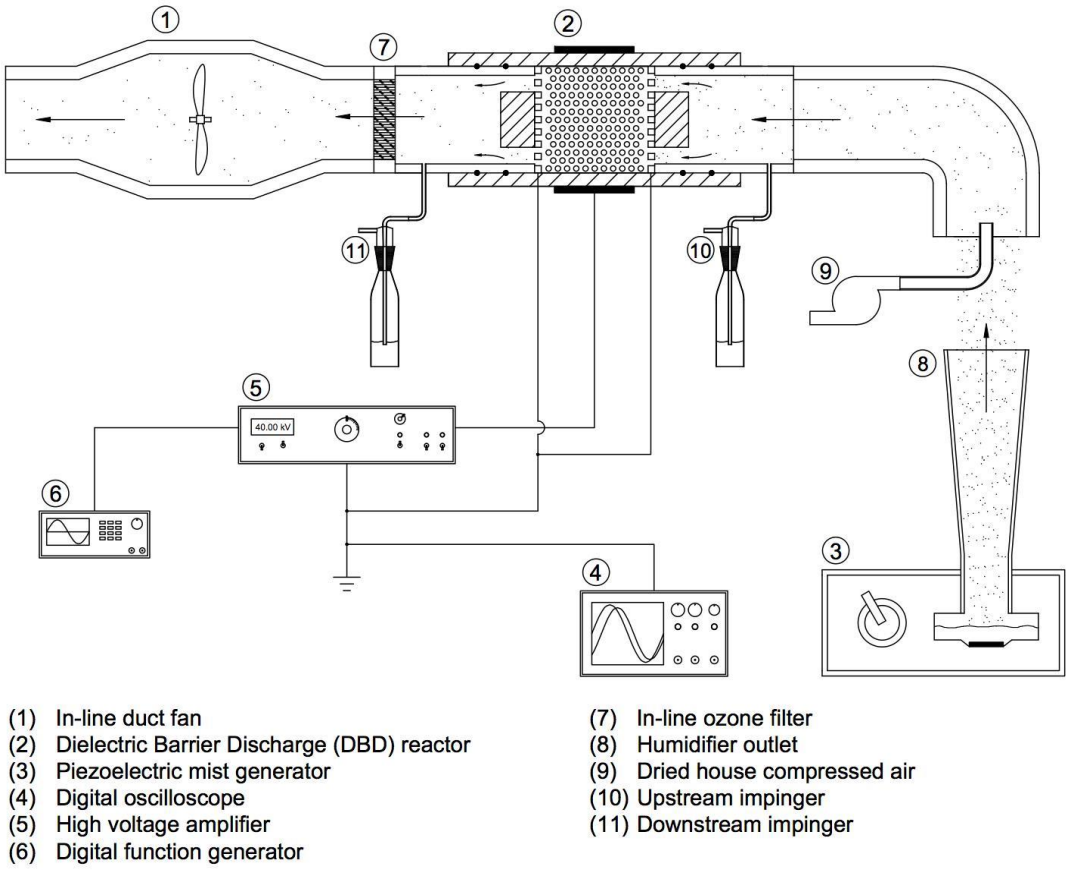

Figure 2. 3 Experimental setup for examining inactivation of viral aerosols by the NTP reactor (Plotted by Eric M. Lee).

2.3.1.2 Non-Thermal Plasma and Reactor Design

The NTP reactor developed in the present study utilizes the characteristics of DBD and packed-bed discharge for the application of viral aerosol inactivation. Figure 2.4 (plotted by Eric M. Lee) is a close-up schematic of the DBD packed-bed reactor. The reactor is composed of three Plexiglas tubes with two smaller tubes (3.5-inch OD, 3-inch ID, 6-inch length). The smaller tubes slide freely relative to the larger tube (4-inch OD, 3.75-inch ID, 8-inch length) due to a clearance of 0.125-inch. Two rubber O-rings, which sit in the grooves on the OD of the smaller

tube permit an air tight sliding mechanism. As indicated in Figure 2.4, a circular perforated brass plate is installed at the end of each sliding tube to serve as the ground electrode and to evenly distribute the inlet and outlet flow of the reactor. The design of the sliding electrode allows for packed bed depth adjustment ranging between 0.25 to 6 inches. A brass ring (0.035-inch thickness, 1-inch width) adhered to the OD of the larger Plexiglas tube serves as the positive electrode for the AC high voltage supply. Two flow plugs made of Styrofoam (2-inch OD) are positioned at the center of the reactor to direct the airflow with viral aerosols through an annular region in which the plasma is concentrated. The DBD reactor utilizes the microdischarge generated through a dielectric barrier made of Plexiglas. The packed-bed, consisting of 500 inert borosilicate glass beads (0.25-inch diameter), further enhances the microdischarge by partial discharges at the contact points between the glass beads for effective electron-viral aerosol collisions and inactivation process.

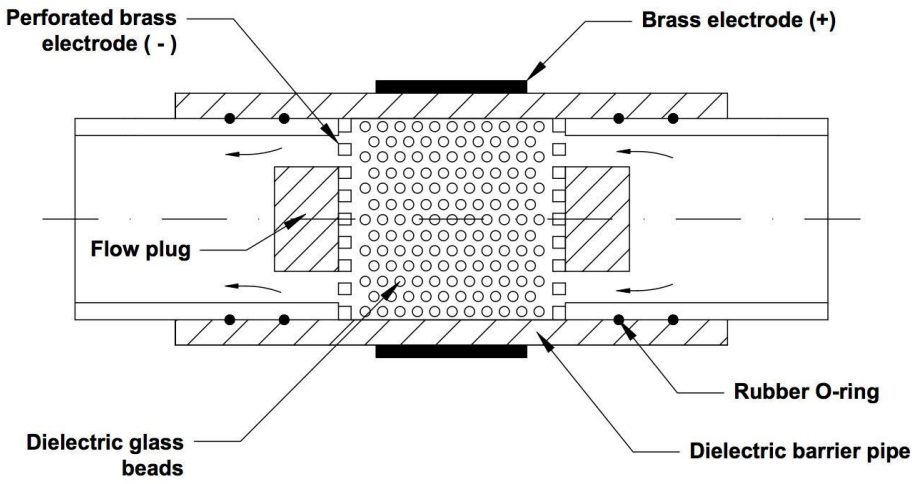

Figure 2. 4 Schematic of the DBD packed-bed non-thermal plasma reactor (Plotted by Eric M. Lee).

2.3.1.3 Experimental Procedure

During the virus inactivation tests, a consumer-grade ultrasonic humidifier was used to generate MS2 viral aerosols from the original virus solution. Each inactivation test involved adding into the ultrasonic humidifier reservoir 300ml (for 60-minute test) or 200 mL (for 30-minute test) of a virus dilution buffer (VDB) (0.78 g NaH_2PO_4/L, 0.58 g NaCl/L, ~0.2 g NaOH to adjust pH to 7.5) containing ~$1x10^8$ pfu/mL of MS2. The humidifier was set to built-in power level 2 (labeled as H2) and the atomization rate was approximately 117 mL/hr over a 30 minute experimental period (Xia et al., 2018). The air flow rate through the sampling train was maintained by the ID fan with a viable transformer (Staco Energy 3PN221B). In each test, the ID fan and humidifier was turned on for five minutes until reaching steady state. Then the packed-bed NTP reactor was activated by the selected high voltage supply and an electric vacuum pump (McMaster-Carr model #4176K11) was turned on to draw samples from the air stream through the impingers (ACE Glass 7533-13) upstream and downstream of the reactor at 1 LPM, leading to collection of MS2 aerosols in the 20 mL impinger collection fluid (VDB). For inactivation tests with the reactor powered by the 0-20kV variable amplifier, the sampling time was 30 minutes. For tests with the 30kV supply, the sampling time was 60 minutes in order to collect more viable viral aerosols using the impinger installed downstream of the reactor (Figure 2.3, label 11). Virus samples were collected directly from the ultrasonic humidifier reservoir as well before each trial. Plaque assays (described below) and reverse transcriptase quantitative polymerase chain reaction (RT-qPCR) were performed on each sample to determine the concentration of infectious MS2 plaque forming units (pfu/mL) and the concentration of MS2 genome copies (gc/mL) in the VDB collecting solution. To compare the humidifier reservoir samples with impinger samples, all of

the acquired infectious MS2 concentrations in aqueous VDB solutions were converted to concentrations in the air stream using the following two mass balance equations:

$$C_{8,air} = \dot{m} \times \frac{C_3}{\dot{Q}_{air}} \tag{2.7}$$

$$C_{10,air} = \frac{V_{impinger} C_{10}}{\dot{Q}_{sample} t_{sample}} \quad ; \quad C_{11,air} = \frac{V_{impinger} C_{11}}{\dot{Q}_{sample} t_{sample}} \tag{2.8}$$

where C_3 is measured MS2 concentrations from plaque assays of the VDB samples acquired from the humidifier reservoir (position 3 in Figure 2.3) right before each test. C_{10} and C_{11} are measured viable MS2 concentrations from plaque assays of the impinger collection samples (position 10 and 11 in Figure 2.3 respectively). $C_{8,air}$, $C_{10,air}$ and $C_{11,air}$ are converted infectious MS2 concentrations in the air stream at the humidifier outlet and at the upstream sampling point, respectively. $\dot{Q}_{air}$ is the air flow rate through the apparatus, $V_{impinger}$ is the volume of VDB in each of the impingers (20 ml), and $\dot{Q}_{sample}$ and t_{sample} are, respectively, air flow rates through the impingers (1 LPM) and the standard elapsed time allowed for sampling (30 minutes). It should be noted that the MS2 inactivation in the reservoir during atomization is not considered in the calculation of $C_{8,air}$, so the calculated results should be good approximations rather than true values. According to our previous study, there may be a 0.3-log reduction of viable MS2 concentration in the humidifier reservoir during the 30-minute test, but this inactivation would not affect the estimation of the NTP reactor inactivation efficiency as long as viable MS2 concentration is measured by the upstream impinger. Similarly, total virus particle concentrations (both infective and inactivated) were assessed with qPCR and measured as genome copies per milliliter of solution (gc/mL), corrected with Equations 1 and 2, and reported as genome copies per liter of air.

MS2 propagation and enumeration

MS2 (ATCC 15597-B1) and its corresponding *Escherichia coli* host ATCC 15597 was purchased from American Type Culture Collection (ATCC). MS2 was propagated and assayed in its *E. coli* host using previously published methods (EPA, 2001; Pecson, Martin, & Kohn, 2009). The virus stocks were purified using an Econo Fast Protein Liquid Chromatography system (Bio-Rad, USA) with a HiPrep Sephacryl S-400 HR column (GE, USA). The purified virus fractions were concentrated with 100 kDa Amicon ultracentrifugal filters (Millipore, USA), and finally filter-sterilized with 0.22 μm PES membrane filters. The final MS2 stocks (~10^{11} pfu/mL were stored in phosphate buffer (5 mM NaH_2PO_4 and 10 mM NaCl, pH 7.5) at 4 °C. In the experiments, the detection limit was 10 pfu/mL since only 100 µL of a sample was used for each plate.

RT-qPCR

Viral RNA was extracted from 200 µL MS2 virus samples using Maxwell 16 Viral Total Nucleic Acid Purification Kit (Promega, Madison, WI) according to the manufacturer's instructions. Extracted RNA was eluted using 50 µL of nuclease-free water. The forward primer (5'-CCGCTACCTTGCCCTAAAC-3') and reverse primer (5'-GACGACAACCATGCCAAAC-3') were designed with the Primer3free software (http://primer3.sourceforge.net/) and purchased from ThermoFisher Scientific (Grand Island, NY). Extracted MS2 RNA samples and RNA standards were reverse transcribed and amplified in parallel in an Eppendorf Mastercycler ep realplex Real-time PCR System (Eppendorf, Hauppauge, NY). Each reverse transcription-qPCR reaction was run in 20 µL of total volume comprising 10 µL of GoTaq 1-Step Master Mix, 0.4 µL of RT mix, 0.6 µL each of 10 µM forward and reverse primers, 6.4 µL of nuclease-free water

and 2 µL of RNA sample (Promega, Madison, WI). The following thermocycling conditions were used: 15 min at 40 ºC; 10 min at 95 ºC; and 45 cycles of 95 ºC for 15 s, 60 ºC for 30 s and 72 ºC for 40s, followed by a melting ramp from 68 to 95 ºC, with temperature hold for 45 s at 60 ºC and 5 s holds on all subsequent temperatures.

Measurements of System Performance

During the experiment, a portable humidity/temperature pen (Traceable 4093) measured the temperature and relative humidity (RH) inside the sampling train upstream of the reactor. An insertable anemometer (Extech 407123) measured the air stream radial velocity profile ~1ft downstream of the reactor. The pressure drops across the packed-bed NTP reactor and the ozone filter were measured by a low-pressure differential gauge (Magnehelic 2300-0). When the reactor was powered by the 0-20 kV variable amplifier, an oscilloscope (BK Precision Model-2190D) monitored the applied voltage and transferred current to the packed-bed NTP reactor, from which the power consumption can be calculated. When the reactor was powered by the fixed 30kV transformer, the power consumption of the transformer was measured by an electricity power meter (P3 International P4460) as the estimation of the pack-bed NTP reactor's power consumption. To ensure that collected MS2 would not be inactivated in the impinger liquid during sampling, 20 ml of $1x10^6$ pfu/mL MS2-VDB solution was added into the downstream impinger, which was then connected to the downstream sampling port. The packed-bed NTP reactor was either inactivated or activated by the 20kV voltage supply, and the effluent gas from the reactor was bubbled through the impinger liquid for 15, 30 and 45 minutes, after which the infectious MS2 concentrations of the impinger samples were examined through plaque assay. Ozone generated by the packed-bed NTP reactor when energized had the potential to

dissolve into sampling liquid in the downstream impinger and inactivate MS2 during and after sample collection. To quench the ozone in solution, 50mM of sodium sulfite anhydrous (Na_2SO_3, Fisher Scientific BP355-500) was added into the downstream 20ml impinger collection liquid. An ozone sensor (EcoSensors A-21ZX) measured the ozone concentration either upstream of the ozone filter (downstream of the reactor) or downstream of the filter to determine the amount of ozone generated by the pack-bed NTP reactor at various power and flow rate levels, and examine the removal efficiency of the ozone filter.

2.3.2 In-flight inactivation of Porcine Reproductive & Respiratory Syndrome (PRRS) virus by Non-thermal Plasma

2.3.2.1 Experimental Apparatus

The tests of PRRS virus inactivation by NTP were conducted using a small-scale non-recirculating wind tunnel located at the University of Minnesota. A schematic of the experimental setup is shown in Figure 2.5. The wind tunnel has an inside duct diameter of 3.5", an overall length of 96" and can operate in a volumetric flow rate range from approximately 3 to 30 cfm. A vacuum pump is connected at the outlet of the wind tunnel and the volumetric flow rate is maintained by measuring the differential pressure (OMEGA Differential Pressure Transmitter PX653-10D5V) across a calibrated orifice meter installed near the tunnel exit and applying the necessary voltage to the vacuum pump downstream of the tunnel. Temperature and relative humidity in the tunnel and absolute pressure are measured and taken into account in the volumetric flow rate measurements. The flow rate is calculated and maintained using PID feedback control in LabView. Data acquisition by the LabView software is facilitated by a National Instruments USB-6001 DAQ. A

HEPA filter is installed at the exit of the tunnel to prevent contamination or release of the PRRS virus into the laboratory.

The packed-bed NTP reactor was mounted in the test section of the wind tunnel (shown in Figure 2.5) and was tested at volumetric flow rates of 5 and 12 cfm. The design and schematic of the dielectric barrier discharge (DBD) packed-bed NTP reactor are described in detail in Section 2.3.1.2 and Figure 2.4. The Plexiglas tube wall serves as the dielectric barrier which would promote microdischarge generation. Two grounded electrodes, compressing 500 inert borosilicate glass beads (0.25-inch diameter) in between, formed the packed bed setup which further enhances the microdischarge by partial discharges at the contact points between the glass beads for more effective electron-viral aerosol collisions and inactivation process.

An air-jet large particle generator (LPG) atomizer was installed at the entrance of the tunnel and used to generate PRRS virus challenge aerosols. A PRRSv solution from a 65 ml syringe was fed into the LPG atomizer using a syringe pump set (New Era Pump Systems Inc. NE-300) at a constant liquid feed rate of 3 mL/min. Dry and filtered dispersion air at a volumetric flow rate of 1.5 liter per minute (LPM) was directed into the dispersion air inlet of the atomizer to aerosolize the virus solution reaching the atomizer nozzle. After aerosolization, the PRRSv aerosols were diluted and dried with lab air drawn into the wind tunnel, and the air was mixed thoroughly using a downstream orifice mixing plate, which generates turbulence to achieve uniform aerosol distribution in the air flow. Isokinetic probes were installed upstream and downstream of the packed-bed NTP reactor to extractively sample from the wind tunnel flow at 2.8 LPM, and the droplet number concentrations in the sampled air were measured by a portable optical particle

counter (OPC, TSI AeroTrak model 9306-V2). An aerosol diluter was used to prevent coincidence errors in the OPC. Another set of isokinetic probes were installed as well upstream and downstream of the packed-bed NTP reactor at the same locations as the OPC probes, which extractively sampled the wind tunnel air flow at a nominal volumetric flow rate of 9 LPM. The sampled air was drawn by a vacuum pump through two identical liquid impingers (Ace Glass, Inc. 125mL 24/25 Impinger), leading to collection of infectious and inactivated PRRSv aerosols in the 20 mL impinger collection fluid (Dulbecco's Modified Eagle Medium (DMEM)). The pressure drop across the NPT reactor was measured by another differential pressure transmitter (Omega PX653-03D5V).

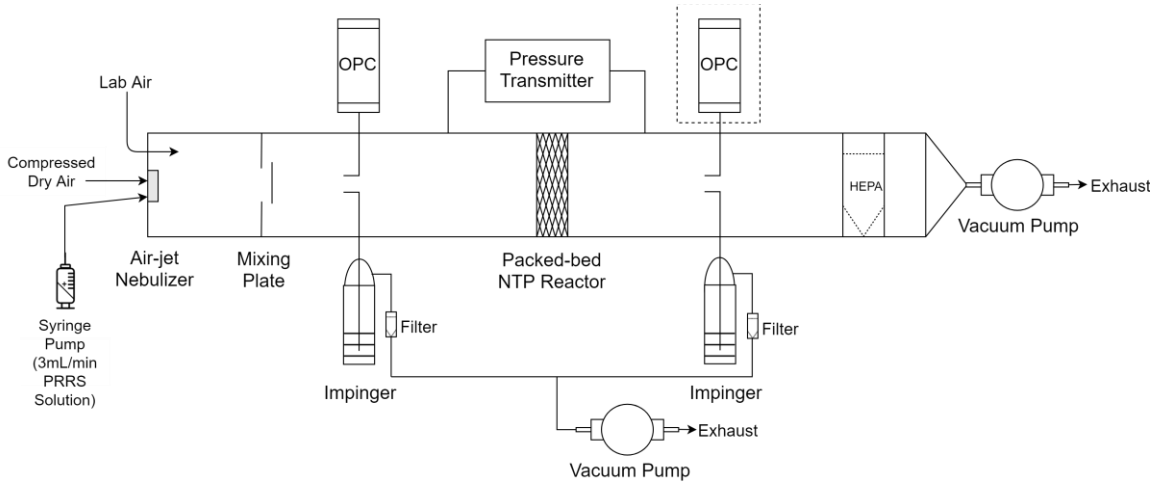

Figure 2. 5 Schematic of the small-scale wind tunnel setup at Univ. of Minnesota with the NTP reactor mounted in the middle test section. One OPC is in dashed box since only one OPC was applied in this study and was switched between upstream and downstream sampling probes.

2.3.2.2 Experimental Procedure

NTP Inactivation Testing Procedure

The tests of airborne PRRSv inactivation by the packed-bed NTP reactor took place in two phases, in May and August 2017, over the course of four months to allow time for samples collected in the first phase to be analyzed by the Veterinary Diagnostic Lab at Univ. of Minnesota. The two-phase tests were designed because there was initial concern that the sensitivity of PRRSv titration, which is limited by the initial titer of infective PRRSv that is aerosolized, might lead to a situation where no infective virus was detected downstream of the reactor, resulting in uncertainty as to the extent of virus inactivation. As a result, Phase 1 employed the lowest voltages to make sure to the extent possible that as little of the virus was inactivated. Test conditions in the second phase employed higher voltages after VDL analyses showed the results of Phase 1 yielded partial inactivation.

In the first phase (May data), the NTP reactor was operated at voltages of 12, 16, and 20 kV, and the highest NTP deposited power was 1.7 W achieved at 20 kV. In the second phase (August data), voltages of 30 kV were applied in the reactor using a second power supply, resulting in about 23 W power consumption by the NTP reactor. For each voltage setting, the PRRSv inactivation by the packed-bed NTP reactor was examined under two air flow rates (5 cfm and 12 cfm), and all tests were conducted in triplicate. In each phase (May and August), two control tests, either with the reactor deactivated (no voltage supplied) or with the reactor uninstalled, were also conducted in duplicate. At the beginning of each test, the vacuum pump downstream of the sampling train was turned on to reach constant desired flow rate though the wind tunnel, after which the syringe pump and compressed air supplied to the air-jet nebulizer were turned on to initiate PRRSv aerosolization. When consistent mist was observed emitting from the nebulizer, the packed-bed NTP reactor was activated (for reactor-on tests only), and the pump downstream of the impingers was turned on to start the 20-minute impinger sampling. Only one OPC was available for this study, which was

switched between upstream and downstream sampling probes, consecutively making 5-minute upstream particle size distribution (PSD) measurement, 5-minute downstream PSD measurement, and then another 5-minute upstream PSD measurement during the 20-minute testing period. The two 5-minute upstream PSD data were averaged as an estimation of the upstream PSD during the interim period between those measurements when the downstream PSD was actually measured. The OPC had six particle size bins (set to 0.3 μm, 0.5 μm, 1 μm, 3 μm, 5 μm and 10μm) and was set to report the differential particle number concentrations between adjacent bin sizes. It was assumed that the log-average of two consecutive bin sizes was the average droplet size for the corresponding measured differential number concentrations.

PRRS Virus Preparation, Aerosolization and Collection

Researchers at the University of Minnesota propagated PRRS VR2332 strain in MARC-145 cells followed by titration of the virus to 10^5 $TCID_{50}$/mL. The virus was aliquoted and frozen at -80°C until used. For each test, a syringe was filled with 65 mL of PRRSv at 10^5 $TCID_{50}$/mL, placed into a New Era pump system, model NE-1000 multi-phaser, and aerosolized into the testing chamber at 3 mL/min via an air-jet nebulizer for 20 minutes. Room temperature and relative humidity (RH) level were measured during each test by a portable humidity/temperature pen (Traceable 4093). During each test, air samples were collected with twin impingers, placed upstream and downstream of NTP reactor, for 20 minutes. Each impinger was filled with 20 mL of DMEM supplemented with 1.5 mg/mL of bovine serum albumin fraction V 7.5%, 1X antibiotic-antimycotic, 0.0015 mg/mL of Trypsin-TPCK, and 0.05 mg/mL of gentamicin. After 20 minutes sampling time, the volume of supplemented DMEM in each impinger was measured, recorded, aliquoted into 3 tubes and frozen

at -80°C until tested. The collected impinger samples were submitted to the Veterinary Diagnostic Lab at the University of Minnesota for Quantitative RT-PCR analysis and $TCID_{50}$ assay analysis.

Quantitative RT-PCR (RT-qPCR)

The Minnesota VDL quantified samples for the PRRSv genome using quantitative RT-PCR as previously described (Cho et al., 2006). A standard curve based on transcript RNA with a quantitative linear range from 1×10^3 copies/µL to 1×10^6 copies/µL was used to determine the RNA copy number/mL. The copy number/mL results were consecutively converted to copies/m^3 of air.

Sample Titration

Samples were serially diluted 5-fold. 100 uL of the serial dilution was plated onto 96-well plates containing MARC-145 cells in 4 replicates. Plated samples were incubated for 7 days at 37°C with 5% CO_2. At day 7, plates were removed and CPE was read and recorded. $TCID_{50}$/mL was calculated using the Spearman-Karber method followed by conversion to $TCID_{50}/m^3$ of air. PRRSv titration was conducted by the Veterinary Diagnostic Lab at the Univ. of Minnesota.

Testing the Effects of Liquid Accumulation on NTP Performance

During the experiment, it was observed that compared with the previous bacteriophage MS2 inactivation tests, more virus solution droplets (mainly DMEM in this study) impacted upon the packed-bed and accumulated in the reactor between the glass beads, likely due to higher RH conditions of the supplied air, shorter distance between the atomizer and the packed-bed NTP reactor, and potentially larger droplets produced by the air-jet large particle generator. The

accumulated virus solution may promote virus aerosol filtration by the packed-bed, but can also lead to potential re-emission of viral aerosols from the packed bed into the air stream. In addition, increase of RH and accumulation of liquid inside the packed-bed may change the NTP discharge scenario, serve as a protective reservoir for suspended viruses, and affect reactive species formation by the NTP. To examine the effects of accumulated DMEM solutions, tests were conducted at the University of Michigan using bacteriophage MS2 as the target virus. DMEM solutions of 5 mL and 10 mL were preloaded by spray in the packed-bed reactor before powering the reactor and starting each test. The reduction of airborne infectious MS2 between the upstream and downstream impingers was examined for the DMEM-soaked packed-bed NTP reactor with the reactor powered by the 20 kV power supply at 170 LPM air flow rate. The setup of the sampling line, the methodology of MS2 ultrasonic atomization, and the virus sample analysis methods were described in detail in Section 2.2.1 and Section 2.3.1.

CHAPTER III OPTICAL AND PHYSICAL CHARACTERIZATION OF MIXED COAL FLY ASH AND PARTICULATE CARBON

3.1 Short review on the research background and methodology

Mercury (Hg) is an environmental pollutant of concern due to its tendency to cycle between soil, air, and water; its bioaccumulation within the food chain; and its toxic effects on human and wildlife health. Coal-fired power plants (CFPPs) are one of the major sources of anthropogenic mercury emissions. The most mature technology for controlling mercury emissions from coal combustion is the injection into the flue gas of powdered activated carbon (PAC) adsorbents having chemically treated surfaces designed to rapidly oxidize and adsorb mercury. However, carbonaceous particles are known to have low electrical resistivity, which contributes to their poor capture in electrostatic precipitators (ESPs), the most widely installed device for particulate control in coal-fired power plants worldwide. Thus, the advent of mercury emissions standards for power plants has the potential for increased emissions of PAC. The emitted PAC is expected to have optical properties similar to submicron black carbon (BC), which can have the second largest effect on climate forcing behind CO_2. Our previous analyses have provided estimates of PAC emission rates resulting from PAC injection in the US and extrapolated these estimates globally to project their associated climate forcing effect. The present work continues our examination by conducting the first comparative measurements of optical scattering and absorption of aerosols comprised of varying mixtures of coal combustion fly ash (FA) and PAC

to better understand the actual climate forcing potential of incidentally emitted PAC. Detailed literature review of this research background is provided in Section 1.2.

The objective of this research is to provide the first comparative measurements of optical scattering and absorption of aerosolized FA and PAC admixtures, in an effort to better constrain the potential climate forcing effects of emitted PAC resulting from ACI used to reduce mercury emissions. A partially fluidized bed (FB) containing fly ash-PAC admixtures with varying PAC concentrations elutriates aerosol agglomerates. A photo-acoustic extinctiometer (PAX, Droplet Measurement Technologies, Boulder, CO) extractively samples from the FB flow, providing measurements of optical absorption and scattering coefficients of fly ash (FA) alone and FA-PAC admixtures. Extracted aerosol samples from the FB flow provide particulate loading measurements, thermogravimetric analysis (TGA) provide estimations of the carbon content of the particulates collected from the FB emission, and SEM images of the collected aerosols provide qualitative insight into the aerosols' size distributions and agglomeration state. Soot from an oil lamp flame provides a comparative benchmark. The research methodology is illustrated in detail in Section 2.1.

3.2 Preliminary Test Results of the Fluidized Bed

Figure 3.1 shows the preliminary PAX optical absorption coefficient (B_{abs}) readings of the emissions from seven different bed mixtures with the inset image outlined in red highlighting the period when both PAX readings and mass loading measurements were taken at the same time. PAX measurements displayed in Figure 3.1 showed that the 100 times increase in PAC mass concentration (from 0.01% to 1%) in the fluidized bed yielded a ~1200 times increase in B_{abs} of

the emission. This demonstrates how the addition of PAC to the sand can change optical absorption of the elutriated aerosol mixtures significantly. The disproportionate increase of B_{abs} with the addition of PAC to the sand may be due to the change of fluidization behavior due to the finer and less dense PAC. The addition of 0.01% PAC to 1% FA in sand mixtures as the bed material increased B_{abs} more than occurred for the 0.01% PAC addition to sand alone. Comparing the results between the two examined fly ashes, it is apparent that the B_{abs} readings of different FA samples may be affected differently by the addition of PAC, a result of differences in the baseline FA B_{abs}, FB emission rates, or the emitted particle size distributions.

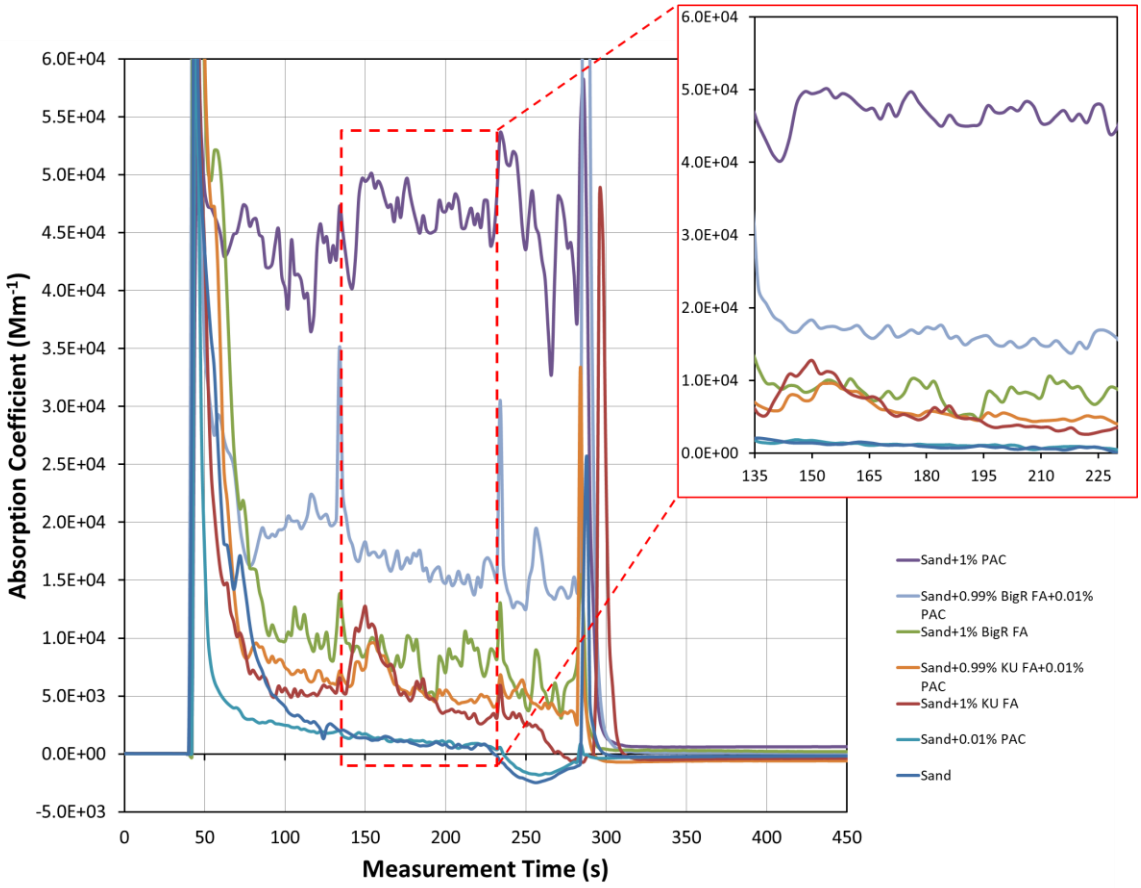

Figure 3. 1 Preliminary B_{abs} readings of the emissions from seven different bad mixtures.

Figure 3.1 illustrates several experimental challenges that are unique to this measurement process. Firstly, in the figure the initial high B_{abs} readings indicate that the initial aerosol emission rates from the FB were very high and decayed rapidly. The initial high emission rates readily fouled the optical windows inside the PAX and caused inaccurate errors in the measurement of absorption coefficient (B_{abs}) and scattering coefficient (B_{scat}). Also, the rapid decay in both readings makes successful demonstration of repeatability difficult. Secondly, the FA and PAC admixtures fall into the Geldart Fluidization Group C (Geldart, 1973), which is the most difficult and least predictable group for achieving stable fluidization. To achieve a relatively more stable and predictable fluidization, sand (Group B) was used as the basic bed material. However, the optical property of sand is not of interest in this context, no techniques were available for differentiating concentrations of sand from those of fly ash, and the emission of large amounts of sand may affect the B_{scat} results significantly due to its high single scattering albedo (SSA). Thirdly, in the experimental procedure the position of a three-way valve downstream of the FB was switched at the start of the mass loading measurement, which caused a pressure spike in the FB vessel and a corresponding spike in B_{abs} readings (observed in sand+1% PAC samples and sand+KU FA samples). To address these issues, it was necessary to delay the start of PAX measurements until FB emission rates decreased to the PAX acceptable measurement ranges, employ a different fly ash (BR FA) to meet Geldart Group B fluidization behavior, and use paired experiments to obtain, separately, PAX and mass loading measurements free of pressure-induced spikes. The remaining results reported here were all obtained using this revised procedure.

3.3 Optical Characterization of Combustion-Generated Soot

Figure 3.2 illustrates the PAX measurement results of the plume from the sooting flame during the first three tests. The relatively consistent readings indicate that the emission sampled was relatively steady and there was no increasing or decreasing trend observed. Unlike the pressurized fluidized bed, the sooting flame was an open flame at atmospheric pressure and therefore there were none of the pressure spikes and B_{abs} spikes that occurred for the fluidized bed. Because of these reasons, for the characterization of combustion-generated soot both PAX readings and mass loading measurements were taken simultaneously for 300 seconds during the six tests. The average MAC and MSC of the generated soot were calculated for each test, and the final results are summarized in Table 3.1. The final average MSC and MAC for combustion-generated soot are 0.90 m^2/g and 2.15 m^2/g respectively, and the average single scattering albedo (SSA) is calculated to be 0.29.

Table 3. 1 Calculated MAC and MSC of the combustion generated soot in six tests.

	Test 1	Test 2	Test 3	Test 4	Test 5	Test 6	Average	Standard deviation
MSC (m^2/g)	0.87	0.89	0.87	0.88	0.95	0.94	0.90	0.04
MAC (m^2/g)	2.13	2.11	2.09	2.13	2.31	2.13	2.15	0.08

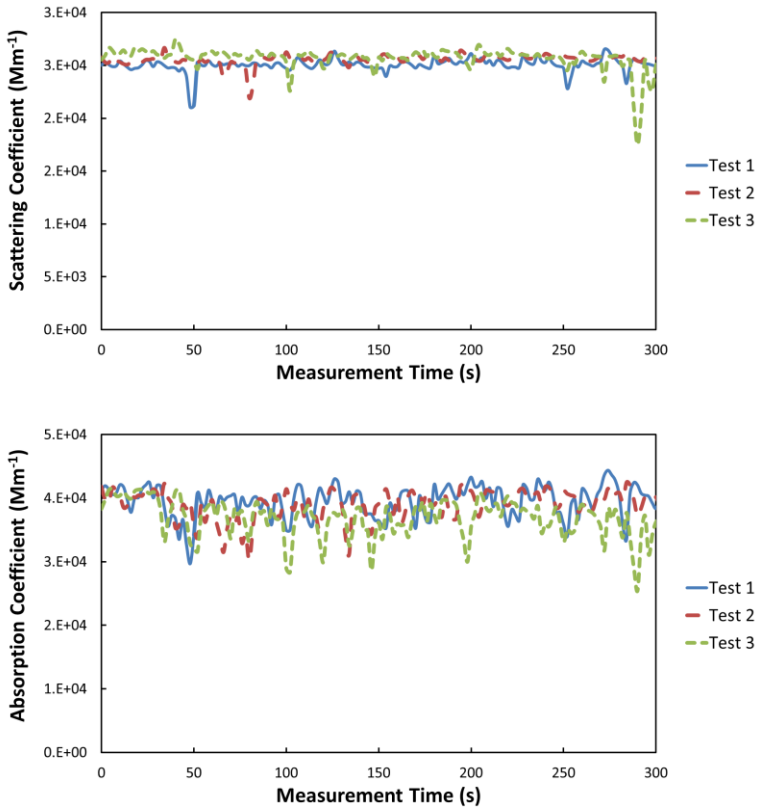

Figure 3. 2 PAX measurement results of the combustion-generated soot during the first three tests.

3.4 Physical and Optical Characterization of FA-PAC Admixtures

3.4.1 Physical characterization of FB emissions

The measurements illustrated in the following sections utilized the BR fly ash as the basic bed material which belongs to the Geldart Fluidization Group B (Geldart, 1973). The BR FA can achieve a relatively steady and predictable fluidization, and was mixed with 0%, 0.5%, 1% and 2% PAC by mass as the bed material.

Figure 3.3 shows the mass loading measurement results of the FB emissions from four bed material admixtures with different FA-PAC mixing ratio. All of the emissions showed a strong exponential decay, which can be used to estimate the real-time mass loadings for each of the PAX measurements. From the figure it is apparent that the addition of 0.5% PAC into BR FA can significantly increase the emission from the FB (both measurements started after 90 minutes' free elutriation of the FB). During the tests, it was observed that the addition of PAC can promote fluidization of the admixtures, and the particle emission from the FB would increase greatly as the increase of PAC mixing ratios in the bed material. For the bed material mixed with 1% and 2% PAC, the emission further increased and the fluidized bed was allowed to freely and continuously elutriate for 30 and 60 more minutes respectively before measurement so that the aerosol absorption coefficient would reduce to levels within the measurement range of PAX. This is the reason why the mass loading results presented in Figure 3.3 decrease with the increase of PAC mixing ratio in the bed material.

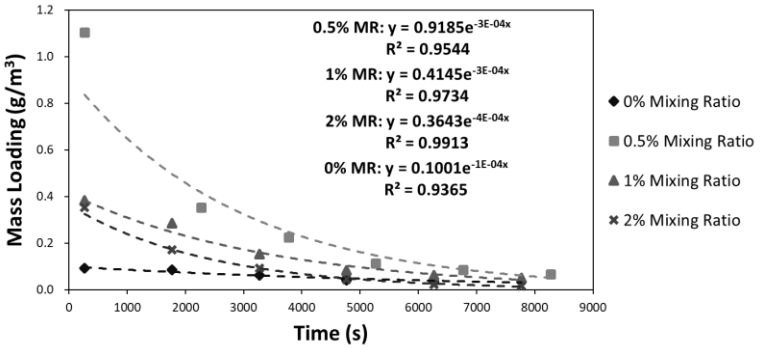

Figure 3. 3 Mass loading measurement results of the FB emissions from four bed material admixtures.

Figure 3.4 shows the TGA measurement results of the collected emissions from the FB with PAC mixed in the bed material. The three lines show similar decay patterns. The small mass reduction at 30°C was likely evaporation of water contained in the collected particles, and the major mass reduction between 450°C and 530°C was induced by the oxidation of carbon in the collected particles to CO_2. Based on the DTE chemical analysis, the BR FA applied in these measurements contained only 0.14% carbon and the remaining mass was only composed of fully oxidized metal oxides such as SiO_2 (51.77%), Al_2O_3 (14.44%) and CaO (13.12%), so there is no cause of mass change expected during the TGA test other than water evaporation and carbon oxidization. Calculated from Figure 3.4, there was 18.57% carbon by mass in the emission from the 0.5% PAC bed, 30.37% carbon in the emission from 1% PAC bed, and 41.81% carbon in the emission from 2% PAC bed.

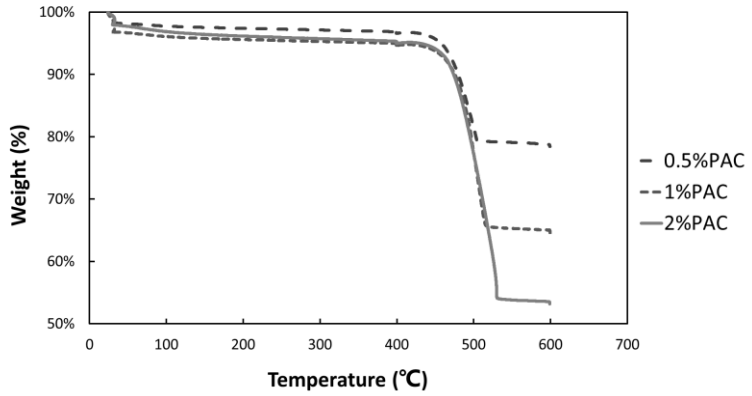

Figure 3. 4 TGA test results of emissions from three different FB materials.

Figure 3.5 shows two typical SEM images of the particles collected from the FB emission with and without PAC mixed in the bed. All FA particles showed spherical shapes while PAC particles were mainly irregularly shaped, which should be mainly due to pulverization in PAC production. According to Figure 3.5(b) and other acquired SEM images of collected FA-PAC

emissions, the average particle diameters were 6.21μm for PAC and 2.63μm for FA, which are relatively larger than the particles expected to be emitted from power plants' stacks (Gladney, Small, Gordon, & Zoller, 1976). This may be because the smaller particles that are more easily entrained in the air flow during the initial stage of fluidization had been exhausted during the free elutriation of the FB before any measurements and as a result only larger particles were sampled and characterized. Last but not least, according to SEM images, PAC and FA did not agglomerate even after the intensive mechanical mixing by the rock tumbler. In the flue gas, the PAC and FA particles are diffused by large volume of gas and thus have fewer contact opportunities to agglomerate than in the mixing barrel of the rock tumbler. In addition, in ESPs particles are charged to the same polarity and tend to repel each other, which further reduces the likelihood of FA-PAC agglomeration. Therefore, it is reasonable to infer that the large PAC and FA particles of the same size range would not agglomerate in the flue gas of the coal-fired power plants.

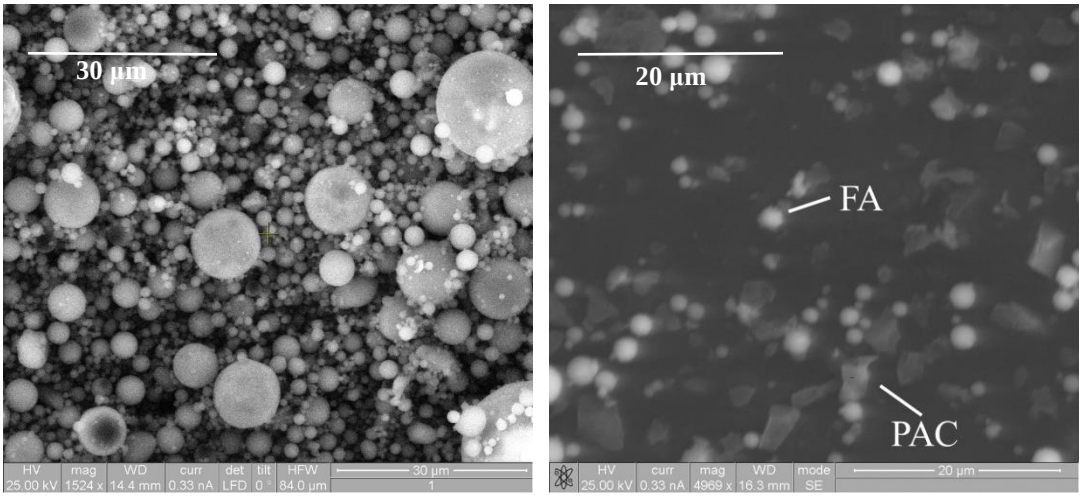

(a) (b)

Figure 3. 5 SEM images of the particles collected from the FB emission (a) without and (b) with PAC mixed in the bed.

3.4.2 Optical Characterization of FB emissions

For the emission from each FB with a specific bed FA-PAC mixing ratio, three groups of PAX data were acquired during the measurement time (0-120s, 1500-1620s, and 3000-3120s). Each group of PAX data measured the B_{abs} and B_{scat} of the emission for 120s and the results were averaged for every two seconds. For every two seconds, the mass loading in the emission were calculated according to the exponential decay presented in Figure 3.3. The PAX readings of B_{abs} and B_{scat} divided by the correlated mass loading calculation results yield the MAC and MSC of the emissions for every two seconds, and the final MAC and MSC of the emissions from each FB with a specific bed FA-PAC mixing ratio were calculated by averaging the three groups of data points.

The correlations of the resulting average MSCs and MACs with the emissions' carbon contents obtained in TGA test are presented in Figure 3.6. From the figure, it can be found that the MSC of the FA-PAC admixture particles emitted from the FB increased linearly with the increase of the particles' carbon content with a slope of 0.072 m^2/g, and the MAC increased linearly with the increase of the particles' carbon content with a slope of 0.14 m^2/g. Figure 3.6 also showed that the increase of carbon content from nearly 0% to 41% in the emission can cause a 1.4 times increase of MSC and a 40 times increase in MAC. This is reasonable since according to Figure 3.5, there was no agglomeration between FA and PAC particles. The two types of particles were externally mixed and the resulting MSC and MAC of the admixture were simply the addition of the MSC and MAC of the two types of particles according to their mixing ratio. The acquired MSC and MAC of FA-PAC admixture particles are much smaller than the obtained properties of soot, which should be due to the large particle size of FA and PAC sampled. The large error bars

for the data with >30% carbon content should be due to carbon content fluctuations in the emission from the FB, where active fluidization was promoted by the addition of PAC.

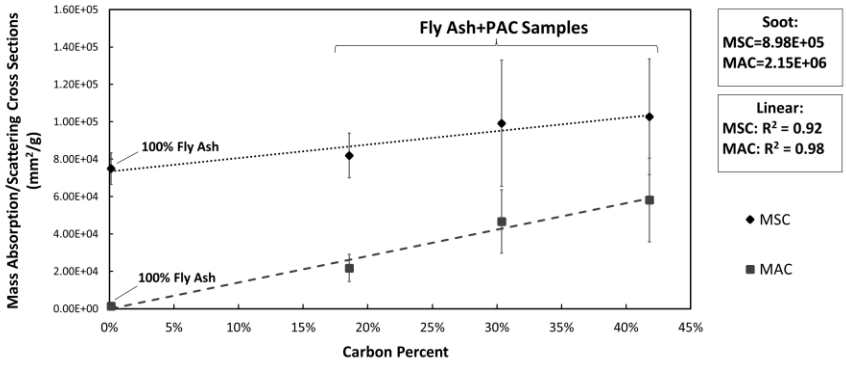

Figure 3. 6 Correlation of the obtained MSC and MAC with particles' carbon content.

In addition to the MAC and MSC, the SSAs of the emissions for every two seconds' PAX data points were calculated, and the final SSA of the emissions from each FB with a specific bed FA-PAC mixing ratio were calculated by averaging the three groups of data points. The correlation of the calculated SSAs with the emissions' carbon contents is presented in Figure 3.7 with a data point representing the soot measurement result assuming a 100% carbon content. From the figure, it can be found that the SSA of the FA-PAC admixture particles decreases with increasing carbon content. A trendline calculated from Eq. 2.1 and the linear correlations presented in Figure 3.6 was drawn as well, from which it can be found that when the carbon content reaches 100% (pure PAC emission), the SSA obtained from the trend line is about 0.51, 75% higher than the measured soot SSA (~0.3). This indicates that the sampled PAC emission may not be as absorptive as soot, possibly due to its larger size and irregular shape. The assertive assumption that soot contains 100% carbon can also lead to uncertainties in this comparison. Soot is a

mixture of carbon and various organic materials, and to further examine the optical propriety of soot generated in this research, its chemical composition should be studied.

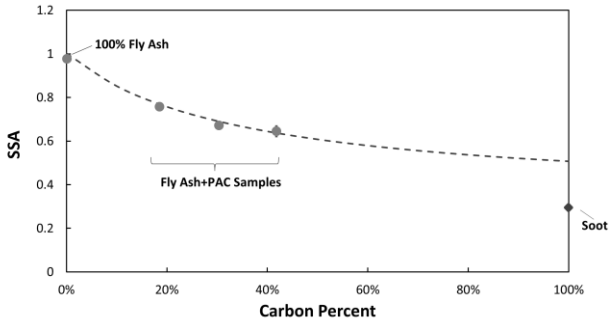

Figure 3. 7 Correlation of the obtained SSA with particles' carbon content.

3.5 Comparison with Other Research

In this section, the optical properties obtained in last section are compared with relevant measurement results from other research. The comparison is only focused on MAC and SSA results since the two properties are the most commonly used ones by models to predict aerosol climate forcing.

The MAC of soot, or black carbon (BC), has been measured and reported by many researchers, while the results vary significantly due to the vague definition of black carbon. Before any comparison, it should be noted that the aerosol light absorption property is dependent on the wavelength of light. The equation below is a commonly used one to characterize the spectral dependence of MAC using the absorption Ångstrom exponent ($Å_{abs}$):

$$MAC=K\lambda^{-Åabs} \quad (3.1)$$

where K is a constant and λ is the wavelength of light (Bond, 2001). Bond (Bond et al., 2013) suggested $Å_{abs}$=1 in regions where externally mixed BC dominates absorption, while it is stressed that the assumption is only valid over the light wavelength throughout the visible spectrum (Bond & Bergstrom, 2006). The research conducted by Kirchstetter (Kirchstetter, Novakov, & Hobbs, 2004) measuring light attenuation by soot generated from motor vehicles throughout the light wavelength from 330nm to 1000nm proved that the assumption of $Å_{abs}$=1 is valid over a larger wavelength range, which is supported by the research of Russell et al (Russell et al., 2010). In this research the wavelength used by PAX is 870nm and it is assumed that $Å_{abs}$=1 for all samples, which means that the obtained MACs depend inversely on light wavelength.

Bond and Bergstrom (Bond & Bergstrom, 2006) suggested a value of 7.5±1.2 m^2/g (550nm wavelength) for the MAC of fresh light-absorbing carbon, which is over two times that of the acquired soot MAC (3.4 m^2/g adjusted to 550nm) in this research. Other photoacoustic measurements of BC aerosols emitted from diesel engines or acetylene smoke also suggested much larger MAC values (Bruce, Stromberg, Gurton, & Mozer, 1991; Roessler & Faxvog, 1979; Szkarlat & Japar, 1981). One reason of the low MAC value obtained in this research may be the low temperature and short height of the oil lamp flame. Combustion generated carbon is a type of amorphous carbon which contains both sp^3 and sp^2 bonds, and the islands of sp^2-bonded (graphitic) clusters control the light-absorbing properties of the particle (Robertson & O'reilly, 1987). The transformation of carbon with primarily sp^3 bonds to that with sp^2 bonds is called graphitization, which is a common process that occurs to carbonaceous particles passing through the flame and is positively correlated to the flame temperature and particles' residence time in flame. The flame generated by an oil lamp in this research was only about 10 cm tall, which is

expected to have a relatively low flame temperature compared with diesel engines and acetylene flames, and emit carbonaceous particles quickly into the surrounding environment (Oberlin, 1984; Sattel, Robertson, & Ehrhardt, 1997). As a result, fewer sp^2 bonds were formed in the sampled soot and therefore the measured MAC was low.

The soot SSA obtained in this research is 0.29, which is within the 0.2-0.3 value range suggested by Bond and Bergstrom (Bond & Bergstrom, 2006). The value of SSA depends one both light wavelength and particle size distributions, so further comparison of the obtained SSA with other measurement results is not representative and applicable. The measurements also report a SSA value of 0.98 for BR fly ash, which is comparable with the sand duct SSA value reported previously by other researchers. Tanre et al. (Tanré et al., 2001) reported a 0.96-0.97 value for the SSA of sand dust measured using 870nm wavelength light, and Kim et al. (D. Kim et al., 2011) reported a SSA of 0.94-0.95 over a wide wavelength range. These consistent results are reasonable since the major chemical component of FA and sand dust are both SiO_2. Because of this similarity, the emission of FA from CFPPs is often assumed to be entirely mineral in climate simulations of BC climate forcing and BC emissions inventories (Bond et al., 2004; Cao et al., 2006; Reddy & Venkataraman, 2000).

3.6 Estimation of PAC emissions from CFPPs

According to the discussion in the last section, the emission of FA from CFPPs is often assumed to be entirely mineral, while the measurement results presented in Figure 3.6 show that the increase of carbon content of the particles emitted from the power plants may cause a significant linear increase of MAC of the emissions. It is expected that the installation of ACI technologies

has the potential to increase the carbon content of CFPPs' emissions, and in this section the carbon content (as the PAC mass fraction of the total particles emitted) of the emission from an ESP is examined as a function of the ESP's FA removal efficiency.

Figure 3.8 shows the calculation results of the emission carbon content ($[PAC]_{out}$) as a function of ESP's FA collection efficiency (η_{FA}). In the calculation it is assumed that 0.5% PAC by mass was mixed with the FA in the flue gas upstream of the ESP, and the ESP's PAC collection efficiency (η_{PAC}) either had a constant differential with η_{FA} (η_{FA}-η_{PAC}=const.), or was a constant fraction of η_{FA} (η_{PAC}/η_{FA}=const.). From the figure it can be found that for both η_{PAC} assumptions, as η_{FA} approaches 100%, there will be significant carbon content increases (up to 60%) in the emission. Modern ESPs generally have η_{FA} larger than 95% or even larger than 99% (Cooper & Alley, 2011), so it is reasonable to claim that the installation of ACI technologies will significantly increase the carbon content in the CFPPs' emissions. If PAC and FA particles do not agglomerate as discussed in Section "*Physical characterization of FB emissions*", the increased carbon content will be emitted as individual carbonaceous particles, which makes CFPPs a new source of BC emissions. This new BC source is a large-scale point source, generally operated under steady state conditions yielding relatively steady BC emissions, which is quite different from most of the conventional BC sources that are believed to be either small and numerous, or large but episodic (Bond et al., 2013). Due to CFPPs' nature of relatively steady emission, BC emission should be monitored by CFPPs with ACI installed and the international BC emission inventories for CFPPs should be established for the emission control and simulation of climate forcing associated with BC emissions from CFPPs, in a way that cannot be done with other BC sources.

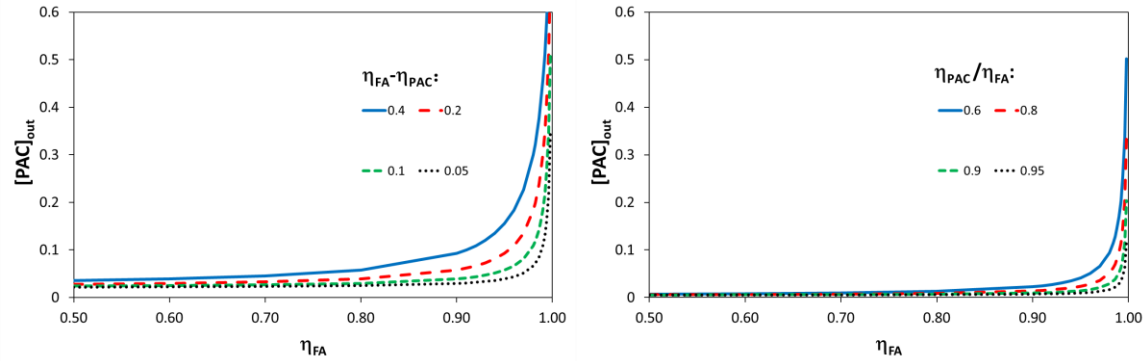

(a) (b)

Figure 3. 8 Calculated ESP emission carbon contents as function of η_{FA} assuming (a) η_{FA}-η_{PAC}=const. or (b) η_{PAC}/η_{FA}=const..

The calculation and figure presented in this section was performed by Prof. Herek L. Clack as a part of this research project.

3.7 Conclusions, Limitations and Future Work

This research measured B_{abs}, B_{scat} and mass loadings of combustion-generated soot as well as FA/FA-PAC aerosols emitted from a fluidized bed, and calculated the corresponding MSC, MAC and SSA of soot, FA aerosols and FA-PAC admixture aerosols. For the relatively large PAC and FA particles sampled in the experiment, the SEM images indicate agglomeration in the flue gas is unlikely. Both MSC and MAC of FA-PAC admixture aerosols would increase linearly with the increase of particles' carbon content, while the increase of carbonaceous particles in the FB emissions had a more significant effects on the MAC of the particles in the emissions, and the SSA would decrease linearly with the carbon content increase. The acquired MAC value of soot is relatively low compared with other reported values, which may be due to the small size of

the oil lamp flame, and the acquired SSA values for both soot and FA are comparable with other relevant reports. The measurements and calculations illustrated that the installation of ACI in CFPPs would increase the MAC of the emissions from the power plants and make the CFPPs a new source of light absorbing particle emissions. Although large in average size, the emitted PAC particles, especially the submicron fraction, can absorb light efficiently and potentially act like BC in the atmosphere. Further studies should be conducted to quantify the intensity of this new emission and examine its potential climate forcing effects.

Several limitations have been observed during the research. The measurements conducted for FB emissions only sampled relatively large particles since the smaller particles may have been exhausted during the free elutriation of the FB before any measurements, and the size distributions of the sampled particles were not fully examined. In future a dilution chamber should be built downstream of the FB to capture and dilute the small particles emitted by the FB during the early stage of fluidization for PAX measurements, and scanning mobility particle sizer spectrometer (SMPS) should be utilized to further examine the size distribution of sampled particles. Last but not least, since most CFPPs use industrial opacity sensors to monitor their PM emissions, the light extinction measured by PAX and industrial opacity sensors should be compared to examine the effectiveness of opacity sensors on detecting carbon emissions from CFPPs.

CHAPTER IV SUSPENDING VIRAL AEROSOLS IN AN AIRSTREAM THROUGH ULTRASONIC ATOMIZATION

4.1 Ultrasonic Atomization of Virus Suspended in Bulk Liquid Solution

4.1.1 Short review on the research background and methodology

The study of airborne disease transmission is challenging despite the substantial public awareness and concern that accompanies outbreaks of airborne infectious diseases. In order to study the airborne transmission of pathogens, and particularly in studying strategies for their containment or inactivation, expertise is needed in virology, epidemiology, fluid mechanics, and aerosol dynamics, areas not commonly united within a single discipline as noted by Peccia et al. (J. Peccia, Milton, Reponen, & Hill, 2008). Studying the spontaneous or engineered inactivation of airborne pathogens requires suspension of the pathogen in air, which can be non-trivial. Some viruses and bacteria can be suspended in air by a conventional spray drying process in which the pathogen is dispersed in a volatile liquid solution, the liquid solution is atomized after which the liquid phase of the resulting droplets rapidly evaporates leaving the viral or bacterial pathogen suspended in air along with any dissolved minerals. Widely used for such purposes is the Collison nebulizer which uses a high velocity gas flow to shear the solution into a liquid film that breaks up into a spray. All such airblast or air assist atomization processes, however, produce sprays droplets that are polydisperse in size (A. H. Lefebvre, 1980, 1989). The distribution of droplet sizes causes distributed, size-dependent droplet behavior and transport, from gravitational settling velocity to the time required for complete evaporation. Low-pass filtering of the droplets,

such as cyclonic separation, reduces but does not eliminate the polydispersity which is a complicating factor in designing and operating experiments to consider the inactivation or survival of infectious aerosols in air. Ultrasonic atomization produces a much narrower distribution of particle sizes, leading to more uniform droplet behavior and transport. Specialized ultrasonic atomizers used for these purposes can be expensive, particularly when viewed in the context of commercial-grade ultrasonic air humidifiers that operate on similar principles but cost much less. More detailed discussion of this research background can be found in Section 1.3.2.1.

The objective of this research is to describe the method and necessary conditions required to successfully use a consumer-grade ultrasonic (aka "cool mist") air humidifier to suspend viral aerosols in flowing airstreams in the service of studying airborne pathogen inactivation. A sampling train as shown in Figure 2.1 was constructed, and MS2 (a single-stranded RNA bacteriophage) suspended in virus dilution buffer (VDB) was used to generate viral aerosols from a consumer-grade ultrasonic humidifier. The survival of MS2 in the humidifier reservoir and aerosolized in the sampling air were examined by plaque assay analysis. The temperature and relative humidity (*RH*) of the air stream inside the sampling train was measured by a portable humidity/temperature pen (Traceable 4093), the temperature increase of the VDB solution inside the humidifier reservoir was measured by a thermometer (TrueTemp 3516), and the power consumption of the humidifier was measured by an electricity usage monitor (P3 International P4460) over the range of eight built-in power settings (labeled as H1-H8 in this paper) of this humidifier model. The research methodology is illustrated in detail in Section 2.2.1.

4.1.2 Performance of the humidifier

The model of humidifier used has eight user-selected power settings, referred to here as H1-H8. Over the range of power settings available, Figure 4.1a shows plots of measured electric power consumption and atomization rate of the humidifier. Both quantities increased linearly with increasing power level: for each power setting detent, power consumption increased by 1.3 W, and the average atomization rate increased by 57 ml/h. The trend line for power consumption indicates that at power Level 0 (Humidifier_Off), the humidifier would still consume 26 W of electricity, which represents the baseline power consumption of the other components of the humidifier such as the internal ventilation fan used to draw air into the device. Figure 4.1b shows the correlation between the humidifier atomization rate and the measured relative humidity in the air stream immediately upstream of the reactor after evaporation of the generated mist (constant air flow rate of 170 LPM). The *RH* increased linearly with the increasing atomization rate, and for each 100 ml/h more water atomized, the *RH* would increase by 9%. It was predicted that the *RH* would reach 100% upstream of the reactor if the atomization rate was increased to 500ml/h, which is unlikely for the current humidifier (maximum atomization rate was estimated to be 450 ml/h at H8).

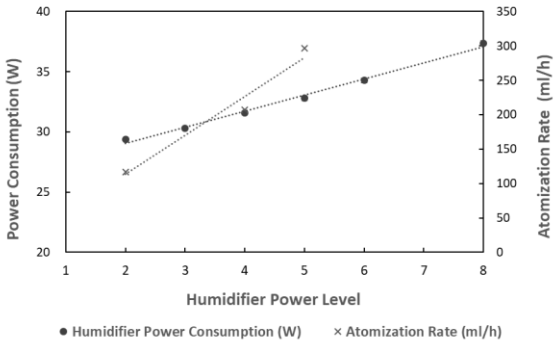

(a)

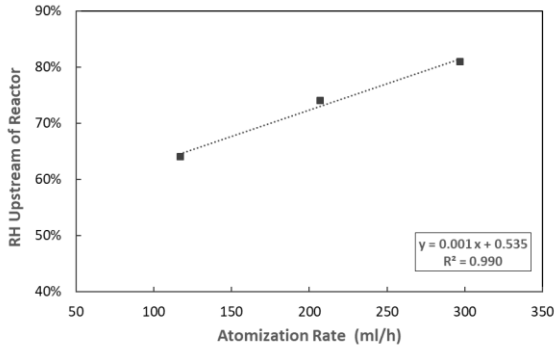

(b)

Figure 4. 1 Measured performance of the humidifier. (a) Humidifier power consumption and atomization rate as a function of power levels; (b) The final RH upstream of the reactor as a function of atomization rate.

One major concern of utilizing the consumer-grade ultrasonic humidifier to atomize virus solutions is that the vibration of piezoelectric transducer may increase the virus solution temperature rapidly and cause virus inactivation. Figure 4.2 shows the measured solution temperature increase inside the reservoir over 60 minutes at three humidifier settings (Humidifier_Off, H2, and H5). When the humidifier was off, the solution temperature increased gradually by 4 ℃ over the one-hour period, mainly due to the heat exchange with ambient air. At H2, however, the solution temperature increased rapidly by 12 ℃ during the first 20 minutes and then increased relatively gradually by 6 ℃ in the next 40 minutes. The much more significant temperature increase could be caused by the dissipation in the fluid of the vibrational energy generated by the piezoelectric transducer. In addition, the ventilation by the internal fan when the humidifier was on promoted heat transfer between the solution in the reservoir and ambient air, which is initially warmer and thus could warm the solution rapidly. When the power level was increased to H5, the temperature increase profile did not differ much from that at H2: during the first 20-30 minutes, the temperature increase at H5 was about 2 ℃ faster, while the final temperature increase at 60 minutes was nearly the same. The small difference between the temperature rises of the solution in the reservoir at different humidifier settings may indicate that ventilation should be the major cause of the initial rapid temperature rise in the humidifier reservoir, rather than the atomization process.

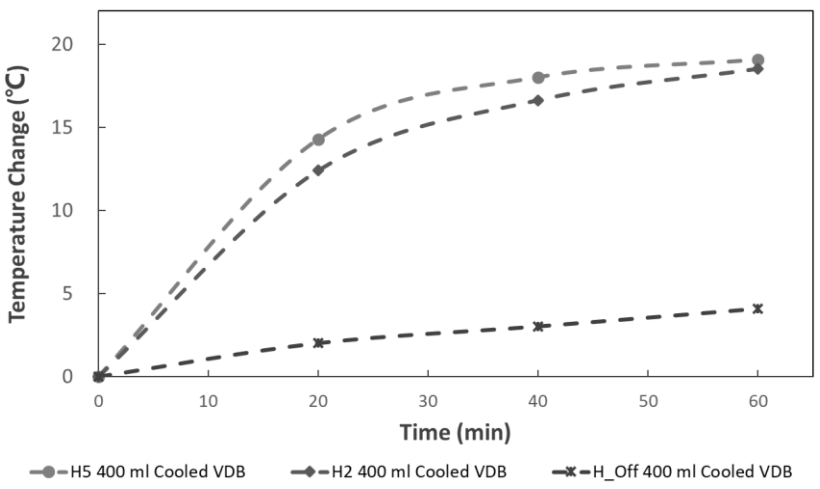

Figure 4. 2 Temperature increase of cold (~5℃) VDB inside the humidifier reservoir during the 60-minute atomization tests at three power settings.

4.1.3 MS2 inactivation during the atomization process

Figures 4.3 shows the inactivation of MS2 in the ultrasonic humidifier reservoir over a 65 minute atomization period at H2 compared to the temperature in the reservoir. From the figure it is evident that the concentration of infectious MS2, in terms of plaque forming units (PFUs) determined from plaque assay, showed no significant decrease as long as the temperature of the VDB in the reservoir remained below about 20 ℃. Once the temperature exceeds 20 ℃, concentrations of infectious MS2 decreased markedly with increasing temperature, ultimately resulting in approximately a 1.2 log reduction in infectious MS2 after 65 minutes. When active cooling was employed in the form of adding a small packet of water ice, this inactivation was significantly reduced. Although the temperature of the VDB still exceeded 20 ℃ eventually, slower initial rates of increasing VDB temperature in the reservoir translated into negligible inactivation of MS2 and largely unchanged concentrations of infectious MS2 over the first 35 minutes (Figure 4.3b). Only approximately 0.3 logs inactivation was observed after 65 minutes

with active cooling in the reservoir. The relatively unchanged infectious MS2 concentrations while the VDB temperature remained below 20 ℃ indicated that MS2 was mainly inactivated by the increase in solution temperature during the tests, while the vibration of the piezoelectric transducer inside the reservoir likely had minimal effects on the survival of the virus. The temperature increase during ultrasonic atomization was not a new discovery. Phipps et al. (Phipps et al., 1990) and Niven et al. (Niven et al., 1995) both reported similar temperature increases with ultrasonic nebulizers atomizing saline solution or enzyme stabilizing solution, and Niven et al. also observed the inactivation effect of heating on enzyme viability.

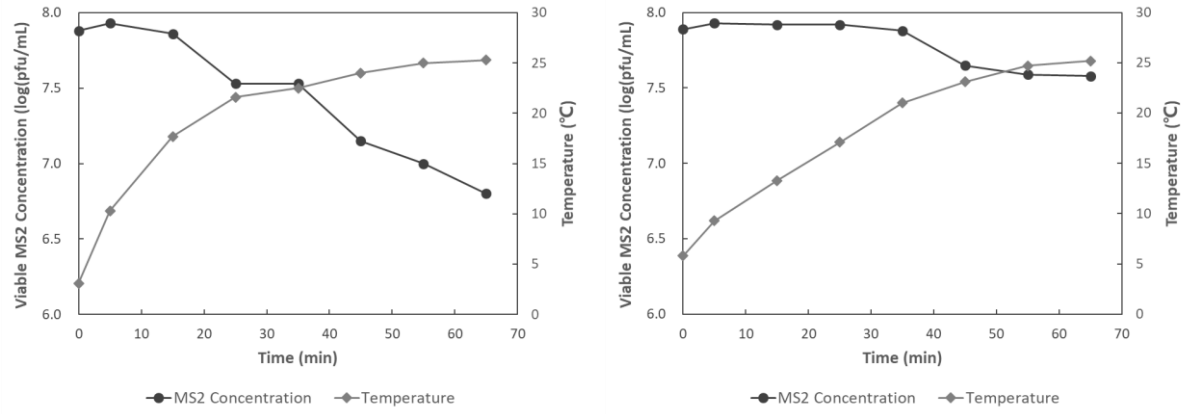

(a) (b)

Figure 4. 3 MS2 Inactivation in humidifier reservoir (a) without and (b) with active cooling.

4.1.4 Performance of MS2 Atomization

Figure 4.4 compares the estimated infectious MS2 concentrations in air stream (pfu/L) at the humidifier outlet with the in-air concentrations at the upstream impinger sampling point in seven tests conducted during the study. The atomization period was set to 30 minutes and no active cooling was applied since according to Figure 4.3a, the inactivation of MS2 in the first 30

minutes should be below 0.2-log. The approximate infectious MS2 concentrations at the humidifier outlet were between 10^5 to $10^{5.5}$ pfu/L, and the estimated infectious MS2 concentrations at the upstream impinger sampling point were between 10^2 to 10^3 pfu/L. The relatively consistent results with small standard deviations for seven tests proved that the atomization process was quite repeatable. As MS2 was aerosolized from VDB by the humidifier and traveled from the humidifier outlet to the upstream sampling point (3.7m in distance), an average of 2.6-log reduction in infectious MS2 concentration in air was observed. The qPCR results (showed in Figure 5.3), which reflect the total (infectious and inactivated) number of viruses in the sample, suggested a decrease of ~1 log between the humidifier outlet and upstream impinger likely due to physical aerosol removal such as duct wall impaction. The additional 1.6-log reduction in infectious MS2 concentration should be caused by the evaporation process of the atomized MS2-VDB droplets. The VDB solution was prepared by dissolving several salts in MilliQ water. The fine mist of VDB droplets generated by the humidifier and injected into the air flow underwent evaporation of water, causing a brief period in which the salinity of the droplets containing MS2 increased significantly. It is hypothesized that this high salinity condition contributed to the inactivation of a substantial fraction of MS2 from the humidifier reservoir to the suspension of the virus in the air stream. The condensation and impaction of VDB droplets on duct walls and the MS2 inactivation inside the humidifier reservoir can also contribute to the 2.6-log inactivation, while their effects may not be as significant. Although a substantial fraction of MS2 was inactivated by the atomization process, the atomization process can still be considered successful since 10^2-10^3 pfu/L MS2 aerosols were generated consistently by the humidifier. In this project, MS2 atomization at power level H5 was studied as well, but a much more substantial (4-log) inactivation was observed from the humidifier reservoir to the impinger

sampling point. It is hypothesized that the more rapid temperature increase and greater acoustic energy produced inside the humidifier reservoir caused this further MS2 inactivation. Research by Niven et al. (Niven et al., 1995) illustrated a similar mechanism where the studied enzyme in the nebulization solution was inactivated by the combined effects of heating and aerosol formation.

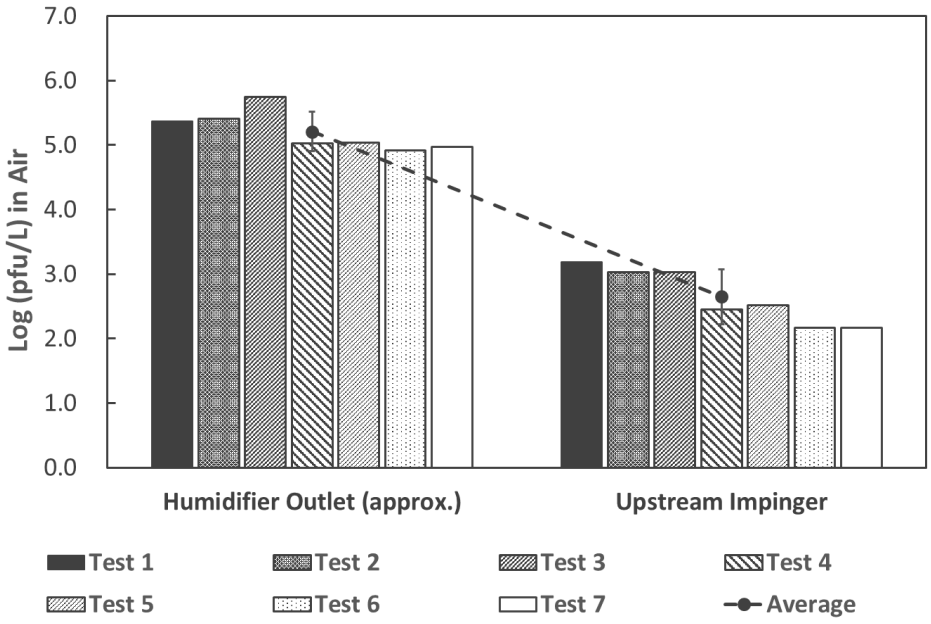

Figure 4. 4 Estimated infectious MS2 concentrations in air stream at the humidifier outlet and the upstream impinger sampling point in seven 30-minute tests.

4.1.5 Conclusions and Future Work

This study examined the method and necessary conditions needed to successfully use a consumer-grade ultrasonic air humidifier to suspend viral aerosols in flowing airstreams in the service of studying airborne pathogen inactivation. A numerical model was constructed to predict the evaporation process in the air flow of fine droplets emitted from the ultrasonic air

humidifier with narrow particle size distributions, and a series of experimental tests were designed and conducted to examine the performance of the humidifier in suspending MS2 into the flowing airstream. The numerical modeling results proved that for the much more uniform, finer mists produced by ultrasonic atomization, the droplet evaporation process can be modeled, and therefore designed, with precision. The nonlinear influence of evaporative cooling and increasing moisture content of air to which aqueous droplets are injected were shown to lead to highly nonlinear, rapid variations in the rate of droplet evaporation, including the onset of water vapor saturation. For several initial dew point temperatures of the intake air, the modeling results illustrated acceptable ranges for the air-to-liquid ratio to avoid the sudden onset of water vapor saturation when aerosolizing biological pathogens from aqueous solutions. These results should be revisited when considering solutions having higher concentrations of dissolved solids due to their effect on the vapor pressure of the solvent vapor above the solvent liquid. The experimental results proved that the commercial-grade ultrasonic air humidifier used in this study can consistently suspend 10^2-10^3 pfu/L dry MS2 aerosols into the 170 LPM air flow at its low power setting (H2). The average virus solution atomization rate increased by 57 ml/h when the built-in humidifier power level was increased by one, and for each 100 ml/h more solution atomized, the *RH* in the airstream would increase by 9%. During atomization, the ventilation of ambient air into the humidifier reservoir can cause temperature rise of the virus solution inside, but MS2 would not be largely inactivated as long as the temperature remained below about 20 C. The vibration of piezoelectric transducer inside the humidifier reservoir would not cause significant solution temperature rise and should have minimal effects on the survivability of virus inside the humidifier reservoir. An average of 2.6-log reduction in infectious MS2 concentration in air were estimated, mainly due to the evaporation process of atomized MS2-VDB droplets. In future,

ways should be examined to minimize this evaporation-induced inactivation, and the performance of the humidifier in atomizing other virus solutions should be studied, since different virus solutions may vary in viscosity, which can significantly affect the atomization rate of the humidifier.

4.2 Real-time in situ Monitoring of Ultrasonic Atomization Rate by Light Attenuation Measurements

4.2.1 Short review on the research background and methodology

As discussed in Section 4.1, it is possible to aerosolize viruses or bacteria through ultrasonic aerosolization with a consumer-grade ultrasonic humidifier. The system, however, can still be improved by including a real-time atomization rate monitoring system. To achieve real-time *in situ* atomization rate monitoring, the most common and nondestructive method is measurement of light extinction, or attenuation. As the beam of a laser passes through an aerosol suspension, the light intensity is attenuated due to light scattering and absorption by particles. The degree of light attenuation or extinction is dependent on the particle number density and particle size, thus the measurement of light extinction can serve as a real-time nondestructive indication of number concentration and size distribution of particles suspended in the sampled airstream. To calculate corresponding particle number concentrations from light attenuation data, Beer–Lambert law can be used even without forward scattering correction. Lee and Clack (E. M. Lee & Clack, 2010) illustrated that a simple *in situ* laser-photodiode system is sensitive and accurate to measure mass concentration and size distribution of suspended carbonaceous particles for detection of particle agglomeration. In industry, opacity (derived from light extinction measurement, $opacity = 1 - I/I_0$) sensors are installed as a standard equipment to continuously monitor particulate matter

(PM) concentrations in smoke stacks (USEPA, 2000). Detailed literature review of the background of this research is included in Section 1.1.4 and Section 1.3.2.2.

The objective of the present study is to develop a system for measuring *in situ* and in real-time the virus solution atomization rate from a consumer-grade humidifier, rates whose values are essential for producing air flows containing consistent concentrations of bioaerosols. The approach uses a laser and photodiode to measure light attenuation similar to that developed by Lee and Clack (E. M. Lee & Clack, 2010), and Arduino, a novel open-source electronic prototyping platform, was employed as the data logger. Various virus solutions were atomized by the humidifier, with the real-time atomization rate monitored by light attenuation measurements and average atomization rate estimated by measuring the change in fluid level in the humidifier reservoir with time. The voltage across the photodiode circuit was measured by the Arduino built-in voltmeter and the data were acquired and analyzed using the Arduino programming software. The research methodology is illustrated in detail in Section 2.2.2.

4.2.2 Repeatability assurance

Figure 4.5 shows the average photodiode voltage registered without any obscuration of the laser beam,V_0, for two groups of three consecutive tests at Position 2 (upstream of the humidifier outlet, as shown in Figure 2.2). At the beginning of each test, V_0 always returned to a similar value, ranging from 16 mV to 17 mV, and there was no obvious increasing trend of measurement bias. The results proved that the light extinction system constructed in this study is accurate and reliable for continuous or repeated atomization rate measurements, and the accumulation of liquid droplets on outlet chimney walls would not affect measurement results when the optical

bench was installed at Position 2, since the diameter of the pinhole (3mm) is much larger than the diameter of the laser beam (0.46mm).

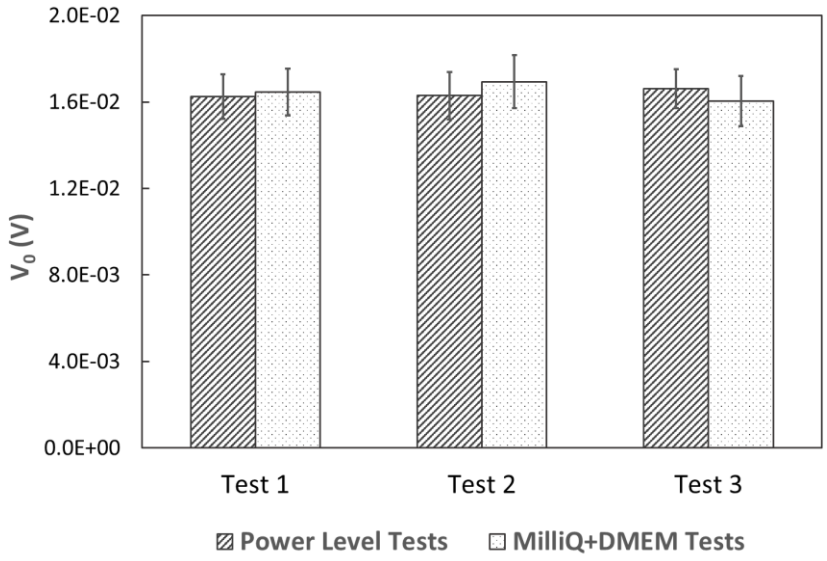

Figure 4. 5 Average V_0 for two groups of three consecutive tests at Position 2. All of these tests reported similar V_0 values and no increasing trend was observed for error bars.

4.2.3 Real-time *in situ* measurement of atomization rate

The conditioned V/V_0 signal from the photodiode at Position 1 is displayed in Figure 4.6. The raw signal produced by the photodiode exhibited a 1 Hz noise component that likely was generated in the photodiode circuit and/or on the Arduino platform. Signal conditioning involved using a 20-point averaging function in data analysis software Origin^{TM}. When no atomization was occurring (the first 400 seconds in Figure 4.6a and the first 500 seconds in Figure 4.6b), $V/V_0 \sim 1.0$, with the small fluctuations mainly attributed to noise. When the humidifier was turned on, V/V_0 for all four tests in Figure 4.6a had rapid and significant drops, indicating high atomization rates and droplet density and the ability of the system for rapid detection. V/V_0

decreased with increasing humidifier output setting, which is reasonable since increasing humidifier output increased the atomization rate, leading to more droplets generated per unit time and greater light attenuation. V/V_0 displayed in Figure 4.6b, however, had a much more gradual and less significant reduction when the atomization started, indicating much smaller atomization rates in these tests as compared to test results presented in Figure 4.6a.

V/V_0 increased by about 11% when the proportion of DMEM in the bulk solution was increased from 0% to 30%, while no obvious increasing trend was observed when the DMEM proportion was further increased from 30% to 50%. The results indicated that the addition of glucose and other organic compounds into MilliQ water would significantly reduce the ultrasonic atomization rate at constant piezoelectric transducer frequency and power, and the atomization rate reached the lowest measured value (~0.7ml/min) when about 30% of DMEM was added. These observations agree with literature. Data reported by Vazquez et al. (Vázquez, Alvarez, & Navaza, 1998) and Telis et al. (Telis, Telis-Romero, Mazzotti, & Gabas, 2007) proved that the addition of glucose into sodium carbonate + sodium bicarbonate solutions or distilled water would cause increasing liquid viscosity. McCallion et al. (McCallion et al., 1995) reported that ultrasonic atomization was affected by liquid viscosity, and increasing liquid viscosity generally led to decreasing ultrasonic atomization rate. In this study, the viscosity of virus solution increased as more DMEM was added, causing reduction of ultrasonic atomization rate and the density of droplets in the generated mist, what was furthermore reflected in a reduction in light attenuation as measured by the photodiode. In all tests, V/V_0 did not reach a steady state and continued to decrease with time, which means that the humidifier atomization rate was never constant. Instead, the atomization rate kept increasing during each test. This is likely due to the

temperature increase of the bulk solution in the humidifier reservoir. The bulk solution temperature increase during ultrasonic atomization has been observed and discussed in detail in previous studies (Niven et al., 1995; Xia et al., 2018), and the viscosity of both water and glucose solution is inversely related to liquid temperature (Kestin, Sokolov, & Wakeham, 1978; Telis et al., 2007; Vázquez et al., 1998). In this study, increasing temperature during ultrasonic atomization led to decreasing liquid viscosity in the humidifier reservoir, which led to the increasing atomization rate during all tests. Light attenuation measurements at Position 2 yielded plots similar to Figure 4.6 (not shown). In all, Figure 4.6 proved that the system constructed in this study was a fast and accurate way to monitor in real-time light attenuation due to droplet mists produced by ultrasonic atomization of bulk solutions, and was capable of indicating a change in atomization rates reflecting scenarios likely to change bulk liquid properties. The Arduino platform can be a low cost and programmable data logger for real-time monitoring systems, and its built-in voltmeter was sensitive enough for the objective of this study.

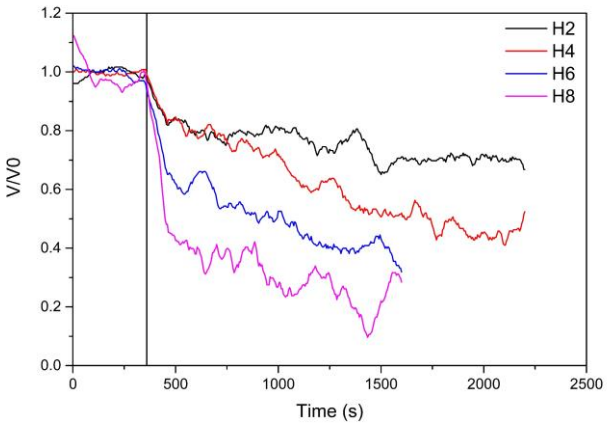

(a)

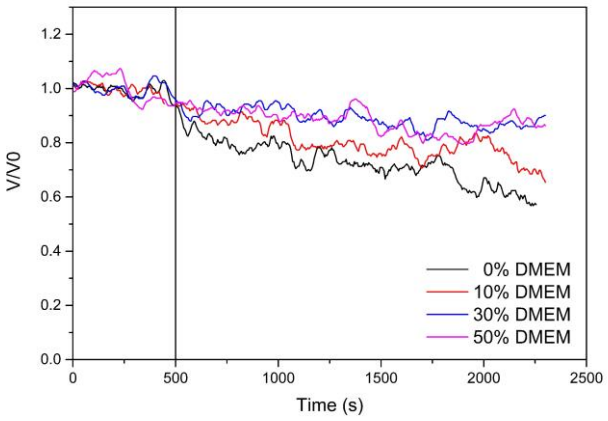

(b)

Figure 4. 6 Real-time measurements of V/V0 at Position 1 with the consumer-grade humidifier atomizing (a) 200 ml MilliQ water at four power levels, or (b) 200 ml MilliQ + DMEM solution with four mixing ratios at power level H2. Vertical lines indicate the start of atomization.

For each test, average values of V/V_0 during the atomization period were calculated and the resulting $-\ln(V/V_0)$ values were plotted against estimated average atomization rate in Figure 4.7. Strong linear correlations were found for measurements at both optical bench positions. At Position 2, droplets were more concentrated in the outlet chimney before being emitted into the open air. As a result, measured V/V_0 values at Position 2 were lower than values measured at Position 1 at the same atomization rate, and the resulting $-\ln(V/V_0)$ values were higher. The strong linear correlation proved that the assumptions made for derivation of Equation 3 were valid, and Beer–Lambert law can be applied for this light attenuation monitoring system without additional corrections. All measurements taken at the same optical bench position fall onto a common line, regardless of bulk liquid properties, which means that the light attenuation measurements were independent of droplet liquid properties, and the system can be applied for

different atomization methods aerosolizing various virus or bacterial solutions. When the atomization rate was over 3 ml/min, the attenuation of the laser beam was so high that the energy reaching the photodiode approached its lower detection limit, resulting in measurement error indicated by the large error bars in Figure 4.7. In all, the system is effective and accurate in measuring ultrasonic atomization rate within the range of 0.7 ml/min to 3 ml/min. The optical bench measured real-time V/V_0 during atomization, which can be correlated to real-time atomization rate using the linear trend line functions presented in Figure 4.7, making real-time *in situ* monitoring of ultrasonic atomization rate from a consumer-grade humidifier possible without destructing or obstructing the sampling air flow.

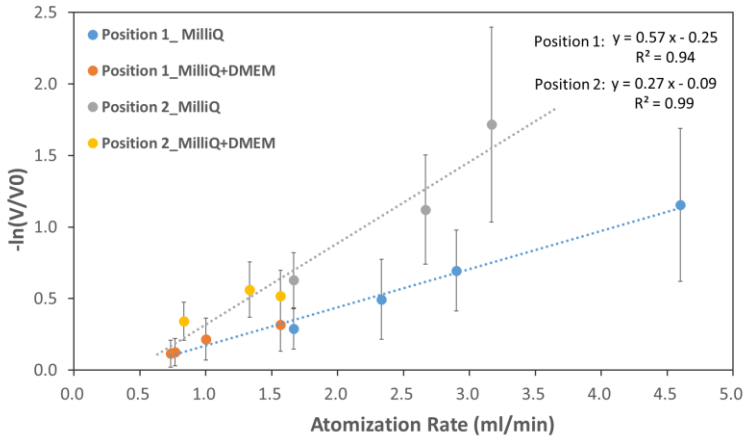

Figure 4. 7 Correlation between $-\ln(V/V_0)$ and the average atomization rate for all tests at both optical bench installation positions.

4.2.4 MS2 Survival during Laser Exposure

To examine if the laser source used in this study can inactivate MS2, a group of batch tests with 1ml MS2 samples exposed to the laser radiation for 1s to 300s was conducted, and the resulting viable MS2 concentration in each sample was analyzed by plaque assay. The exposure test results, together with the control test results, are displayed in Figure 4.8. From the figure, it is

evident that viable MS2 concentration remained constant (~4×10^7 pfu/ml) over exposure times from 1 to 300 seconds, which implies that exposure to the laser energy of this intensity (0.8 mW rated power, 5 mW maximum power) for up to five minutes, far more than the momentary exposure as the mist traverses the laser beam, would not cause detectible MS2 inactivation. Comparison between exposure and control tests at 60s and 300s also support this assertion: after 1- or 5-minute laser exposure, viable MS2 concentrations were only 0.08-log and 0.06-log lower than the concentrations in corresponding control samples respectively, which was within the plaque assay measurement error. In the mist produced by the ultrasonic humidifier, droplets containing MS2 experienced exposures of fractions of a second to the laser (<<1s), so according to the results presented in Figure 4.8, it is reasonable to conclude that such exposure would not cause detectible inactivation of aerosolized MS2 in the airstream.

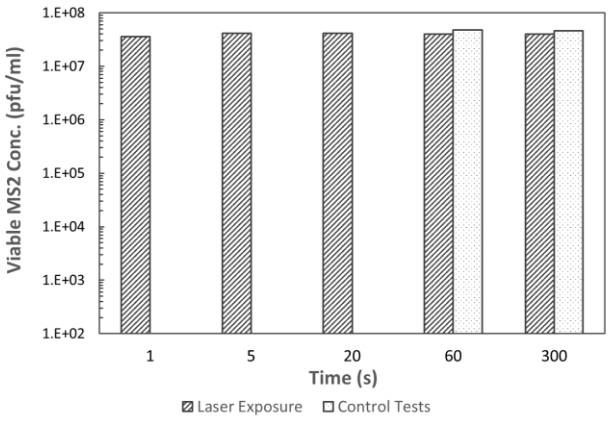

Figure 4. 8 Survival of MS2 during 1s–300s laser exposure. The results proved that the laser radiation applied in this study would not cause detectable MS2 inactivation during up to five minutes exposure.

4.2.5 Conclusion and Future Work

In summary, for the purpose of developing an in situ monitoring system measuring real-time virus solution atomization rate from a consumer-grade humidifier and demonstrating a simple and low cost method for in situ sensing of atomized bioaerosols for various bioaerosol studies, an optical system was constructed with laser-photodiode light attenuation measurements and an Arduino platform as the voltmeter and data logger. Various virus solutions were atomized by the humidifier at different power levels, light attenuation was measured as V/V0 and the average atomization rate was estimated by measuring the total liquid volume reduction in the humidifier reservoir over the atomization period. The results proved that light attenuation measurements and Arduino platform were reliable for continuous or repeated atomization rate monitoring. The system developed in this study was fast and accurate to monitor real-time light attenuation, and was able to indicate change of ultrasonic atomization scenarios due to changes of bulk liquid properties. The system was effective in indicating real-time ultrasonic atomization rate within the range of 0.7 ml/min to 3 ml/min, and the Beer–Lambert law and Equation 3 was proved to be valid for the current setup without additional corrections. Exposure to laser applied in this study would not cause unintentional MS2 airstream inactivation. In future, ultra-transparent cap can be installed on the pinhole to completely prevent potential droplet leakages and an adjustable piezoelectric transducer, which can be tuned to atomize glucose solution effectively, should be installed for successful aerosolization of viruses suspended in MEM.

CHAPTER V INACTIVATION OF AIRBORNE VIRUSES BY A PACKED BED NON-THERMAL PLASMA REACTOR

5.1 In-flight Inactivation of MS2 by Non-thermal Plasma

5.1.1 Short review on the research background and methodology

Airborne disease transmission, the processes governing it, and the development of protective measures against it, are less understood than transmission via water, food, arthropod vectors, and direct contact with infected individuals. Disease transmission among humans and animals often involves either direct contact with an infected individual or transport across very short distances; however, pathogen transmission over longer distances can also occur. For food industry, livestock diseases such as Newcastle disease, avian influenza, hoof-and-mouth disease, porcine reproductive and respiratory syndrome (PRRS), and African swine flu are potential threats to global food security.

In contexts where humans or animals move freely, the potential for disease transmission through direct contact is greater, reducing the importance of airborne transmission and greatly limiting the utility of airborne pathogen inactivation. However, where airborne transmission is or is suspected of being an important transmission route, few mitigation technologies exist. UV germicidal irradiation (UVGI) and conventional HEPA filtration are common available technologies which can prevent airborne transmission from outdoor to indoor environment, but both technologies present several drawbacks. Two factors govern the potential for disease

transmission by airborne pathogens such as viruses and bacteria: aerosol *transport* and aerosol *infectivity* (Pitkin, Deen, & Dee, 2009). UV radiation alone only addresses aerosol infectivity and particle filtration only addresses aerosol transport. Unlike filtration and UV irradiation, non-thermal plasmas (NTPs) can address *both* transport (by charge-driven filtration) *and* infectivity (by reaction with reactive plasma species) of airborne pathogens. Researchers (N.D. Vaze et al., 2007; Y. Wu et al., 2015) have reported reductions in infective airborne pathogen concentrations as a result of NTP treatment, results that included confounding effects of extended exposure of viral aerosols to ozone (N.D. Vaze et al., 2007) or loss of viral aerosols by charge-driven filtration (Y. Wu et al., 2015). The background of this research is discussed in detail in Section 1.3.1 and Section 1.3.3.

The objective of this research project is to develop a non-thermal plasma in-flight airstream disinfection system and contributing to the scientific understanding of generating non-thermal plasma at atmospheric pressure, and the spontaneous inactivation of airborne viruses in a plasma environment. A dielectric barrier discharge (DBD) non-thermal plasma reactor was constructed to treat an air stream seeded with viral aerosols remaining after the evaporation of fine mists produced by the ultrasonic atomization of solutions of MS2 phage in virus dilution buffer (VDB). Plaque assay and quantitative polymerase chain reaction (qPCR) analyses were used to determine the pre- and post-treatment abundance of infective MS2 aerosols and the viral genomes to separately evaluate aerosol filtration from virus inactivation. Ultimately, the ability to remove residual ozone with carbon filters was assessed by measuring ozone concentration downstream of the reactor with an ozone sensor (EcoSensors A-21ZX). The research methodology is described in detail in Section 2.3.1

5.1.2 Sampling Train Operating Conditions

Figure 5.1 shows measured radial velocity profiles downstream of the packed bed in the duct at different ID fan voltage settings (30%, 60% and 100% of 120V). The figure indicates that the airflow through the 3" ID duct was close to a plug flow, with the maximum velocity at the duct centerline, decreasing more significantly near the duct wall than near the centerline. Integrating the measured air velocity values along the profile yielded an estimation of the overall air flow rate through the sampling train of 170 liters per minute (LPM) at the 30% setting of the ID fan.

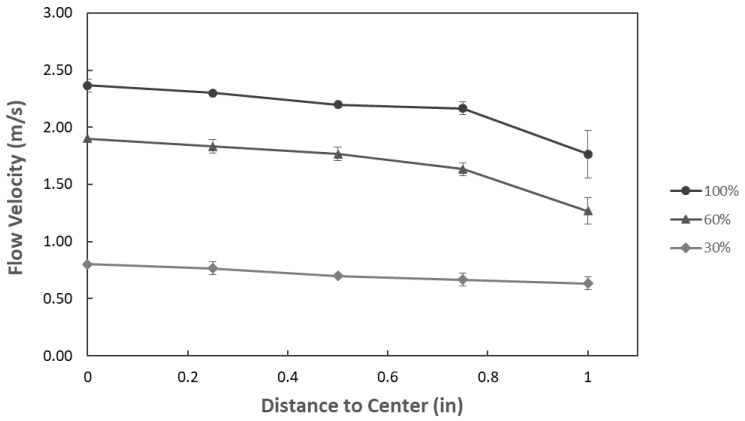

Figure 5. 1 Measured radial velocity profile downstream of the NTP reactor packed bed at different ID fan voltage levels.

The pressure difference upstream and downstream of the NTP DBD packed bed measured at the flow rate of 170 LPM was 45 Pa, reasonably low due to the porosity of the packed bed. The ozone filter was also quite porous, with a honeycomb structure that produced a pressure drop of 20 Pa at the flow rate of 170 LPM. The total pressure drop across the system was about 65 Pa at the flow rate of 170 LPM, or 0.38 Pa/LPM. It was estimated that at 170 LPM, the virus exposure time to NTP species was about 0.25s.

For the power consumption of the reactor, while 20-30 kV was applied across the electrodes of the NTP reactor the corresponding current was on the order of 0.1 mA and as a result the overall power consumption of the reactor was typically in the single-digit watt range. For the Trek high voltage supply system providing voltage at 20 kV, the power consumption as indicated by the oscilloscope was only 1.7 W (600 J/m^3 at 170 LPM). For the fixed 30kV supply, the power consumption was 21 W (7400 J/m^3 at 170 LPM) measured by the commercial power meter.

When supplementing ambient air with dry compressed air, the temperature and RH of the air stream inside the sampling train were 20℃ and 30%, respectively, prior to the introduction of the mist formed from the water mist. The addition of water mist from the humidifier into the air stream can induce evaporational cooling, in which the air temperature would be reduced and the RH would be increased. According to the measurement data, when water mist was injected into the air stream (170 LPM) at humidifier power Level 2 (H2) (atomization rate of 117ml/h), both the temperature and RH reached steady state values of 16.5℃ and 60% respectively after 30 minutes.

The plaque assay results of the quality control test, in which 20ml of $1x10^6$ pfu/mL MS2-VDB solution was added into the downstream impinger and the effluent gas from the reactor (either off or powered by 20 kV supply) was bubbled through the impinger liquid, are presented in Figure 5.2. The constant concentration presented when the NTP reactor was off proved that when bubbling ozone-free air through the impinger (reactor off), the virus in the impinger liquid would not be inactivated during the 45-minute testing period. Compared with reactor off results, reactor on results in Figure 5.2 illustrated a 3-log reduction of viable MS2 in the impinger during the

first 15 minutes. This indicated that when the reactor was activated by 20kV voltage supply, ozone was generated, which can dissolve into the impinger liquid and cause inactivation of sampled MS2. To quench the dissolved ozone, 50mM of sodium sulfite anhydrous was added into the downstream impinger collection liquid. According to the measured ozone concentration in the airstream and a numerical model of ozone dissolution, the added sodium sulfite should be in excess of the amount needed to quench all the potentially dissolved ozone during the packed-bed NTP inactivation tests. It was proved that the addition of 50 mM of sodium sulfite into the impinger collection liquid would not cause any detectable MS2 inactivation in two hours.

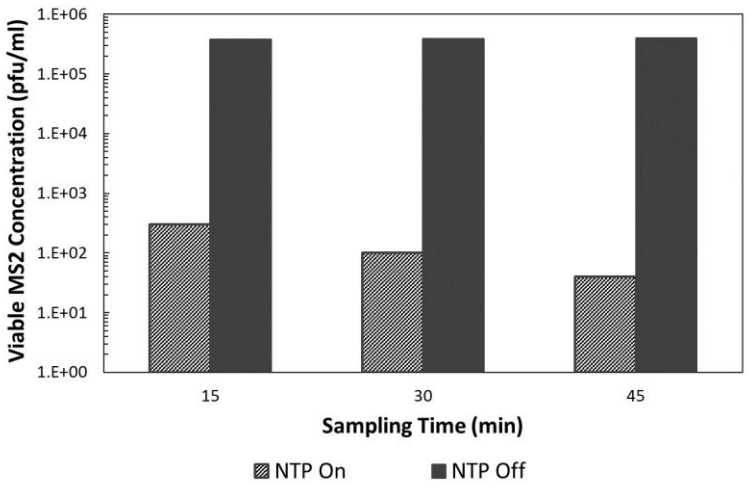

Figure 5. 2 Change of infectious MS2 concentration in the downstream impinger with either ozone-free air (reactor off) or ozone-loaded air (reactor activated by 20kV) bubbling through the impinger liquid.

5.1.3 MS2 Inactivation

The decrease in infective MS2 particles and total MS2 particles across the reactor were assayed by taking samples from the atomizer reservoir (representing infective MS2 concentrations in the

bulk virus buffer solution) and samples from both the upstream and downstream impingers (representing infective MS2 concentrations pre- and post-NTP treatment). Although plaque assay results are normally reported in pfu per mL of solution and qPCR results in genome copies (gc) per mL of solution, our reported concentrations are in pfu per liter of air corresponding to either the overall air flow rate (to obtain gross concentrations entering the NTP reactor) or the 1 LPM air sampling rate through the impingers (for concentrations in air sampled through the impingers).

When the volumetric air flow rate was maintained at 170 LPM and the reactor was off, a ~2.5 log decrease in infective particles from the humidifier outlet to the upstream impinger and a ~0.35 log decrease in infective MS2 particles between the upstream and downstream impingers were observed (Figure 5.3). Likewise, the qPCR results, which reflect the total number of viruses, suggested a decrease of ~1 log between the humidifier outlet and upstream impinger and ~0.35 log decrease between the upstream and downstream impingers (Figure 5.3). The ~2.6 log decrease in infective particles from the humidifier outlet to the upstream impinger has been fully discussed in Section 4.1.4, and the ~1 log decrease in gene copy concentrations from the humidifier outlet (position 8) to the upstream impinger (position 10) may have several causes, including wall losses along the four meter long duct. Based on the qPCR results, the decrease of infectious viruses through the packed bed when the reactor was off was not due to inactivation of viruses in the aerosols, and was likely due to physical filtration of the virus by the packed bed. When the reactor was turned on with 30 kV power supply, samples collected post-NTP treatment contained infective virus concentrations below our plaque assay limit of quantification. Consequently, the reactor caused a decrease of more than 2.3 log infective MS2 (Figure 5.3). In

contrast, the nearly constant reduction in gene copy concentrations with and without power to the reactor suggests that the virus was inactivated, and not removed physically (Figure 5.3). In Xia et al (Xia et al., 2018) we discuss the likely mechanisms responsible for the nearly three log reduction in MS2 PFU concentration between the introduction of the aerosol at position 8 to the upstream impinger at position 10 (see Figure 2.3).

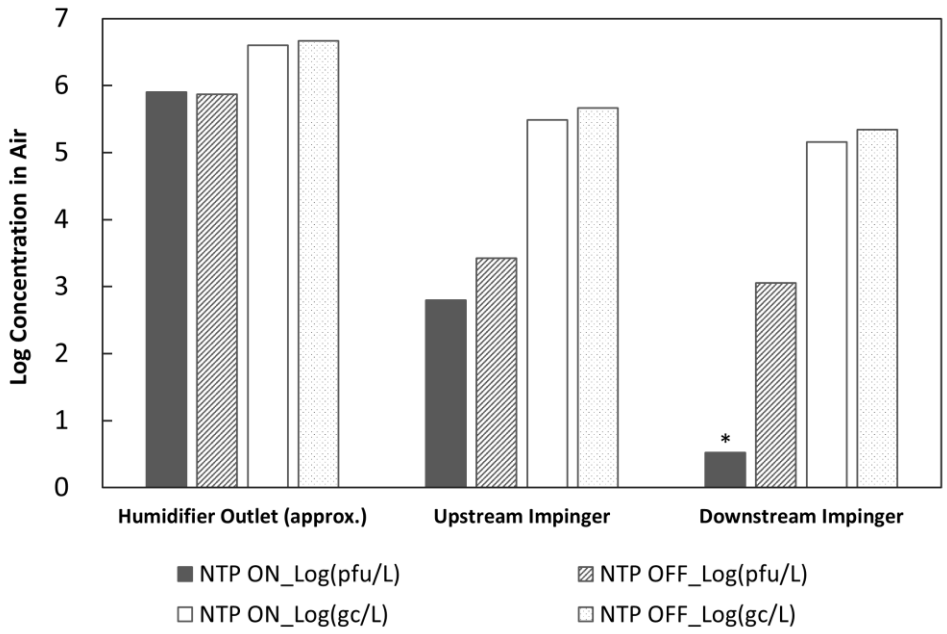

Figure 5. 3 Concentrations of viruses in air measured with plaque assays and RT-qPCR in the NTP reactor powered by 30kV AC supply at a 170 LPM air flow rate (*: Detection limit).

MS2 inactivation was measured over a range of lower voltages (12, 16, and 20 kV) and two air flow rates (170 LPM and 330 LPM). Increasing voltage resulted in an exponential increase in MS2 inactivation by the reactor (Figure 5.4), with the packed-bed filtration effect subtracted. At an air flow rate of 170 LPM and 12 kV, an infective virus reduction of 0.23 log was examined. This increased to a 0.78 log reduction at 20 kV. Inactivation of infectious agents by chemical

oxidants generally is considered to follow a Chick-Watson model, as illustrated by the equation below (Chick, 1908; Watson, 1908):

$$ln\left(\frac{C_D}{C_U}\right) = -kC_{inact}^{n}\mathrm{t} \quad (5.1)$$

where C_D and C_U are downstream and upstream infectious virus concentrations respectively, C_{inact} is the concentration of the inactivating agent generated by NTP, n is the coefficient of dilution (usually assumed to be 1), t is duration of treatment, and k is a kinetic constant. When the NTP reactor is operating at steady state under constant applied voltage, C_{inact} and treatment time t should remain constant. Increasing applied voltage to the NTP reactor increases the concentration of reactive ions and electrons (C_{inact}) in the plasma, and according to Figure 5.4 and Eq. 5.1, C_{inact} should increase exponentially with increasing applied voltage. This assertion, however, needs to be justified in future plasma species measurements and analysis. Increasing the flow rate to 330 LPM, and consequently reducing the treatment time by about half, had a minimal impact on inactivation (Figure 5.4), which indicates that the amount of air treated by the reactor can be increased without reducing much inactivation efficiency. Wu et al. (Y. Wu et al., 2015) reported similar limited impact of treatment time on NTP inactivation efficiency, which showed that doubling the treatment time would only cause 2-4% further inactivation of aerosolized MS2. Extrapolating the results obtained at 12-20 kV and 170 LPM to 30 kV would yield an estimated 3.5 log reduction, in agreement with the greater than 2.3 log reduction obtained with the fixed 30 kV power supply. In this study at the flow rate of 170 LPM, the virus exposure time to NTP species was about 0.25s, and the steady state ozone concentration downstream of the reactor was measured as 0.21 ppm at 20 kV and 2.08 ppm at 30 kV. The ozone dose received by aerosolized MS2 was thereby estimated as 0.0017 min-mg/m^3 at 20 kV and 0.017 min-mg/m^3 at 30 kV (assuming room temperature and pressure). According to Tseng

and Li (Tseng & Li, 2006), 90% (1-log) inactivation of airborne MS2 required an ozone dose of 1.28 min-mg/m^3, which is 75-750 times of the ozone dose provided in this study. So it is likely that ozone acted only as a secondary inactivating reagent in this study and aerosolized MS2 was more predominantly inactivated by radicals and other reactive oxygen species (ROS) generated by the packed-bed NTP reactor over the short exposure time.

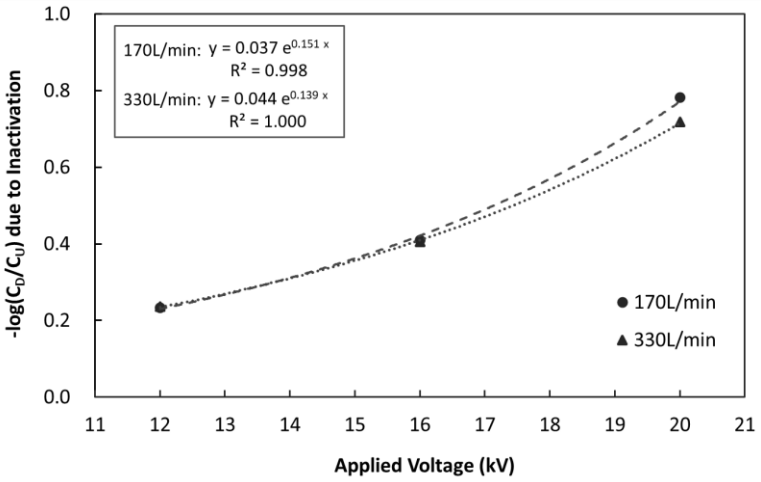

Figure 5. 4 Log-reduction of infectious MS2 in airstream due to inactivation of the packed-bed NTP reactor activated by the variable voltage amplifier at 12kV, 16kV and 20kV (C_D and C_U represent the downstream and upstream concentrations in air, respectively).

The results presented in Figure 5.3 and Figure 5.4 are comparable with the previous studies presented by Vaze et al. and Wu et al.. Vaze et al. applied 28 kV 600 μs pulse discharges to generate NTP, and the reactor achieved 97% inactivation of *E. Coli* (1.5 log reduction) during the 10 s treatment time (Nachiket D Vaze et al., 2007). When the plasma generation area was reduced by 25%, the reactor's *E. Coli* inactivation efficiency reduced significantly to 29% (0.16 log reduction) (Vaze et al., 2010). Wu et al. applied a 14 kV 10 kHz AC power supply, and at 20

W power level, the reactor achieved ~80% MS2 inactivation (0.9 log reduction) in room air during 0.12 s treatment time (Y. Wu et al., 2015). Both studies, however, only reported the reductions of viable bioaerosol concentration after the NTP treatment, and did not separately examine the effect of bioaerosol inactivation by active plasma species, and the physical electrostatic precipitation or filtering effect of the reactor on charged aerosols.

5.1.4 Ozone Generation by the NTP Reactor

One major concern for NTP-based airstream disinfection is the production of ozone in ventilation air, which can have detrimental impacts of human and animal health (Lippmann, 1989). In California, state environmental regulations (Jakober & Phillips, 2008) require that indoor air cleaning devices intended for use in occupied spaces should not produce ozone concentrations greater than 0.05 ppm in treated air streams. We therefore adapted consumer-grade activated carbon honeycomb filters, normally installed over exhaust vents of photocopiers and laser printers, for use as a post-NTP treatment ozone filter.

The ozone concentration, in the air flow upstream of the ozone filter (and downstream of the packed bed section of the reactor), as a function of peak-to-peak voltage (V_{pp}) applied by the Trek high voltage power supply were measured during this study (Figure 5.5). The baseline ozone concentration in the room air was 0.03 ppm. From Figure 5.5 it is apparent that plasma was not established in the reactor and no ozone was produced until the applied V_{pp} exceeded 10 kV. Above 10 kV, the ozone concentration downstream of the packed bed and upstream of the ozone filter increase with increasing V_{pp} and decrease due to dilution with increasing air flow rate, as set by the ID fan. When 20kV AC voltage was applied to the packed-bed NTP reactor,

the maximum transferred current was 0.5mA, and at 170 LPM flow rate, the highest ozone concentration downstream of the reactor was 0.21 ppm, which was small compared with other NTP experiments. Yehia and Mizuno examined (Yehia & Mizuno, 2013) the ozone generation by negative DC corona discharges in a wire-cylinder electrode configuration, and reported ~50 ppm ozone concentration in 4 LPM air flow with 3kV and 0.5mA delivered to the reactor. By assuming constant ozone generation rate, this reported concentration can be recalculated to 1.2 ppm in a 170 LPM air flow, about five times higher than the 0.21 ppm ozone concentration measured with our setup under similar conditions. The relatively low ozone generation further supports the assertion that at 20 kV and 1.7W, with a packed bed configuration of this size, only a small amount of energy was deposited into the system and the reactor was not active enough to achieve high virus inactivation.

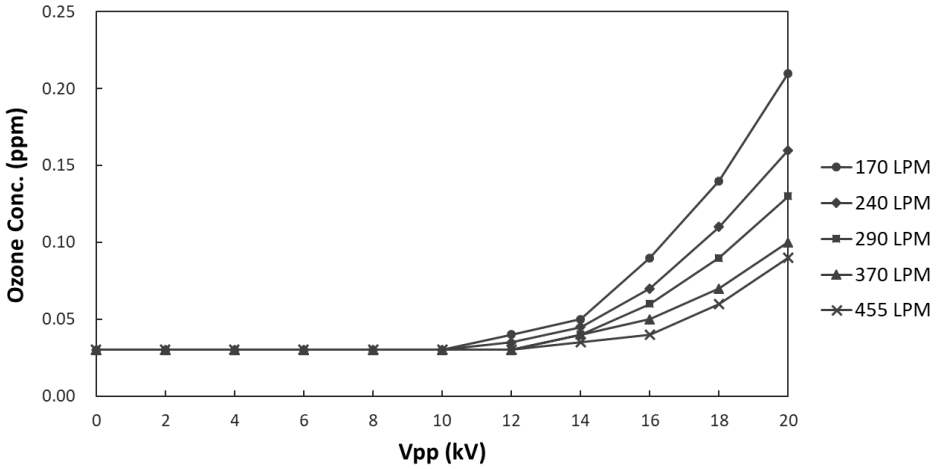

Figure 5. 5 Measured ozone concentrations upstream of the ozone filter as a function of V_{pp} and air flow rate.

Ozone concentrations were measured upstream and downstream of a single, centimeter-thick ozone filter under reactor-on conditions at 20 kV (supplied power ~1.7 W) and 30 kV (supplied

power of 21 W) over a range of air flow rates (Figure 5.6). Increasing air flow rates corresponded with decreasing upstream ozone concentrations due to dilution and increasing downstream ozone concentrations likely due to increasing space velocity (defined as volumetric flow rate normalized by filter volume). The much higher supplied power (21 W) of the 30 kV power supply as compared to the 20 kV power supply (< 1.7 W) also produced more ozone, 10 times higher at all three flow rate conditions as shown in Figure 5.6. This was likely a result of greater O and OH radical production at the higher power, reacting with the available O_2 to form more O_3. At 170 LPM and 30 kV, the single layer of activated carbon filter reduced upstream ozone concentrations by 96%, however the downstream O_3 concentration (0.09 ppm) still exceeded the 0.05 ppm California standard. The addition of a second filter would very likely reduce concentrations below the California standard, with little increase in the minimal pressure drop across the filter (20 Pa at the flow rate of 170 LPM).

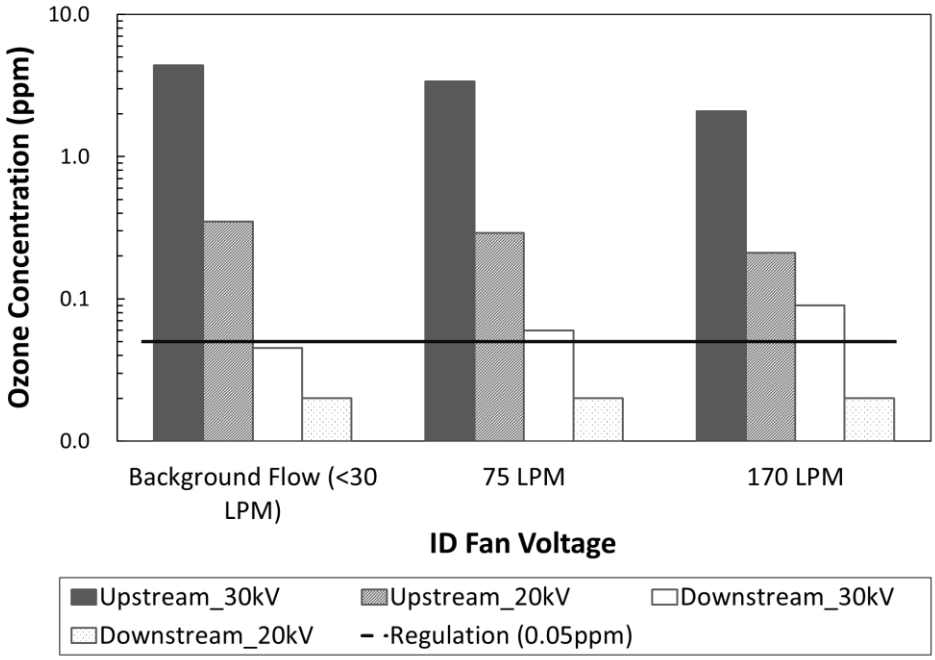

Figure 5. 6 Measured ozone concentration upstream and downstream of the single layer ozone filter with either 20 kV or 30 kV power supply at varied air flow rates. Dashed line represents ozone standard for indoor air cleaners set by the state of California (Jakober & Phillips, 2008).

5.1.5 Conclusion and Future Work

For the purpose of developing a novel airstream disinfection technology and contributing to the scientific understanding of spontaneous inactivation of airborne pathogens in a plasma environment, a packed-bed dielectric barrier discharge non-thermal plasma reactor was designed and constructed in this study and its airstream disinfection efficiency was examined. The plaque assays results showed that the reactor with 30kV power supply can achieve an at least 2.3 log reduction in MS2 pfu concentration. The qPCR results indicated a ~0.35 log reduction in MS2 genome copies across the reactor by packed bed filtration. Using genome copies as a standard, the plaque assay results indicated over 99% inactivation of MS2 by non-thermal plasma only, which proved that the non-thermal plasma generated in the study can inactivate viruses effectively. With the Trek variable high voltage power supply (0-20 kV), the infectious MS2 log reduction due to NTP inactivation solely increased exponentially as the increase of applied voltage, with the minimum 0.23 log reduction at 12kV applied voltage, and the maximum 0.78 log reduction at 20kV applied voltage, at 170 LPM flow rate. Doubling the flow rate should not have large impact on the reactor inactivation. The pressure drop across the packed bed and ozone filter was measured to be minimal and the total power consumption of the NTP reactor was 1.7 W with the 20kV Trek high voltage supply and 21W with the fixed 30kV power supply. Ozone was generated by the active plasma but the concentration can be effectively reduced to meet the regulation by commercial ozone filters without significant pressure drop. In future, the packed-

bed depth, the dielectric material and the air flow rate through the sampling train can be varied to further examine the performance of the reactor under different design and flow conditions.

5.2 In-flight Inactivation of PRRSv by Non-thermal Plasma

5.2.1 Short review on the research background and methodology

Porcine Reproductive and Respiratory Syndrome (PRRS) is one of the greatest threats to modern pork industry. The virus has been detected in air more than 9 km downwind of infected swine (Dee et al., 2009; Otake et al., 2010). Applying HEPA filtration, the traditional bioaerosol control technology, to ventilation air supplied to hog barns involves structural retrofits to buildings that can be costly, in addition to the periodic replacement of used filters. Non-thermal plasmas (NTPs) are electrical discharges comprised of reactive radicals and excited species that inactivate viruses and bacteria while inducing minimal pressure drop and thus avoiding the need for building retrofits. The study discussed in the previous section demonstrated effective inactivation of bacteriophage MS2 as a function of applied voltage and power by a prototype packed bed non-thermal plasma reactor. The objective of the present study is to measure the inactivation efficiency of aerosolized PRRSv by the same packed bed NTP reactor and compare it with the measured NTP inactivation efficiency of MS2 under similar conditions. The resulting comparison will indicate to what degree MS2 can be considered a conservative surrogate for PRRSv in future optimization of NTP reactor design. A PRRSv solution containing ~10^5 $TCID_{50}$/ml was aerosolized at a rate of 3 ml/min by an air-jet nebulizer and introduced into air flows of 5 or 12 cfm followed by NTP exposure in the reactor. Two impingers sampled the virus-laden air flow at both upstream and downstream positions of the reactor. Subsequent $TCID_{50}$ assay and quantitative polymerase chain reaction (qPCR) analyses of the collected

samples determined the pre- and post-treatment abundance of infective PRRSv (in $TCID_{50}$/ml) as compared with the abundance of the viral genome (qPCR), whether infective or rendered inactive by NTP exposure. An optical particle sizer measured upstream and downstream aerosol size distributions, giving estimates of aerosol filtration by the reactor. The background of this study is discussed in detail in Section 1.3.1 and Section 1.3.3, and the research methodology is discussed in detail in Section 2.3.2.

5.2.2 Droplet Size Distribution

For all reactor-activated tests, particle size distributions (PSD) were measured both upstream and downstream of the packed-bed NTP reactor under two flow rates, and the results were averaged for each phase and each flow rate (Figure 5.7). From Figure 5.7 it is evident that the OPC measurements were quite consistent with small confident intervals, indicating that the virus solution aerosolization process was repeatable and the packed-bed had relatively consistent filtration efficiencies regardless of the applied voltage level (which is proved by PSD data comparison between different applied voltages in the same phase with the same flow rate). The PSD plots proved that aerosols generated by air-jet nebulizers are polydisperse in size with large proportion of droplets over 5 μm in diameter, which agrees with other reports on aerosol PSDs through air-blast atomization (Lorenzetto & Lefebvre, 1977; Steckel & Eskandar, 2003). The upstream sampling probe was installed about 40” downstream of the air-jet nebulizer, which was only about a quarter of the distance between the ultrasonic atomizer and upstream sampling port (144”) in our previous bacteriophage MS2 inactivation setup. The shorter distance led to more incomplete aerosol evaporation, and as a result more coarse droplets (with d_p ranging from 2.5 to 10 μm) would reach the reactor, get filtered by the packed bed and cause bulk liquid

accumulation in the reactor. This inference was proved by experimental observations: during all PRRSv inactivation tests in both phases, bulk virus solution was found accumulating between the glass beads in the packed-bed NTP reactor, while for all MS2 tests conducted in University of Michigan, no liquid accumulation was found with the ultrasonic atomizer (potentially generates aerosols with smaller and more uniform size distribution(Steckel & Eskandar, 2003)) and dry compressed air (RH typically <10%) supplementing the ambient inlet air supply. It should be noted throughout the data analysis and interpretation here that the accumulated virus solution is not desired for this study, since it may cause reemission of aerosols from the packed bed, change the NTP discharge phenomena, serve as a protective reservoir for suspended viruses, and impact reactive species formation by the reactor.

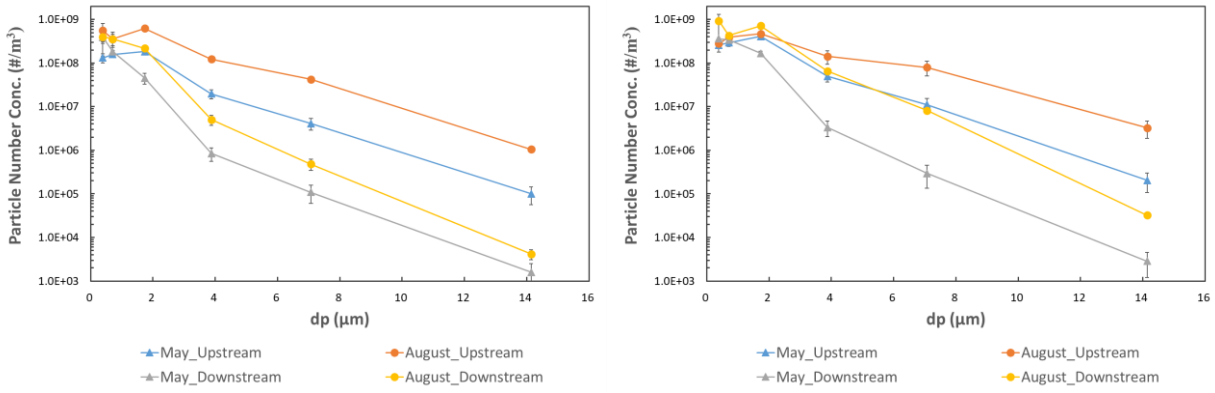

(a) (b)

Figure 5. 7 Average droplet size distributions both upstream and downstream of the reactor in each phase (May and August) under wind tunnel flow rate of (a) 12 cfm and (b) 5 cfm.

The two plots in Figure 5.7 illustrate how virus solution aerosolization and packed-bed filtration would change with changing flow rate and flow relative humidity. For data obtained in a specified phase of testing (May or August), the upstream droplet number concentration is generally higher at 5 cfm (Figure 5.7b) than that at 12 cfm flow rate (Figure 5.7a), due to

reduced dilution and slower droplet evaporation at lower flow rate. The average RH of the ambient room air (which was the major air source of the wind tunnel flow) in August was 49%, much higher than the ambient condition in May (38%), while the air temperature remained relatively constant in both testing phases (22.2 ℃ in May and 23.2 ℃ in August). Higher inlet air RH in August caused slower droplet evaporation, and as a result more droplets in all sizes were found upstream of the reactor in August in both Figure 5.7a and 5.7b. Comparison between upstream and downstream PSD in both plots gives an estimation of the packed bed filtration effects on various size droplets. Figure 5.7a showed that the number concentrations of droplets larger than 1 μm reduced significantly from upstream to downstream of the reactor, which should be mainly due to filtration by the packed bed and size reduction through evaporation, and larger droplets had more significant number reductions due to their low mobility and rapid evaporation. Concentrations of submicron droplets (droplets smaller than 1 μm), however, increased from upstream to downstream of the reactor, potentially due to re-aerosolization of virus solutions accumulated in the packed bed, and evaporation of super micron droplets to submicron sizes. Figure 5.7b showed similar droplet number concentration trends at 5 cfm, while concentrations of droplets between 1 μm and 7 μm, especially in August, showed less reduction compared with the 12 cfm data. This should be due to slower evaporation of droplets larger than 7 μm to this size range at 5 cfm. At 12 cfm, these droplets may evaporate faster and fall into the submicron region before reaching the downstream sampling probe. These observations and hypothesis are proved by comparing droplet penetration (downstream concentration divided by upstream concentration) in May and August at two flow rates (Figure 5.8). From Figure 5.8, it is evident that in May droplets had similar penetration through the reactor at both flow rates, and 1 μm to 5 μm droplets had slightly higher penetration at 5 cfm. In August at 12 cfm, the penetration of

droplets smaller than 4 μm had similar values as the May data, while droplets larger than 4 μm had less penetration, likely due to the increased amount of virus solution accumulated in the packed bed at higher RH. At 5 cfm in August, the penetration curve was quite different from the other three, with significantly higher droplet penetration in the range 2 μm - 7 μm. It is likely that at this air-to-water mass flow ratio, the RH in the wind tunnel exceeded the critical RH predicted by our previous droplet evaporation numerical model (Xia et al., 2018), which prevented rapid liquid evaporation and led to more 2 μm - 7 μm droplets reaching the downstream sampling probe. Based on the OPC data and assuming spherical droplets, the average volumetric droplet penetration through the packed-bed was 10.6% in May at 12 cfm, 13.7% in May at 5cfm, 6.2% in August at 12 cfm, and 22.2% in August at 5 cfm.

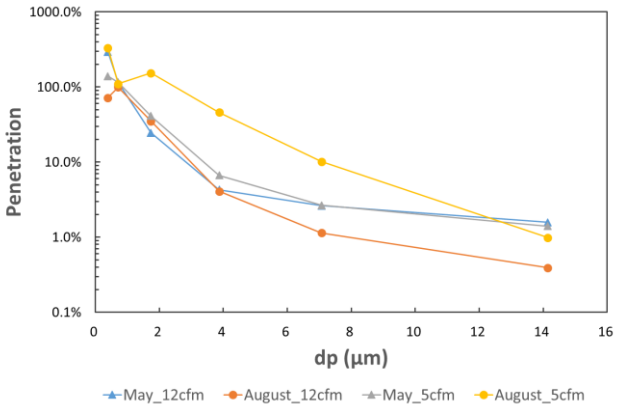

Figure 5. 8 Penetration of particles (downstream number concentration / upstream number concentration) in each OPC size bin measured at two flow rates in the two testing phases (May and August).

5.2.3 PRRSv Inactivation by NTP

In this study, $TCID_{50}$ analysis of the twin impinger samples collected in each test provided estimations of viable PRRSv reduction from upstream to downstream of the reactor, and either

qPCR analysis (performed for each sample that underwent $TCID_{50}$ analysis) or reactor-off tests can provide estimations of viable PRRSv reduction across the reactor that is not caused by NTP discharge (referred to as filtration effect by the packed bed). $TCID_{50}$ analysis results, subtracting viable PRRSv reductions due to packed bed filtration, yielded the inactivation of PRRSv by the reactor solely due to NTP discharge. Table 5.1 summarizes PRRSv inactivation efficiency results determined based on the ratio of post-treatment (downstream) to pre-treatment (upstream) abundance of viable PRRSv normalized by either the ratio of downstream to upstream abundance of infective PRRSv without NTP treatment (reactor-off), or ratio of downstream to upstream abundance of genome copies determined by qPCR. Highlighted values represent rejected, unphysical results implying higher infectivity for post-treatment samples. For several tests, particularly those conducted in May, $TCID_{50}$ or qPCR analyses did not pass the data quality controls. Specifically, in some cases either the abundance of infective PRRSv or the number of genome copies was found to be higher at the downstream location than at the upstream location, including a few instances of this occurring when the reactor was not powered. Degradation of the airborne PRRSv by attack from reactive species within the non-thermal plasma would not be expected to result in either an increase in $TCID_{50}$ or an increase in the number of PRRSv genome copies at the downstream sampling location. More consistent values of inactivation efficiency were obtained in phase 2 of testing (August), as is evident from the absence of negative values of inactivation efficiency (Table 5.1). The unreasonable increasing $TCID_{50}$ or PRRSv genome copies data could be due to sampling or analysis errors, and accumulation of virus solution in the packed bed and the resulting potential re-aerosolization of PRRSv in the downstream flow can also induce a large uncertainty in the acquired inactivation data. From Table 5.1, it can be found that using either qPCR results or reactor-off test results as

the indication of background viable PRRSv reduction by packed bed filtration generally yielded similar NTP inactivation efficiency results. In the following analysis qPCR data were used rather than reactor-off test results, mainly because qPCR and $TCID_{50}$ analysis were conducted on the same sample collected by each impinger in each test, which should provide the most comparable results with the fewest differences in test conditions at which each sample was taken. The reactor-off tests were conducted separately, which could have been subject to different RH conditions, varied virus solution aerosolization and evaporation phenomena, and have different viable PRRSv concentration in the initial solution filled into the syringe pump. In addition, the previous bacteriophage MS2 inactivation study used qPCR data as the indication of packed bed filtration, so the same analytical method should be applied in order to compare results between the two studies.

Table 5. 1 Summary of PRRSv inactivation efficiency results, normalized by either reactor-off tests or qPCR analysis, at two air flow rates and four NTP voltage settings.

	August Tests		**May Tests**		
	30kV	**20kV**	**12kV**	**20kV**	**16kV**
Reactor-Off 5cfm	66.20%	29.71%	71.27%	-27.10%	68.16%
qPCR 5cfm	61.01%	53.47%	83.88%	-51.02%	80.03%
Reactor-Off 12cfm	73.98%	26.55%	-71.79%	94.63%	35.24%
qPCR 12cfm	71.31%	47.23%	71.59%	98.63%	71.15%

The inactivation efficiency reported in Table 5.1 (normalized by qPCR analysis) were plotted with the results showing bacteriophage MS2 inactivation by the same packed bed NTP reactor (Figure 5.9). For data acquired in phase 1 testing (May), the figure illustrates the increasing trend

in inactivation efficiency with increasing applied voltage, as expected, and the generally lower inactivation efficiency at the higher air flow rate (12 cfm) as compared to the lower air flow rate (5 cfm). These trends are as expected and agree with those observed in previous results involving inactivation of bacteriophage MS2 conducted at University of Michigan. The PRRSv inactivation levels by NTP agree with the relevant NTP inactivation levels reported by other research groups (Vaze et al., 2010; Y. Wu et al., 2015). Evident from the May data presented in Figure 5.9 is the fact that under similar experimental conditions, the effectiveness of the NTP in inactivating PRRSv aerosols was somewhat higher than the demonstrated effectiveness for inactivating MS2 with the same device at the same conditions; however, the large uncertainty in the results as indicated by the large confidence intervals allows only for a conclusion that the two viruses were likely inactivated comparably. Data acquired in phase 2 testing (August), however, showed reduced inactivation efficiency. With 20 kV supplied voltage, the measured inactivation efficiency at both flow rates in August was 30%-50% lower than the values acquired in May or in the MS2 inactivation study. When the supplied voltage was increased from 20 kV to 30 kV, and the power consumption was increased from 1.7 W achieved at 20 kV to about 23 W achieved at 30 kV, the packed bed NTP reactor showed increased PRRSv inactivation efficiencies at both flow rates, which were still lower than the values acquired with 20 kV power supply in May or during the MS2 inactivation study. It was found in our previous study that the bacteriophage MS2 inactivation by the packed bed NTP reactor with 30 kV power supply can lead to at least 2-log (99%) viable MS2 reduction, which was significantly higher than the 30 kV results presented in Figure 5.9. It is likely that the reduced NTP inactivation efficiency observed in August, as well as the large confidence intervals for all PRRSv inactivation results in both

phases, were due to increased accumulation of bulk virus solution (in this study DMEM) in the packed bed.

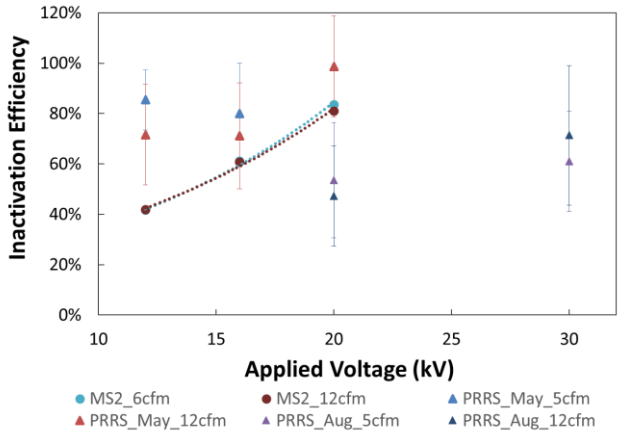

Figure 5. 9 Comparison of phase 1 (May) and phase 2 (August) PRRSv inactivation by NTP treatment at two air flow rates (5cfm and 12 cfm) and four voltages (12, 16, 20, and 30 kV), as compared to earlier results for MS2 phage inactivation at the similar conditions (30 kV not shown).

As discussed in previous sections, incomplete evaporation of the PRRSv-laden droplets of DMEM was consistent throughout both phase 1 and phase 2 tests, while prior tests involving MS2 inactivation achieved complete or near complete droplet evaporation after several modifications to the experimental apparatus: lengthening the distance between the introduction of the droplets into the airstream and the NTP reactor; supplementing ambient air with dry compressed air (RH<10%), and thereby lowering relative humidity and speeding evaporation; and producing smaller droplets via an ultrasonic atomizer. These remedies were not available or not possible for the tests involving PRRSv. As a result, the significant unanswered question regarding the present results is the impacts, if any, of the persistent presence of liquid DMEM in fine droplets exposed to the non-thermal plasma and accumulating in the NTP reactor itself.

DMEM is a solution of glucose in water. One hypothesis is that residual DMEM on aerosols or as aerosols passing through the NTP reactor may have the effect of protecting PRRSv from oxidation by the reactive species generated by the plasma. Whereas H_2O alone, when dissociated, produces additional reactive species in the form of H^+ and OH^-, hydrocarbons would act more as a sink for the plasma-generated species, consuming them in the course of their complete oxidation. There exists a separate branch of plasma environmental remediation that involves using plasmas to oxidize chemical contaminants in water supplies or wastewater. Support for this hypothesis came from preliminary tests prior to phase 1. Prior testing at Univ. of Michigan using MS2 phage determined that ozone (O_3) produced by the NTP reactor had the potential to accumulate in the downstream impinger fluid, a virus dilution buffer (VDB) consisting small amounts of sodium and phosphorous salts dissolved in water. The dissolved ozone was found to continuously inactivate MS2 phage in the impinger during and after testing, potentially leading to a high bias in inactivation efficiency results. Sodium sulfite was routinely added to the VDB during MS2 testing, serving to consume O_3 and prevent inactivation of MS2 phage while in the impinger. However, when similar tests were conducted exposing PRRSv in DMEM to dissolved O_3, the results showed no inactivation of PRRSv in DMEM by O_3, suggesting that O_3 was consumed by oxidation reactions with the hydrocarbons in DMEM and therefore unavailable to chemically attack the PRRSv in solution. A second potential effect of residual DMEM could be in influencing the electrical properties of the packed bed and the strength or distribution of the plasma therein. In the packed bed, the plasma exists in the voids between the beads where the electric field increases above the threshold where electrical breakdown occurs in air. Accumulation of DMEM (approximate conductivity $\sigma = 1.4$ S/m (M.-T. Chen, Jiang, Vernier, Wu, & Gundersen, 2009)) in these spaces could provide a conductive

electrical pathway that prevents such electric fields from forming. This, too, would be expected to reduce the apparent inactivation efficiency of tests involving DMEM as compared to tests in which evaporation of the liquid phase was more complete.

In order to test these hypotheses and the potential effects of accumulated DMEM, tests were conducted after phase 2 in which the packed-bed NTP reactor was pre-soaked with known amounts of DMEM (5 mL or 10 mL), and the inactivation of MS2 aerosols by the "wet" reactor was measured. Figure 5.10 shows the results of these tests in the form of MS2 reduction, comprising both physical filtration and NTP inactivation (with 20 kV), comparing samples collected at the upstream pre-treatment location against those collected at the downstream post-treatment location. The values of viable MS2 reduction induced by the 20 kV dry reactor were acquired from the previous bacteriophage MS2 inactivation study (Figure 5.4). With 5 mL DMEM sprayed into the packed bed, the viable MS2 reduction decreased from 88% (dry reactor) to 79%, and with 10 mL DMEM added, the viable MS2 reduction was further reduced to 46%. The figure proved that increasingly accumulated DMEM in the packed bed would reduce viable MS2 reduction from upstream to downstream locations of the packed bed NTP reactor, potentially by quenching reactive plasma species or preventing electric field build up for NTP discharge. With regard to the electrical effects, it seemed that the residual DMEM in the packed-bed NTP reactor can increase the amplitude of transferred current without changing the amplitude and waveform of the applied voltage. With 20 kV applied to the dry packed-bed NTP reactor, the transferred current had an amplitude of 0.40mA. The addition of 5 ml of MEM to the packed bed increased the current amplitude to 0.48mA, and the addition of 10 ml of MEM to the packed bed further increased the current amplitude to 0.56mA. This was reasonable since the

accumulation of liquid in the packed bed could reduce the resistance of the reactor and thus increasing the amplitude of transferred current. This discharge environment, however, may not be favorable for plasma generation, since more current would pass through the conductive liquid without ionizing air in the packed-bed.

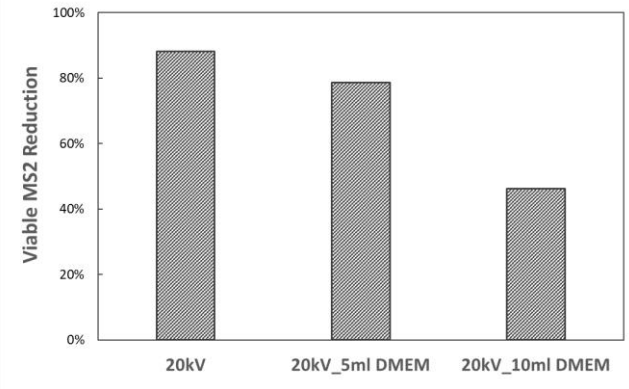

Figure 5. 10 Reduction (filtration + inactivation) of viable bacteriophage MS2 in response to 5 ml and 20 ml of DMEM added to and held within the NTP packed bed.

5.2.4 Conclusion and Future Work

In summary, this study provides the first demonstration of NTP inactivation of an airborne pathogen relevant to livestock. Compared to non-enveloped bacteriophage MS2, no evidence show that the lipid layer of enveloped PRRSv offered any protection against inactivation, and the two viruses were likely inactivated comparably. The highest PRRSv inactivation efficiency was 98.6% achieved in phase 1 (May) with 20 kV voltage supplied to the packed bed NTP reactor at the wind tunnel flow rate of 12 cfm. However, size, composition of DMEM droplets and relative humidity were all likely contributors to variability in measured inactivation. Future study with improved virus aerosolization methods and have more consistent and dryer inlet air supply should be conducted to further examine how non-enveloped and enveloped viruses react to NTP

inactivating environment. Overall, the results show promising results to inactive airborne PRRSv and offer potential alternatives to producers to enhance their biosecurity practices.

CHAPTER VI CONCLUSIONS AND FUTURE WORK

6.1 Conclusions

This thesis focuses on two major research projects related to aerosol control and corona discharge and contains three topics. The first research project (one topic) is focused on powdered activated carbon (PAC) injection into the flue gas to remove mercury from the exhaust of coal-fired power plants (CFPPs) and its potential impact to climate change due to low removal efficiency of PAC in ESPs. The second research project (two topics: virus aerosolization and NTP inactivation) is focused on packed-bed non-thermal plasma (NTP) and the experimental examination of in-flight inactivation of two airborne viruses, MS2 and PRRSv, by NTP. The major objectives of this thesis are: a) to provide the first comparative measurements of optical scattering and absorption coefficients of aerosols comprised of varying mixtures of FA and PAC; b) to describe the method and necessary conditions required to successfully use a consumer-grade ultrasonic air humidifier to suspend viral aerosols in flowing airstreams in the service of studying airborne pathogen inactivation; c) to demonstrate effectiveness of simple and economic light attenuation measurements in real-time *in situ* monitoring of virus solution atomization rate from the consumer-grade ultrasonic humidifier; d) to demonstrate effectiveness of a packed-bed dielectric barrier discharge non-thermal plasma in-flight disinfection system on inactivating aerosolized non-enveloped virus MS2, and enveloped virus PRRSv. Major conclusions are listed as bullet statements below.

6.1.1 Optical and Physical Characterization of Mixed Coal Fly Ash and Particulate Carbon

1) For the relatively large PAC and FA particles sampled in the experiment, the SEM images indicate agglomeration in the flue gas is unlikely and PAC and FA would likely be emitted from CFPPs with ACI installed as separate particle species.

2) Both MSC and MAC of FA-PAC admixture aerosols would increase linearly with the increase of particles' carbon content, while the increase of carbonaceous particles in the FB emissions had a more significant effects on the MAC of the emissions, and the SSA would decrease linearly with the carbon content increase.

3) The acquired MAC value of soot is relatively low compared with other reported values, which may be due to the small size of the oil lamp flame, and the acquired SSA values for both soot and FA are comparable with other relevant reports.

4) It is reasonable to conclude that the installation of ACI in CFPPs would increase the MAC of the emissions from the power plants and make the CFPPs potentially a new source of light absorbing particle emissions. Although large in average size, the emitted PAC particles, especially the submicron fraction, can absorb light efficiently and potentially act like BC in the atmosphere.

6.1.2 Suspending Viral Aerosols in an Airstream through Ultrasonic Atomization

1) The experimental results proved that the commercial-grade ultrasonic air humidifier used in this study can consistently suspend 10^2-10^3 pfu/L dry MS2 aerosols into the 170 LPM air flow at its low power setting (H2).

2) During atomization, the ventilation of ambient air into the humidifier reservoir can cause temperature rise of the virus solution inside, but MS2 would not be largely inactivated as long as the temperature remained below about 20℃. The vibration of piezoelectric transducer inside the humidifier reservoir would not cause significant solution temperature rise and should have minimal effects on the survivability of virus inside the humidifier reservoir.

3) An average of 2.6-log reduction in infectious MS2 concentration in air were estimated, mainly due to the evaporation process of atomized MS2-VDB droplets. This inactivation is unavoidable with current setup, and in order to achieve desired concentration of viable bioaerosols in the downstream air flow, the initial virus or bacteria concentration in the bulk dilution buffer solution, the ultrasonic aerosolization rate and the air flow rate through the sampling train should be adjusted accordingly.

4) Light attenuation measurements and Arduino platform were reliable for continuous or repeated atomization rate monitoring. The real-time *in situ* atomization rate monitoring system developed in this thesis was fast and accurate to monitor real-time light attenuation, and was able to indicate change of ultrasonic atomization scenarios due to changes of bulk liquid properties. The system was effective in indicating real-time ultrasonic atomization

rate within the range of 0.7 ml/min to 3 ml/min, and the Beer–Lambert law and Equation 3 was proved to be valid for the current setup without additional corrections.

5) Exposure to laser applied in this study (a 632.8 nm Class 3B laser with rated power of 0.8 mW and maximum power of 5 mW) would not cause unintentional MS2 airstream inactivation.

6.1.3 Inactivation of Airborne Viruses by A Packed Bed Non-Thermal Plasma Reactor

1) The packed-bed dielectric barrier discharge NTP reactor constructed as a part of this thesis research can achieve inactivation of airborne MS2 suspended in a controlled flow. The inactivation of aerosolized MS2 phage was found to increase exponentially with increasing applied voltage from 12 kV to 20kV at 170 standard liters per minute (LPM). At 30 kV and an air flow rate of 170 LPM, a greater than 2.3-log reduction of infective virus was achieved across the reactor. This reduction represented ~2 log of the MS2 inactivated and ~0.35 log physically removed in the packed bed.

2) Increasing the air flow rate from 170 to 330 LPM did not significantly impact virus inactivation effectiveness, which agreed with the test results reported by Wu et al. (Y. Wu et al., 2015).

3) Ozone was generated by the packed-bed NTP reactor, and ozone concentration downstream of the reactor can reach 2 ppm with 30 kV power supply at 170 LPM flow rate. Activated carbon-based ozone filters can remove at least 95% of residual ozone, in most cases bringing

the ozone emission from the system down to below the California regulation for indoor air cleaning devices (Jakober & Phillips, 2008).

4) The pressure difference upstream and downstream of the packed-bed NTP reactor measured at the flow rate of 170 LPM was 45 Pa, reasonably low due to the porosity of the packed bed. The ozone filter was also quite porous, with a honeycomb structure that produced a pressure drop of 20 Pa at the flow rate of 170 LPM.

5) Compared to non-enveloped bacteriophage MS2, no evidence show that the lipid layer of enveloped PRRSv offered any protection against inactivation, and the two viruses were likely inactivated comparably. The highest PRRSv inactivation efficiency was 98.6% achieved in phase 1 (May) with 20 kV voltage supplied to the packed bed NTP reactor at the wind tunnel flow rate of 12 cfm.

6) In the study on PRRSv inactivation by NTP treatment, size, composition of aerosolized DMEM droplets and the air flow relative humidity were all likely contributors to variability in measured inactivation. Accumulated DMEM bulk liquid in the packed bed can reduce the reactor's efficiency on viable PRRSv reduction, potentially through quenching reactive plasma species or preventing electric field build up for NTP discharge.

6.2 Future Work

This thesis study proved that the installation of ACI in CFPPs could potentially make the CFPPs potentially a new source of light absorbing particle emissions; the commercial-grade ultrasonic air humidifier can consistently suspend bioaerosols from bulk liquid into a controlled air flow

with the aerosolization rate monitored by laser light attenuation measurements; and the constructed packed-bed dielectric barrier discharge NTP reactor can achieve airstream inactivation of airborne MS2 and PRRS. However, much is unknown for these research topics and much more study is to be conducted, especially on the mechanism and side effects of NTP inactivation, and how to improve ultrasonic atomization efficiencies aerosolizing different virus or bacterial dilution buffers without causing much unintentional inactivation. Future efforts should include, but are not limited to the following.

For the project on optical and physical characterization of mixed coal fly ash and particulate carbon, several limitations have been observed during the research. The measurements conducted for FB emissions only sampled relatively large particles since the smaller particles may have been exhausted during the free elutriation of the FB before any measurements, and the size distributions of the sampled particles were not fully examined. In future a dilution chamber should be built downstream of the FB to capture and dilute the small particles emitted by the FB during the early stage of fluidization for PAX measurements, and scanning mobility particle sizer spectrometer (SMPS) should be utilized to further examine the size distribution of sampled particles. Last but not least, since most CFPPs use industrial opacity sensors to monitor their PM emissions, the light extinction measured by PAX and industrial opacity sensors should be compared to examine the effectiveness of opacity sensors on detecting carbon emissions from CFPPs.

For the research on suspending viral aerosols in an airstream through ultrasonic atomization, methods such as increasing virus or bacteria concentration, or reducing salt concentrations in the

bulk dilution buffer solution, should be examined to minimize the effects of unintentional evaporation-induced inactivation on successfully suspending virus or bacteria into the airstream with desired concentration. In addition, ultra-transparent cap can be installed on the humidifier chimney pinhole to completely prevent potential droplet leakages, and an active water-cooling system should be constructed in the humidifier reservoir to prevent virus or bacteria inactivation before aerosolization due to bulk liquid temperature increase. Lastly, an adjustable piezoelectric transducer, which can be tuned to atomize glucose solution at a higher aerosolization rate, should be installed for successful aerosolization of viruses suspended in MEM or other viscous buffer solutions.

For the project of in-flight inactivation of airborne virus by packed bed non-thermal plasma, it is proposed that the inactivation mechanism of non-enveloped and enveloped virus species by the pack-bed NTP reactor should be examined. Virus has a structure of genes (DNA or RNA) surrounded by a protective coat of protein known as capsid. Some virus species which have a lipid envelope covering the protein capsid are known as enveloped viruses, and the species that do not have the envelope are non-enveloped viruses. It is commonly believed that enveloped viruses are easier to sterilize than non-enveloped viruses. Tang et al. (Joseph Tang, Colacino, Larsen, & Spitzer, 1990) reported that an antidepressant, Hypericin, was virucidal to all tested enveloped viruses, but have no effect on the tested non-enveloped viruses. Vollenbroich et al. (Vollenbroich, Özel, Vater, Kamp, & Pauli, 1997) proved that surfactin, a cyclic lipopeptide antibiotic, can inactivate enveloped viruses much more efficiently than inactivating non-enveloped viruses. Pruss et al. (Pruss et al., 2002), however, reported that the exposure to gamma irradiation has similar inactivation effects on examined enveloped and non-enveloped viruses.

The study presented in this thesis has proved that the constructed packed-bed NTP reactor can inactivate MS2, a non-enveloped virus, and PRRS virus, an enveloped virus, with comparable efficiencies. The results, however, has large uncertainty due to incomplete evaporation of MEM droplets during the PRRS virus inactivation tests. It is proposed that the packed-bed NTP reactor's inactivation of two enveloped viruses, bacteriophage Phi6 and PRRS virus, should be further examined using the same experimental setup under similar temperature and *RH* conditions as the MS2 tests. To further study the mechanism of NTP inactivation, optical emission spectroscopy (OES) can be applied to examine the abundance of reactive oxygen species (ROS) generated by the packed-bed NTP reactor, and SEM and agarose gel electrophoresis can be applied to examine the damage caused by NTP discharge and reactive plasma species to the virus capsid and genes (Y. Wu et al., 2015).

It is also proposed that the removal efficiency of H_2S and/or NH_3 by the packed-bed NTP reactor should be examined. One predicted application of the packed-bed NTP reactor is preventing pathogen and odor emission from the manure pit under agricultural animal confinement. The reactor's inactivation of pathogens, mainly viruses, has been deeply studied, and experiments measuring the reactor's removal efficiency of odorous compounds, H_2S and/or NH_3, are proposed to be conducted subsequently in order to validate this prediction. In addition, the packed-bed depth, the dielectric material, and the air flow rate through the sampling train can be modified to investigate varied NTP inactivation performance at various flow conditions, and a new packed-bed NTP reactor with coaxial electrodes should be constructed to examine the NTP inactivation performance under different electric field distributions and discharge scenarios. For the PRRSv inactivation study, future tests with improved virus aerosolization methods and have

more consistent and dryer inlet air supply should be conducted to further examine how non-enveloped and enveloped viruses react to NTP inactivating environment. Lastly, as shown in Figure 5.3, the MS2 pfu concentration from the downstream impinger with 30kV power supply was too low to be detected by plaque assay analysis. Concentrating process, such as centrifuge, is proposed to be conducted on these samples to exactly determine their infectious MS2 concentrations and report more accurate inactivation performance of the reactor with 30kV high voltage supply.

Appendix

1. Arduino Program for Voltage Measurement and Data Logging from the Photodiode

```
// the setup routine runs once when you press reset:
unsigned long time;
const int numReadings = 5;


float readings[numReadings];    // the readings from the analog input
int readIndex = 0;           // the index of the current reading
float total = 0;             // the running total
float AverageVoltage = 0;     // the average


int inputPin = A0;
void setup() {
 analogReference(INTERNAL);
 // initialize serial communication at 9600 bits per second:
  Serial.begin(9600);
  Serial.println("CLEARDATA");
  Serial.println("LABEL,Computer Time,Time (Sec.),Volt. (V),");
// initialize all the readings to 0:
for (int thisReading = 0; thisReading < numReadings; thisReading++) {
```

```
readings[thisReading] = 0;
}
}

// the loop routine runs over and over again forever:

void loop()  {
// read the input on analog pin 0:
int sensorValue = analogRead(A0);
// Convert the analog reading (which goes from 0 - 1023) to a voltage (0 - 5V):
float voltage = sensorValue * (1.25 / 1023.0);
// print out the value you read:
// subtract the last reading:
total = total - readings[readIndex];
// read from the sensor:
readings[readIndex] = voltage;
// add the reading to the total:
total = total + readings[readIndex];
// advance to the next position in the array:
readIndex = readIndex + 1;

// if we're at the end of the array...
if (readIndex >= numReadings) {
```

```
// ...wrap around to the beginning:
readIndex = 0;
}

// calculate the average:
AverageVoltage = total / numReadings;

  Serial.print("DATA,TIME, ");
  time = millis()/1000;
  //prints time since program started
  Serial.print(time,1);
  Serial.print(", ");
  // wait a second so as not to send massive amounts of data
  Serial.println(AverageVoltage,6);
  // display voltage to six decimal places
   delay(1000);
  // output data after 5 seconds to reduce spam
}
```

Bibliography

Altman, Ralph, Buckley, Wayne, & RAY, DR ISAAC. (2001). Wet Electrostatic Precipitation Demonstrating Promise for Fine Particulate Control-Part II. *Power Engineering, 105*(2), 42-42.

Altman, Ralph, Offen, George, BUCKLEY, PEPRI, BUCKLEY, WAYNE, & RAY, DR ISAAC. (2001). Wet Electrostatic Precipitation Demonstrating Promise for Fine Particulate Control--Part I. *Power Engineering, 105*(1), 37-37.

Amos, Helen M, Jacob, Daniel J, Streets, David G, & Sunderland, Elsie M. (2013). Legacy impacts of all-time anthropogenic emissions on the global mercury cycle. *Global Biogeochemical Cycles, 27*(2), 410-421.

Ancora, Maria Pia, Zhang, Lei, Wang, Shuxiao, Schreifels, Jeremy J, & Hao, Jiming. (2016). Meeting Minamata: Cost-effective compliance options for atmospheric mercury control in Chinese coal-fired power plants. *Energy Policy, 88*, 485-494.

Anderlohr, C, Brachert, L, Mertens, J, & Schaber, K. (2015). Collection and generation of sulfuric acid aerosols in a wet electrostatic precipitator. *Aerosol Science and Technology, 49*(3), 144-151.

Andreae, MO, & Gelencsér, A. (2006). Black carbon or brown carbon? The nature of light-absorbing carbonaceous aerosols. *Atmospheric Chemistry and Physics, 6*(10), 3131-3148.

Ångström, Anders. (1929). On the atmospheric transmission of sun radiation and on dust in the air. *Geografiska Annaler, 11*(2), 156-166.

Bäck, Andreas. (2009). Enhancing ESP efficiency for high resistivity fly ash by reducing the flue gas temperature *Electrostatic Precipitation* (pp. 406-411): Springer.

Bailey, Roger, Fielding, Louise, Young, Andy, & Griffith, Chris. (2007). Effect of ozone and open air factor against aerosolized Micrococcus luteus. *Journal of food protection, 70*(12), 2769-2773.

Baker, Edward T, & Lavelle, J William. (1984). The effect of particle size on the light attenuation coefficient of natural suspensions. *Journal of Geophysical Research: Oceans, 89*(C5), 8197-8203.

Barreras, F, Amaveda, H, & Lozano, A. (2002). Transient high-frequency ultrasonic water atomization. *Experiments in Fluids, 33*(3), 405-413.

Bayless, David J, Jewmaidang, Jirasak, Tanneer, Srinivas, & Birru, Rajkumar. (2000). Kinetics of low-temperature homogeneous SO3 formation for use in flue gas conditioning for improved electrostatic precipitator performance. *Proceedings of the Combustion Institute, 28*(2), 2499-2505.

Bergstrom, Robert W, Pilewskie, Peter, Russell, Philip B, Redemann, Jens, Bond, Tami C, Quinn, Patricia K, & Sierau, Berko. (2007). Spectral absorption properties of atmospheric aerosols. *Atmospheric Chemistry and Physics, 7*(23), 5937-5943.

Bielawski, Gregory T, Schmeida, Melanie J, White, Nicholas T, & Internafional, Power-Gen. (2013). Air Quality Control System Choices for US Utility Power Plants. *Power-Gen International*.

Bittner, B, & Kissel, T. (1999). Ultrasonic atomization for spray drying: a versatile technique for the preparation of protein loaded biodegradable microspheres. *Journal of microencapsulation, 16*(3), 325-341.

Bolashikov, Zhecho Dimitrov, & Melikov, Arsen Krikor. (2009). Methods for air cleaning and protection of building occupants from airborne pathogens. *Building and Environment, 44*(7), 1378-1385.

Bologa, A, Paur, H-R, Seifert, H, Wäscher, Th, & Woletz, K. (2009). Novel wet electrostatic precipitator for collection of fine aerosol. *Journal of Electrostatics, 67*(2-3), 150-153.

Bologa, Andrei M, Paur, H-R, Seifert, Helmut, & Wascher, T. (2005). Pilot-plant testing of a novel electrostatic collector for submicrometer particles. *IEEE transactions on industry applications, 41*(4), 882-890.

Bond, Tami C. (2001). Spectral dependence of visible light absorption by carbonaceous particles emitted from coal combustion. *Geophysical Research Letters, 28*(21), 4075-4078.

Bond, Tami C, & Bergstrom, Robert W. (2006). Light absorption by carbonaceous particles: An investigative review. *Aerosol science and technology, 40*(1), 27-67.

Bond, Tami C, Doherty, Sarah J, Fahey, DW, Forster, PM, Berntsen, T, DeAngelo, BJ, . . . Koch, Dorothy. (2013). Bounding the role of black carbon in the climate system: A scientific assessment. *Journal of Geophysical Research: Atmospheres, 118*(11), 5380-5552.

Bond, Tami C, Streets, David G, Yarber, Kristen F, Nelson, Sibyl M, Woo, Jung‐Hun, & Klimont, Zbigniew. (2004). A technology‐based global inventory of black and organic carbon emissions from combustion. *Journal of Geophysical Research: Atmospheres, 109*(D14).

Brown, Sanborn Conner. (1966). Introduction to electrical discharges in gases.

Bruce, Charles W, Stromberg, Thor F, Gurton, Kristan P, & Mozer, JB. (1991). Trans-spectral absorption and scattering of electromagnetic radiation by diesel soot. *Applied optics, 30*(12), 1537-1546.

Calvert, Seymour, & Englund, Harold M. (1984). *Handbook of air pollution technology*. Hoboken, NJ: Wiley-Interscience.

Cao, Guoliang, Zhang, Xiaoye, & Zheng, Fangcheng. (2006). Inventory of black carbon and organic carbon emissions from China. *Atmospheric Environment, 40*(34), 6516-6527.

Chang, John CS, & Ghorishi, S Behrooz. (2003). Simulation and evaluation of elemental mercury concentration increase in flue gas across a wet scrubber. *Environmental science & technology, 37*(24), 5763-5766.

Chen, Meng-Tse, Jiang, Chunqi, Vernier, P Thomas, Wu, Yu-Hsuan, & Gundersen, Martin A. (2009). Two-dimensional nanosecond electric field mapping based on cell electropermeabilization. *PMC biophysics, 2*(1), 9.

Chen, Tzu-Ming, Tsai, Chuen-Jinn, Yan, Shaw-Yi, & Li, Shou-Nan. (2014). An efficient wet electrostatic precipitator for removing nanoparticles, submicron and micron-sized particles. *Separation and Purification Technology, 136*, 27-35.

Cheng, Yafang, Zheng, Guangjie, Wei, Chao, Mu, Qing, Zheng, Bo, Wang, Zhibin, . . . Carmichael, Gregory. (2016). Reactive nitrogen chemistry in aerosol water as a source of sulfate during haze events in China. *Science advances, 2*(12), e1601530.

Cheng, Yu-Hsiang, & Tsai, Chuen-Jinn. (1998). Factors influencing pressure drop through a dust cake during filtration. *Aerosol Science and Technology, 29*(4), 315-328.

Chick, H. (1908). An Investigation of the Laws of Disinfection. *The Journal of Hygiene, 8*(1), 92-158. doi: http://dx.doi.org/10.1021/es203770q.
ChinaFAQs. (2012). *China Adopts World-Class Pollutant Emissions Standards for Coal Power Plants*. Washington DC: Retrieved from http://www.chinafaqs.org/files/chinainfo/China%20FAQs%20Emission%20Standards%20v1.4_0.pdf.
Cho, Jenny G, Dee, Scott A, Deen, John, Guedes, Alonso, Trincado, Carlos, Fano, Eduardo, . . . Murtaugh, Michael P. (2006). Evaluation of the effects of animal age, concurrent bacterial infection, and pathogenicity of porcine reproductive and respiratory syndrome virus on virus concentration in pigs. *American journal of veterinary research, 67*(3), 489-493.
Clack, Herek L. (2006a). Bimodal fly ash size distributions and their influence on gas-particle mass transfer during electrostatic precipitation. *Fuel processing technology, 87*(11), 987-996.
Clack, Herek L. (2006b). Mass transfer within electrostatic precipitators: in-flight adsorption of mercury by charged suspended particulates. *Environmental science & technology, 40*(11), 3617-3622.
Clack, Herek L. (2006c). Particle size distribution effects on gas-particle mass transfer within electrostatic precipitators. *Environmental science & technology, 40*(12), 3929-3933.
Clack, Herek L. (2009). Mercury capture within coal-fired power plant electrostatic precipitators: model evaluation. *Environmental science & technology, 43*(5), 1460-1466.
Clack, Herek L. (2012). Estimates of increased black carbon emissions from electrostatic precipitators during powdered activated carbon injection for mercury emissions control. *Environmental science & technology, 46*(13), 7327-7333.
Clack, Herek L. (2014). Particulate carbon emissions from electrostatic precipitators used for mercury emissions control: operational factors and implications. *Air Quality, Atmosphere & Health, 7*(2), 155-163.
Clack, Herek L. (2015). Simultaneous removal of particulate matter and gas-phase pollutants within electrostatic precipitators: coupled in-flight and wall-bounded adsorption. *Aerosol Air Qual. Res, 15*(6), 2445-2455.
Clack, Herek L. (2017). Numerical Simulation of Simultaneous Electrostatic Precipitation and Trace Gas Adsorption: Electrohydrodynamic Effects. *Frontiers in Energy Research, 5*, 3.
Clague, ADH, Donnet, JB, Wang, TK, & Peng, JCM. (1999). A comparison of diesel engine soot with carbon black1. *Carbon, 37*(10), 1553-1565.
Colby, Michelle M. (2013). *DHS S&T's Agricultural Defense Program Overview*. Paper presented at the National Center for Foreign Animal and Zoonotic Disease Defense (FAZD). http://iiad.tamu.edu/wp-content/uploads/2013/07/Colby.pdf
Cooper, C David, & Alley, Forrest Christopher. (2011). *Air pollution control: A design approach*: Waveland Press.
Cox, Christopher S, & Wathes, Christopher M. (1995). *Bioaerosols handbook*: crc press.
Cui, Lin, Li, Yue, Tang, Yuzhou, Shi, Yifei, Wang, Qingsong, Yuan, Xueliang, & Kellett, Jon. (2018). Integrated assessment of the environmental and economic effects of an ultra-clean flue gas treatment process in coal-fired power plant. *Journal of Cleaner Production*.
Dai, Dongjuan, Prussin, Aaron J, Marr, Linsey C, Vikesland, Peter J, Edwards, Marc A, & Pruden, Amy. (2017). Factors Shaping the Human Exposome in the Built Environment:

Opportunities for Engineering Control. *Environmental Science & Technology, 51*(14), 7759-7774.
Danzomo, Bashir Ahmed, Salami, ME, Jibrin, S, Khan, MR, & Nor, IM. (2012). Performance evaluation of wet scrubber system for industrial air pollution control. *J Eng Appl Sci, 7*(12), 1669-1677.
Davis, Wayne T, & Buonicore, Anthony J. (2000). *Air pollution engineering manual*: Wiley New York.
Dee, Scott. (2011). An assessment of air filtration for reducing the risk of PRRSV infection in large breeding herds in swine dense regions (N. P. Board, Trans.).
Dee, Scott, Deen, John, Rossow, Kurt, Weise, Carrie, Eliason, Roger, Otake, Satoshi, . . . Pijoan, Carlos. (2003). Mechanical transmission of porcine reproductive and respiratory syndrome virus throughout a coordinated sequence of events during warm weather. *Canadian journal of veterinary research, 67*(1), 12.
Dee, Scott, Otake, Satoshi, Oliveira, Simone, & Deen, John. (2009). Evidence of long distance airborne transport of porcine reproductive and respiratory syndrome virus and Mycoplasma hyopneumoniae. *Veterinary research, 40*(4), 1-13.
Deng, Junjun, Zhang, Yanru, Hong, Youwei, Xu, Lingling, Chen, Yanting, Du, Wenjiao, & Chen, Jinsheng. (2016). Optical properties of PM2. 5 and the impacts of chemical compositions in the coastal city Xiamen in China. *Science of the Total Environment, 557*, 665-675.
Dobbins, RA, Fletcher, Robert A, & Chang, H-C. (1998). The evolution of soot precursor particles in a diffusion flame. *Combustion and flame, 115*(3), 285-298.
DOE. (2015). *Specification for HEPA Filters Used by DOE Contractors* (DOE-STD-3020-2015). Retrieved from https://www.standards.doe.gov/standards-documents/3000/3020-astd-2015/@@images/file.
Dombrowski, Katherine, Richardson, Carl, Padilla, Jackie, Chang, Ramsay, Archer, Greg, Fisher, Kevin, . . . Brickett, Lynn. (2008). *Evaluation of novel mercury sorbents and balance-of-plant impacts at Stanton Unit 1.* Paper presented at the DOE-US EPA-EPRI-AWMA Power Plant Air Pollution Control "Mega" Symposium, Baltimore, Maryland, USA.
Done, SH, Paton, DJ, & White, MEC. (1996). Porcine reproductive and respiratory syndrome (PRRS): a review, with emphasis on pathological, virological and diagnostic aspects. *British veterinary journal, 152*(2), 153-174.
Douwes, J, Thorne, Pl, Pearce, N, & Heederik, D. (2003). Bioaerosol health effects and exposure assessment: progress and prospects. *The Annals of occupational hygiene, 47*(3), 187-200.
Downs, William, & Farthing, George. (2007). Dynamic halogenation of sorbents for the removal of mercury from flue gases: Google Patents.
EIA. (2012). *Annual Energy Review 2011*. (0160910064). Government Printing Office.
EIA. (2014a). *Annual Energy Outlook (AEO) 2014 Early Release Overview*. Retrieved from http://pages.hmc.edu/evans/AEOearly2014.pdf.
EIA (Producer). (2014b). Coal-fired power plant operators consider emissions compliance strategies. Retrieved from https://www.eia.gov/todayinenergy/detail.php?id=15611
EIA. (2016a). *Electric Power Annual 2015*. Washington, DC: Retrieved from http://large.stanford.edu/courses/2017/ph240/weisenberg1/docs/epa-2015.pdf.
EIA. (2016b). *International Energy Data and Analysis - China*. Retrieved from https://www.eia.gov/beta/international/analysis_includes/countries_long/China/china.pdf.

Elazhary, MA, & Derbyshire, JB. (1979). Effect of temperature, relative humidity and medium on the aerosol stability of infectious bovine rhinotracheitis virus. *Canadian Journal of Comparative Medicine, 43*(2), 158.

Elghazaly, Hany MA, & Castle, GS Peter. (1987). Analysis of the multisibling instability of charged liquid drops. *IEEE transactions on industry applications*(1), 108-113.

Ellenbecker, Michael J, & Leith, David. (1980). The effect of dust retention on pressure drop in a high velocity pulse-jet fabric filter. *Powder Technology, 25*(2), 147-154.

EPA, U.S. (2001). Environmental protection agency method 1601: male-specific (f+) and somatic coliphage in water by two-step. Washington, DC.

Espinola, Aida, Miguel, Pablo Mourente, Salles, Milton Roedel, & Pinto, Ailton Ribeiro. (1986). Electrical properties of carbons—resistance of powder materials. *Carbon, 24*(3), 337-341.

Esworthy, Robert. (2013). Air quality: EPA's 2013 changes to the particulate matter (PM) standard. *Congressional Research Service*, 7-5700.

Falkenstein, Zoran, & Coogan, John J. (1997). Microdischarge behaviour in the silent discharge of nitrogen-oxygen and water-air mixtures. *Journal of Physics D: Applied Physics, 30*(5), 817.

Farnoosh, Niloofar, Adamiak, K, & Castle, GSP. (2010). 3-D numerical analysis of EHD turbulent flow and mono-disperse charged particle transport and collection in a wire-plate ESP. *Journal of Electrostatics, 68*(6), 513-522.

Farnsworth, James E, Goyal, Sagar M, Kim, Seung Won, Kuehn, Thomas H, Raynor, Peter C, Ramakrishnan, MA, . . . Tang, Weihua. (2006). Development of a method for bacteria and virus recovery from heating, ventilation, and air conditioning (HVAC) filters. *Journal of Environmental Monitoring, 8*(10), 1006-1013.

Feeley III, Thomas J, Skone, Timothy J, Stiegel Jr, Gary J, McNemar, Andrea, Nemeth, Michael, Schimmoller, Brian, . . . Manfredo, Lynn. (2008). Water: A critical resource in the thermoelectric power industry. *Energy, 33*(1), 1-11.

Fife, JP, Ozkan, HE, Derksen, RC, & Grewal, PS. (2006). Using computational fluid dynamics to predict damage of a biological pesticide during passage through a hydraulic nozzle. *Biosystems engineering, 94*(3), 387-396.

Fisher, Gerald L, Chang, DPY, & Brummer, Margaret. (1976). Fly ash collected from electrostatic precipitators: microcrystalline structures and the mystery of the spheres. *Science, 192*(4239), 553-555.

Fröhlich-Nowoisky, Janine, Kampf, Christopher J, Weber, Bettina, Huffman, J Alex, Pöhlker, Christopher, Andreae, Meinrat O, . . . Elbert, Wolfgang. (2016). Bioaerosols in the Earth system: Climate, health, and ecosystem interactions. *Atmospheric Research, 182*, 346-376.

Fujimura, Kei E, Demoor, Tine, Rauch, Marcus, Faruqi, Ali A, Jang, Sihyug, Johnson, Christine C, . . . Lukacs, Nicholas W. (2014). House dust exposure mediates gut microbiome Lactobacillus enrichment and airway immune defense against allergens and virus infection. *Proceedings of the National Academy of Sciences, 111*(2), 805-810.

Fuzzi, Sandro, Baltensperger, U, Carslaw, K, Decesari, S, Denier Van Der Gon, H, Facchini, MC, . . . Lohmann, U. (2015). Particulate matter, air quality and climate: lessons learned and future needs. *Atmospheric chemistry and physics, 15*(14), 8217-8299.

Gaunt, Lindsey F, Beggs, Clive B, & Georghiou, George E. (2006). Bactericidal action of the reactive species produced by gas-discharge nonthermal plasma at atmospheric pressure: a review. *IEEE Transactions on Plasma Science, 34*(4), 1257-1269.

Geldart, Derek. (1973). Types of gas fluidization. *Powder technology, 7*(5), 285-292.

Ghorishi, S Behrooz, Keeney, Robert M, Serre, Shannon D, Gullett, Brian K, & Jozewicz, Wojciech S. (2002). Development of a Cl-impregnated activated carbon for entrained-flow capture of elemental mercury. *Environmental science & technology, 36*(20), 4454-4459.

Gibb, Herman, & O'Leary, Keri Grace. (2014). Mercury exposure and health impacts among individuals in the artisanal and small-scale gold mining community: a comprehensive review. *Environmental health perspectives, 122*(7), 667.

Gladney, Ernest S, Small, John A, Gordon, Glen E, & Zoller, William H. (1976). Composition and size distribution of in-stack particulate material at a coal-fired power plant. *Atmospheric Environment (1967), 10*(12), 1071-1077.

Granite, Evan J, Pennline, Henry W, & Senior, Constance. (2015). *Mercury Control: for Coal-Derived Gas Streams*: John Wiley & Sons.

Gundel, LA, Dod, RL, Rosen, H, & Novakov, T. (1984). The relationship between optical attenuation and black carbon concentration for ambient and source particles. *Science of the Total Environment, 36*, 197-202.

Guttikunda, Sarath K, & Jawahar, Puja. (2014). Atmospheric emissions and pollution from the coal-fired thermal power plants in India. *Atmospheric Environment, 92*, 449-460.

Górny, Rafal L, Dutkiewicz, Jacek, & Krysinska-Traczyk, E. (1999). Size distribution of bacterial and fungal bioaerosols in indoor air. *Ann Agric Environ Med, 6*, 105-113.

Hansen, ADA, Rosen, H, & Novakov, T. (1984). The aethalometer—an instrument for the real-time measurement of optical absorption by aerosol particles. *Science of the Total Environment, 36*, 191-196.

Harrison, Roy M, & Yin, Jianxin. (2000). Particulate matter in the atmosphere: which particle properties are important for its effects on health? *Science of the total environment, 249*(1-3), 85-101.

Haynes, Brian S, & Wagner, H Gg. (1981). Soot formation. *Progress in energy and combustion science, 7*(4), 229-273.

Heidelberg, JF, Shahamat, M, Levin, M, Rahman, I, Stelma, G, Grim, C, & Colwell, RR. (1997). Effect of aerosolization on culturability and viability of gram-negative bacteria. *Applied and Environmental Microbiology, 63*(9), 3585-3588.

Heimbuch, Brian K, Wallace, William H, Kinney, Kimberly, Lumley, April E, Wu, Chang-Yu, Woo, Myung-Heui, & Wander, Joseph D. (2011). A pandemic influenza preparedness study: use of energetic methods to decontaminate filtering facepiece respirators contaminated with H1N1 aerosols and droplets. *American journal of infection control, 39*(1), e1-e9.

Heinlin, Julia, Morfill, Gregor, Landthaler, Michael, Stolz, Wilhelm, Isbary, Georg, Zimmermann, Julia L, . . . Karrer, Sigrid. (2010). Plasma medicine: possible applications in dermatology. *JDDG: Journal der Deutschen Dermatologischen Gesellschaft, 8*(12), 968-976.

Heisler, Steven Ludvic, & Friedlander, SK. (1977). Gas-to-particle conversion in photochemical smog: Aerosol growth laws and mechanisms for organics. *Atmospheric Environment (1967), 11*(2), 157-168.

Herr, CEW, Zur Nieden, A, Jankofsky, M, Stilianakis, NI, Boedeker, RH, & Eikmann, TF. (2003). Effects of bioaerosol polluted outdoor air on airways of residents: a cross sectional study. *Occupational and environmental medicine, 60*(5), 336-342.

Hinds, William C. (2012). *Aerosol technology: properties, behavior, and measurement of airborne particles*: John Wiley & Sons.

Hirleman, E Dan, Oechsle, V, & Chigier, NA. (1984). Response characteristics of laser diffraction particle size analyzers: optical sample volume extent and lens effects. *Optical Engineering, 23*(5), 235610.

Hitzenberger, R, & Tohno, S. (2001). Comparison of black carbon (BC) aerosols in two urban areas–concentrations and size distributions. *Atmospheric Environment, 35*(12), 2153-2167.

Hodkinson, JR. (1966). *The optical measurement of aerosols*: Academic Press, London and New York.

Holtkamp, Derald J, Kliebenstein, James B, Neumann, Eric J, Zimmerman, Jeffrey J, Rotto, Hans F, Yoder, Tiffany K, . . . Haley, Charles A. (2013). Assessment of the economic impact of porcine reproductive and respiratory syndrome virus on United States pork producers. *Journal of Swine Health and Production, 21*(2), 72-84.

Holzer, F, Kopinke, FD, & Roland, U. (2005). Influence of ferroelectric materials and catalysts on the performance of non-thermal plasma (NTP) for the removal of air pollutants. *Plasma Chemistry and Plasma Processing, 25*(6), 595-611.

Hospodsky, D, Yamamoto, N, Nazaroff, WW, Miller, D, Gorthala, S, & Peccia, J. (2015). Characterizing airborne fungal and bacterial concentrations and emission rates in six occupied children's classrooms. *Indoor air, 25*(6), 641-652.

Huang, Ru-Jin, Zhang, Yanlin, Bozzetti, Carlo, Ho, Kin-Fai, Cao, Jun-Ji, Han, Yongming, . . . Canonaco, Francesco. (2014). High secondary aerosol contribution to particulate pollution during haze events in China. *Nature, 514*(7521), 218.

Huang, Sheng-Hsiu, & Chen, Chih-Chieh. (2002). Ultrafine aerosol penetration through electrostatic precipitators. *Environmental science & technology, 36*(21), 4625-4632.

Jakober, C, & Phillips, T. (2008). Evaluation of Ozone Emissions From Portable Indoor Air Cleaners: Electrostatic Precipitators and Ionizers: California Environmental Protection Agency, Air Resources Board.

Jeong, Sang Hyun, Shim, Sung Hoon, Song, Dong Keun, Hong, Won Seok, Hong, Jeong Hee, & Lee, Sang-Sup. (2013). Performance of a pilot-scale wet electrostatic precipitator for the control of sulfuric acid mist and fine particulates. *Polish Journal of Environmental Studies, 22*(2), 409-415.

Keffaber, KK. (1989). Reproductive failure of unknown etiol-ogy. *Am. Assoc. Swine Pract. Newsl, 1*, 1-9.

Kesavan, Jana, & Sagripanti, Jose-Luis. (2012). Disinfection of airborne organisms by ultraviolet-C radiation and sunlight: ARMY EDGEWOOD CHEMICAL BIOLOGICAL CENTER APG MD RESEARCH AND TECHNOLOGY DIR.

Kestin, Joseph, Sokolov, Mordechai, & Wakeham, William A. (1978). Viscosity of liquid water in the range− 8 C to 150 C. *Journal of Physical and Chemical Reference Data, 7*(3), 941-948.

Kim, D, Chin, M, Yu, H, Eck, TF, Sinyuk, A, Smirnov, A, & Holben, BN. (2011). Dust optical properties over North Africa and Arabian Peninsula derived from the AERONET dataset. *Atmospheric Chemistry and Physics, 11*(20), 10733-10741.

Kim, Hyun-Ha. (2004). Nonthermal plasma processing for air-pollution control: a historical review, current issues, and future prospects. *Plasma Processes and Polymers, 1*(2), 91-110.
Kim, Ki-Hyun, Kabir, Ehsanul, & Kabir, Shamin. (2015). A review on the human health impact of airborne particulate matter. *Environment international, 74*, 136-143.
Kirchstetter, Thomas W, & Novakov, T. (2007). Controlled generation of black carbon particles from a diffusion flame and applications in evaluating black carbon measurement methods. *Atmospheric Environment, 41*(9), 1874-1888.
Kirchstetter, Thomas W, Novakov, T, & Hobbs, Peter V. (2004). Evidence that the spectral dependence of light absorption by aerosols is affected by organic carbon. *Journal of Geophysical Research: Atmospheres, 109*(D21).
Krzyzanowski, Michal, & Cohen, Aaron. (2008). Update of WHO air quality guidelines. *Air Quality, Atmosphere & Health, 1*(1), 7-13.
Kuklinski, Teresa (Producer). (2013). Environmental Standards for Vehicles in the U.S. and Their Impact on BC Emissions. [Presentation Slides] Retrieved from https://www.epa.gov/sites/production/files/2014-05/documents/env-standards-for-vehicles.pdf
Kummer, Volker, & Thiel, Wolf R. (2008). Bioaerosols–sources and control measures. *International journal of hygiene and environmental health, 211*(3-4), 299-307.
Kuwahara, Takuya, Okubo, Masaaki, Kuroki, Tomoyuki, Kametaka, Hideya, & Yamamoto, Toshiaki. (2011). Odor removal characteristics of a laminated film-electrode packed-bed nonthermal plasma reactor. *Sensors, 11*(6), 5529-5542.
Lamminen, Mikko, Wood, James, Walker, Harold, Chin, Yu-Ping, He, Yongtian, & Traina, Samuel J. (2001). Effect of flue gas desulfurization (FGD) by-product on water quality at an underground coal mine. *Journal of environmental quality, 30*(4), 1371-1381.
Lang, Robert J. (1962). Ultrasonic atomization of liquids. *The journal of the acoustical society of America, 34*(1), 6-8.
Lapple, CE. (1961). Characteristics of particles and particle dispersoids. *Stanford Research Institute Journal, 5*, 94.
Lax, Simon, Smith, Daniel P, Hampton-Marcell, Jarrad, Owens, Sarah M, Handley, Kim M, Scott, Nicole M, . . . Weiss, Sophie. (2014). Longitudinal analysis of microbial interaction between humans and the indoor environment. *Science, 345*(6200), 1048-1052.
Lee, Eric Monsu, & Clack, Herek L. (2010). In situ detection of altered particle size distributions during simulated powdered sorbent injection for mercury emissions control. *Energy & Fuels, 24*(10), 5410-5417.
Lee, Eric Monsu, & Clack, Herek L. (2016). Powder resistivity inferred differential collection of heterogeneous coal fly ash and powered activated carbon admixtures within a cylindrical electrostatic precipitator. *Emission Control Science and Technology, 2*(1), 33-43.
Lee, T, Grinshpun, SA, Martuzevicius, D, Adhikari, A, Crawford, CM, Luo, J, & Reponen, T. (2006). Relationship between indoor and outdoor bioaerosols collected with a button inhalable aerosol sampler in urban homes. *Indoor air, 16*(1), 37-47.
Lefebvre, A.H. (1980). Airblast Atomization. *Progress in Energy and Combustion Science, 6*, 233-261.
Lefebvre, A.H. (1989). *Atomization and Sprays*. New York: Hemisphere.
Lefebvre, AH, & Wang, XF. (1987). Mean drop sizes from pressure-swirl nozzles. *Journal of propulsion and power, 3*(1), 11-18.

Lefebvre, AH, Wang, XF, & Martin, CA. (1988). Spray characteristics of aerated-liquid pressure atomizers. *Journal of Propulsion and Power, 4*(4), 293-298.
Levy, Robert C, Remer, Lorraine A, & Dubovik, Oleg. (2007). Global aerosol optical properties and application to Moderate Resolution Imaging Spectroradiometer aerosol retrieval over land. *Journal of Geophysical Research: Atmospheres, 112*(D13).
Li, Jinyu, & Dennehy, John J. (2011). Differential bacteriophage mortality on exposure to copper. *Applied and environmental microbiology, 77*(19), 6878-6883.
Li, Xiaodong, Li, Jingwei, Wu, Dongli, Lu, Shengyong, Zhou, Chenyang, Qi, Zhifu, . . . Yan, Jianhua. (2018). Removal effect of the low-low temperature electrostatic precipitator on polycyclic aromatic hydrocarbons. *Chemosphere*.
Liang, Yongdong, Wu, Yan, Sun, Ke, Chen, Qi, Shen, Fangxia, Zhang, Jue, . . . Fang, Jing. (2012). Rapid inactivation of biological species in the air using atmospheric pressure nonthermal plasma. *Environmental science & technology, 46*(6), 3360-3368.
Lin, Guan-Yu, Chen, Tzu-Ming, & Tsai, Chuen-Jinn. (2012). A modified deutsch-anderson equation for predicting the nanoparticle collection efficiency of electrostatic precipitators. *Aerosol and Air Quality Research, 12*(5), 697-706.
Lin, Guan-Yu, Tsai, Chuen-Jinn, Chen, Sheng-Chieh, Chen, Tzu-Ming, & Li, Shou-Nan. (2010). An efficient single-stage wet electrostatic precipitator for fine and nanosized particle control. *Aerosol Science and Technology, 44*(1), 38-45.
Lin, Guangxing, Penner, Joyce E, & Clack, Herek L. (2014). Radiative forcing associated with particulate carbon emissions resulting from the use of mercury control technology. *Environmental science & technology, 48*(17), 10519-10523.
Linak, William P, Miller, C Andrew, & Wendt, Jost OL. (2000). Comparison of particle size distributions and elemental partitioning from the combustion of pulverized coal and residual fuel oil. *Journal of the Air & Waste Management Association, 50*(8), 1532-1544.
Lippmann, M. (1989). Health effects of ozone. A critical review. *JAPCA, 39*(5), 672-695.
Lorenzetto, GE, & Lefebvre, Arthur H. (1977). Measurements of drop size on a plain-jet airblast atomizer. *AIAA journal, 15*(7), 1006-1010.
Lowen, Anice C, Mubareka, Samira, Steel, John, & Palese, Peter. (2007). Influenza virus transmission is dependent on relative humidity and temperature. *PLoS pathogens, 3*(10), e151.
MacNee, W, & Donaldson, K. (2003). Mechanism of lung injury caused by PM10 and ultrafine particles with special reference to COPD. *European Respiratory Journal, 21*(40 suppl), 47s-51s.
Martins, J Vanderlei, Artaxo, Paulo, Liousse, Catherine, Reid, Jeffrey S, Hobbs, Peter V, & Kaufman, Yoram J. (1998). Effects of black carbon content, particle size, and mixing on light absorption by aerosols from biomass burning in Brazil. *Journal of Geophysical Research: Atmospheres, 103*(D24), 32041-32050.
McAdams, R. (2001). Prospects for non-thermal atmospheric plasmas for pollution abatement. *Journal of Physics D: Applied Physics, 34*(18), 2810.
McCain, Joseph D, Gooch, John P, & Smith, Wallace B. (1975). Results of field measurements of industrial particulate sources and electrostatic precipitator performance. *Journal of the Air Pollution Control Association, 25*(2), 117-121.
McCallion, Orla NM, Taylor, Kevin MG, Thomas, Marian, & Taylor, Anthony J. (1995). Nebulization of fluids of different physicochemical properties with air-jet and ultrasonic nebulizers. *Pharmaceutical research, 12*(11), 1682-1688.

McKinney, Kelly R, Gong, Yu Yang, & Lewis, Thomas G. (2006). Environmental transmission of SARS at Amoy Gardens. *Journal of environmental health, 68*(9), 26.
Meij, Ruud, Vredenbregt, Leo HJ, & Winkel, Henk te. (2002). The fate and behavior of mercury in coal-fired power plants. *Journal of the Air & Waste Management Association, 52*(8), 912-917.
Memarzadeh, Farhad, Olmsted, Russell N, & Bartley, Judene M. (2010). Applications of ultraviolet germicidal irradiation disinfection in health care facilities: effective adjunct, but not stand-alone technology. *American journal of infection control, 38*(5), S13-S24.
MEP. (2011). *Emission standard of air pollutants for thermal power plants*. Beijing: Retrieved from http://www.gbstandards.org/GB_standards/GB-13223-2011.html.
MEP. (2012). *Ambient Air Quality Standards*. (GB3095-2012). Beijing: Retrieved from http://kjs.mep.gov.cn/hjbhbz/bzwb/dqhjbh/dqhjzlbz/201203/W020120410330232398521.pdf.
Merritt, Randy Lee, & Bush, P Vann. (1997). Status and future of baghouses in the utility industry. *Journal of the Air & Waste Management Association, 47*(6), 704-709.
Miaskiewicz-Peska, Ewa, & Lebkowska, Maria. (2012). Comparison of aerosol and bioaerosol collection on air filters. *Aerobiologia, 28*(2), 185-193.
Mie, Gustav. (1908). Beiträge zur Optik trüber Medien, speziell kolloidaler Metallösungen. *Annalen der physik, 330*(3), 377-445.
Millerick-May, M. L., Ferry, E., Benjamin, M., May, G. A. . (2016). *Routine manure removal from swine operations: A potential mechanism for pathogen dispersion*. Paper presented at the Michigan Pork Symposium, Lansing, Michigan.
Montilla, E, Mogo, S, Cachorro, V, Lopez, J, & Frutos, A de. (2011). Absorption, scattering and single scattering albedo of aerosols obtained from in situ measurements in the subarctic coastal region of Norway. *Atmospheric Chemistry and Physics Discussions*(1), 2161-2182.
Moretti, Albert L, Jones, Christopher S, & Asia, Power-Gen. (2012). Advanced emissions control technologies for coal-fired power plants. *Babcock & Wilox power generation group, Bangkok, Thailand. Technical Paper, BR-1886*.
Nazaroff, William W. (2016). Indoor bioaerosol dynamics. *Indoor Air, 26*(1), 61-78.
Niven, Ralph W, Ip, Anna Y, Mittelman, S, Prestrelski, SJ, & Arakawa, T. (1995). Some factors associated with the ultrasonic nebulization of proteins. *Pharmaceutical research, 12*(1), 53-59.
Noriega, Estefanía, Shama, Gilbert, Laca, Adriana, Díaz, Mario, & Kong, Michael G. (2011). Cold atmospheric gas plasma disinfection of chicken meat and chicken skin contaminated with Listeria innocua. *Food microbiology, 28*(7), 1293-1300.
Oberlin, A. (1984). Carbonization and graphitization. *Carbon, 22*(6), 521-541.
Otake, Satoshi, Dee, Scott, Corzo, Cesar, Oliveira, Simone, & Deen, John. (2010). Long-distance airborne transport of infectious PRRSV and Mycoplasma hyopneumoniae from a swine population infected with multiple viral variants. *Veterinary microbiology, 145*(3-4), 198-208.
Owen, Thomas W, Al-Kaysi, Rabih O, Bardeen, Christopher J, & Cheng, Quan. (2007). Microgravimetric immunosensor for direct detection of aerosolized influenza A virus particles. *Sensors and Actuators B: Chemical, 126*(2), 691-699.
Pöschl, Ulrich. (2005). Atmospheric aerosols: composition, transformation, climate and health effects. *Angewandte Chemie International Edition, 44*(46), 7520-7540.

Page, AL, Elseewi, Ahmed A, & Straughan, IR. (1979). Physical and chemical properties of fly ash from coal-fired power plants with reference to environmental impacts *Residue Reviews* (pp. 83-120): Springer.

Pavlish, John H, Sondreal, Everett A, Mann, Michael D, Olson, Edwin S, Galbreath, Kevin C, Laudal, Dennis L, & Benson, Steven A. (2003). Status review of mercury control options for coal-fired power plants. *Fuel Processing Technology, 82*(2-3), 89-165.

Peccia, J., Milton, D.K., Reponen, T., & Hill, J. (2008). A Role for Environmental Engineering and Science in Preventing Bioaerosol-Related Disease. *Environmental Science & Technology, 42*(13), 4631-4637.

Peccia, Jordan, & Kwan, Sarah E. (2016). Buildings, beneficial microbes, and health. *Trends in microbiology, 24*(8), 595-597.

Pecson, B.M., Martin, L.V., & Kohn, T. (2009). Quantitative PCR for determining the infectivity of bacteriophage MS2 upon inactivation by heat, UV-B radiation, and singlet oxygen: Advantages and limitations of an enzymatic treatment to reduce false-positive results. *Applied and Environmental Microbiology, 75*, 5544-5554.

Perni, Stefano, Liu, David W, Shama, Gilbert, & Kong, Michael G. (2008). Cold atmospheric plasma decontamination of the pericarps of fruit. *Journal of food protection, 71*(2), 302-308.

Phipps, Paul R, Pharm, B, & Gonda, Igor. (1990). Droplets produced by medical nebulizers: some factors affecting their size and solute concentration. *Chest, 97*(6), 1327-1332.

Pitkin, Andrea, Deen, John, & Dee, Scott. (2009). Use of a production region model to assess the airborne spread of porcine reproductive and respiratory syndrome virus. *Veterinary microbiology, 136*(1-2), 1-7.

Pitkin, Andrea, Otake, Satoshi, Dee, Scott, & ACVM, DVM MS PhD Dip. (2009). Biosecurity protocols for the prevention of spread of porcine reproductive and respiratory syndrome virus. *Swine Disease Eradication Center. University of Minnesota College of Veterinary Medicine*, 1-17.

Pohl, Steve. (2012, Apr 18, 2012). Filtration Solutions for PRRS. *National Hog Farmer*

Prabhu, Vinit, Kim, Taehoon, Khakpour, Yasmin, Serre, Shannon D, & Clack, Herek L. (2012). Evidence of powdered activated carbon preferential collection and enrichment on electrostatic precipitator discharge electrodes during sorbent injection for mercury emissions control. *Fuel processing technology, 93*(1), 8-12.

Prabhu, Vinit, Lee, Sangkyoung, & Clack, Herek L. (2011). Electrostatic precipitation of powdered activated carbon and implications for secondary mercury adsorption within electrostatic precipitators. *Energy & Fuels, 25*(3), 1010-1016.

Presto, Albert A, & Granite, Evan J. (2006). Survey of catalysts for oxidation of mercury in flue gas. *Environmental science & technology, 40*(18), 5601-5609.

Pruss, Axel, Kao, Moujahed, Gohs, Uwe, Koscielny, Jürgen, von Versen, Rüdiger, & Pauli, Georg. (2002). Effect of gamma irradiation on human cortical bone transplants contaminated with enveloped and non-enveloped viruses. *Biologicals, 30*(2), 125-133.

Prussin, Aaron J, & Marr, Linsey C. (2015). Sources of airborne microorganisms in the built environment. *Microbiome, 3*(1), 78.

Pudasainee, Deepak, Seo, Yong-Chil, Sung, Jin-Ho, Jang, Ha-Na, & Gupta, Rajender. (2017). Mercury co-beneficial capture in air pollution control devices of coal-fired power plants. *International Journal of Coal Geology, 170*, 48-53.

Qi, Zhifu, Li, Jingwei, Wu, Dongli, Xie, Weiyang, Li, Xiaodong, & Liu, Chunhong. (2017). Particulate matter emission characteristics and removal efficiencies of a low-low temperature electrostatic precipitator. *Energy & Fuels, 31*(2), 1741-1746.

Qian, Jing, Hospodsky, Denina, Yamamoto, Naomichi, Nazaroff, William W, & Peccia, Jordan. (2012). Size‐resolved emission rates of airborne bacteria and fungi in an occupied classroom. *Indoor air, 22*(4), 339-351.

Rajan, R, & Pandit, AB. (2001). Correlations to predict droplet size in ultrasonic atomisation. *Ultrasonics, 39*(4), 235-255.

Ramanathan, VCPJ, Crutzen, PJ, Kiehl, JT, & Rosenfeld, Dm. (2001). Aerosols, climate, and the hydrological cycle. *science, 294*(5549), 2119-2124.

Ramos, Sean, MacLachlan, Matthew, & Melton, Alex. (2017). Impacts of the 2014-2015 Highly Pathogenic Avian Influenza Outbreak on the US Poultry Sector.

Reddy, M Shekar, & Venkataraman, Chandra. (2000). Atmospheric optical and radiative effects of anthropogenic aerosol constituents from India. *Atmospheric Environment, 34*(26), 4511-4523.

Reynolds, James. (2004). MULTI-POLLUTANT CONTROL USING MEMBRANE--BASED UP-FLOW WET ELECTROSTATIC PRECIPITATION: Croll-Reynolds Clean Air Technologies (US).

Riley, Richard L. (1961). Airborne pulmonary tuberculosis. *Bacteriological reviews, 25*(3), 243.

Riley, Richard L, Permutt, Solbert, & Kaufman, James E. (1971). Room air disinfection by ultraviolet irradiation of upper air: further analysis of convective air exchange. *Archives of Environmental Health: An International Journal, 23*(1), 35-39.

Roberts, Casey. (2013). Effluent Limitations Guidelines and Standards for the Steam Electric Power Generating Point Source Category; Proposed Rule 78 Fed. Reg. 34,432 (June 7, 2013).

Robertson, J, & O'reilly, EP. (1987). Electronic and atomic structure of amorphous carbon. *Physical Review B, 35*(6), 2946.

Roessler, DM, & Faxvog, FR. (1979). Optoacoustic measurement of optical absorption in acetylene smoke. *JOSA, 69*(12), 1699-1704.

Russell, PB, Bergstrom, RW, Shinozuka, Y, Clarke, AD, DeCarlo, PF, Jimenez, JL, . . . Strawa, A. (2010). Absorption Angstrom Exponent in AERONET and related data as an indicator of aerosol composition. *Atmospheric Chemistry and Physics, 10*(3), 1155-1169.

Sattel, S, Robertson, J, & Ehrhardt, H. (1997). Effects of deposition temperature on the properties of hydrogenated tetrahedral amorphous carbon. *Journal of applied physics, 82*(9), 4566-4576.

Scala, Fabrizio, & Clack, Herek L. (2008). Mercury emissions from coal combustion: Modeling and comparison of Hg capture in a fabric filter versus an electrostatic precipitator. *Journal of hazardous materials, 152*(2), 616-623.

Schaffer, FL, Soergel, ME, & Straube, DC. (1976). Survival of airborne influenza virus: effects of propagating host, relative humidity, and composition of spray fluids. *Archives of virology, 51*(4), 263-273.

Schneider, J, Kirchner, U, Borrmann, S, Vogt, R, & Scheer, V. (2008). In situ measurements of particle number concentration, chemically resolved size distributions and black carbon content of traffic-related emissions on German motorways, rural roads and in city traffic. *Atmospheric Environment, 42*(18), 4257-4268.

Schneider, Raymond K. (2001). Designing clean room HVAC systems. *ASHRAE journal, 43*(8), 39.
Schuster, Gregory L, Dubovik, Oleg, & Holben, Brent N. (2006). Angstrom exponent and bimodal aerosol size distributions. *Journal of Geophysical Research: Atmospheres, 111*(D7).
Seedorf, Jens. (2004). An emission inventory of livestock-related bioaerosols for Lower Saxony, Germany. *Atmospheric Environment, 38*(38), 6565-6581.
Sem, Gilmore J. (2002). Design and performance characteristics of three continuous-flow condensation particle counters: a summary. *Atmospheric research, 62*(3-4), 267-294.
Senior, Constance L, Sarofim, Adel F, Zeng, Taofang, Helble, Joseph J, & Mamani-Paco, Ruben. (2000). Gas-phase transformations of mercury in coal-fired power plants. *Fuel Processing Technology, 63*(2-3), 197-213.
Shaman, Jeffrey, & Kohn, Melvin. (2009). Absolute humidity modulates influenza survival, transmission, and seasonality. *Proceedings of the National Academy of Sciences, 106*(9), 3243-3248.
Sherman, Laura S, Blum, Joel D, Keeler, Gerald J, Demers, Jason D, & Dvonch, J Timothy. (2011). Investigation of local mercury deposition from a coal-fired power plant using mercury isotopes. *Environmental Science & Technology, 46*(1), 382-390.
Srivastava, Ravi K, Hutson, Nick, Martin, Blair, Princiotta, Frank, & Staudt, James. (2006). Control of mercury emissions from coal-fired electric utility boilers: ACS Publications.
Steckel, Hartwig, & Eskandar, Fadi. (2003). Factors affecting aerosol performance during nebulization with jet and ultrasonic nebulizers. *European journal of pharmaceutical sciences, 19*(5), 443-455.
Stein, Michelle M, Hrusch, Cara L, Gozdz, Justyna, Igartua, Catherine, Pivniouk, Vadim, Murray, Sean E, . . . Metwali, Nervana. (2016). Innate immunity and asthma risk in Amish and Hutterite farm children. *New England Journal of Medicine, 375*(5), 411-421.
Stern, Jennifer E, Flagan, Richard C, Grosjean, Daniel, & Seinfeld, John H. (1987). Aerosol formation and growth in atmospheric aromatic hydrocarbon photooxidation. *Environmental science & technology, 21*(12), 1224-1231.
Stocker, Thomas F, Qin, D, Plattner, GK, Tignor, M, Allen, SK, Boschung, J, . . . Midgley, PM. (2013). Climate change 2013: the physical science basis. Intergovernmental panel on climate change, working group I contribution to the IPCC fifth assessment report (AR5). *New York*.
Stolle, Raik, Koeser, Heinz, & Gutberlet, Heinz. (2014). Oxidation and reduction of mercury by SCR DeNOx catalysts under flue gas conditions in coal fired power plants. *Applied Catalysis B: Environmental, 144*, 486-497.
Strivastava, Ravi. (2010). *Control of Mercury Emissions from Coal-fired Electric Utility Boilers: A Update*: National Risk Management Research Laboratory, Office of Research and Development, US Environmental Protection Agency.
Sui, Zifeng, Zhang, Yongsheng, Peng, Yue, Norris, Pauline, Cao, Yan, & Pan, Wei-Ping. (2016). Fine particulate matter emission and size distribution characteristics in an ultra-low emission power plant. *Fuel, 185*, 863-871.
Sun, Zhe, Wang, Juan, Bai, Xiaofei, Ji, Guobiao, Yan, He, Li, Yingying, . . . Li, Xiangdong. (2016). Pathogenicity comparison between highly pathogenic and NADC30-like porcine reproductive and respiratory syndrome virus. *Archives of virology, 161*(8), 2257-2261.

Swithenbank, JJMDSDGC, Beer, JM, Taylor, D, Abbot, D, & McCreath, GC. (1976). *A laser diagnostic technique for the measurement of droplet and particle size distribution.* Paper presented at the 14th Aerospace Sciences Meeting.

Szkarlat, Ann Cuneo, & Japar, Steven M. (1981). Light absorption by airborne aerosols: comparison of integrating plate and spectrophone techniques. *Applied optics, 20*(7), 1151-1155.

Szymanski, Wladyslaw W, & Wagner, Paul E. (1990). Absolute aerosol number concentration measurement by simultaneous observation of extinction and scattered light. *Journal of aerosol science, 21*(3), 441-451.

Tang, Joseph, Colacino, Joseph M, Larsen, Stephen H, & Spitzer, Wayne. (1990). Virucidal activity of hypericin against enveloped and non-enveloped DNA and RNA viruses. *Antiviral research, 13*(6), 313-325.

Tang, JW, Li, Y, Eames, I, Chan, PKS, & Ridgway, GL. (2006). Factors involved in the aerosol transmission of infection and control of ventilation in healthcare premises. *Journal of Hospital Infection, 64*(2), 100-114.

Tanré, D, Kaufman, YJ, Holben, BN e al, Chatenet, B, Karnieli, A, Lavenu, F, . . . Smirnov, A. (2001). Climatology of dust aerosol size distribution and optical properties derived from remotely sensed data in the solar spectrum. *Journal of Geophysical Research: Atmospheres, 106*(D16), 18205-18217.

Tavana, Hossein, Kuo, Chuan-Hsien, Lee, Qian Yi, Mosadegh, Bobak, Huh, Dongeun, Christensen, Paul J, . . . Takayama, Shuichi. (2009). Dynamics of liquid plugs of buffer and surfactant solutions in a micro-engineered pulmonary airway model. *Langmuir, 26*(5), 3744-3752.

Telis, VRN, Telis-Romero, J, Mazzotti, HB, & Gabas, AL. (2007). Viscosity of aqueous carbohydrate solutions at different temperatures and concentrations. *International Journal of food properties, 10*(1), 185-195.

Tellier, Raymond. (2006). Review of aerosol transmission of influenza A virus. *Emerging infectious diseases, 12*(11), 1657.

Thedell, Terry D, Mull, Judith C, & Olenchock, Stephen A. (1980). A brief report of gram-negative bacterial endotoxin levels in airborne and settled dusts in animal confinement buildings. *American journal of industrial medicine, 1*(1), 3-7.

Thomas, D, Contal, P, Renaudin, V, Penicot, P, Leclerc, D, & Vendel, J. (1999). Modelling pressure drop in HEPA filters during dynamic filtration. *Journal of Aerosol Science, 30*(2), 235-246.

Tian, Kegong, Yu, Xiuling, Zhao, Tiezhu, Feng, Youjun, Cao, Zhen, Wang, Chuanbin, . . . Tian, Xinsheng. (2007). Emergence of fatal PRRSV variants: unparalleled outbreaks of atypical PRRS in China and molecular dissection of the unique hallmark. *PloS one, 2*(6), e526.

Tseng, Chun-Chieh, & Li, Chih-Shan. (2006). Ozone for inactivation of aerosolized bacteriophages. *Aerosol science and technology, 40*(9), 683-689.

Tu, Xin, Gallon, Helen J, & Whitehead, J Christopher. (2011). Transition behavior of packed-bed dielectric barrier discharge in argon. *IEEE Transactions on Plasma Science, 39*(11), 2172-2173.

Turgeon, Nathalie, Toulouse, Marie-Josée, Martel, Bruno, Moineau, Sylvain, & Duchaine, Caroline. (2014). Comparison of five bacteriophages as models for viral aerosol studies. *Applied and environmental microbiology, 80*(14), 4242-4250.

Turpin, Barbara J, Huntzicker, James J, Larson, Susan M, & Cass, Glen R. (1991). Los Angeles summer midday particulate carbon: primary and secondary aerosol. *Environmental science & technology, 25*(10), 1788-1793.

UNEP. (2013). Sources, emissions, releases and environmental transport. *UNEP Chemicals Branch, Geneva, Switzerland, 42*.

USEPA. (2000). *Current Knowledge of Particulate Matter (PM) Continuous Emission Monitoring*. (EPA-454/R-00-039). Retrieved from https://www3.epa.gov/ttnemc01/cem/pmcemsknowfinalrep.pdf.

USEPA. (2003). *Air Pollution Control Technology Fact Sheet - Cyclones*. (EPA452/F-03-005). Retrieved from https://www3.epa.gov/ttncatc1/dir1/fcyclon.pdf.

USEPA. (2011). *Regulatory Impact Analysis for the Final Mercury and Air Toxics Standards*. (EPA-452/R-11-011). Research Triangle Park, NC: Retrieved from https://www3.epa.gov/ttnecas1/regdata/RIAs/matsriafinal.pdf.

USEPA. (2012). *Report to Congress on Black Carbon: Executive Summary*. (EPA-450/S-12-001). Retrieved from www.ccacoalition.org/en/file/869/download?token=u_JXzTM2.

USEPA (Producer). (2016). National Ambient Air Quality Standards (NAAQS) Table. Retrieved from https://www.epa.gov/criteria-air-pollutants/naaqs-table

USEPA. (2018). 2014 National Emissions Inventory (NEI) Data. https://www.epa.gov/air-emissions-inventories/2014-national-emissions-inventory-nei-data

Vázquez, Gonzalo, Alvarez, Estrella, & Navaza, José M. (1998). Density, viscosity, and surface tension of sodium carbonate+ sodium bicarbonate buffer solutions in the presence of glycerine, glucose, and sucrose from 25 to 40° C. *Journal of Chemical & Engineering Data, 43*(2), 128-132.

Vandenbroucke, Arne M, Morent, Rino, De Geyter, Nathalie, & Leys, Christophe. (2011). Non-thermal plasmas for non-catalytic and catalytic VOC abatement. *Journal of hazardous materials, 195*, 30-54.

Vaze, N.D., Arjunan, K.P., Gallagher, Jr., M.J., Vasilets, V.N., Gutsol, A.F., Fridman, A.A., & Anandan, S. (2007). *Air and water sterilization using non-thermal plasma.* Paper presented at the 16th IEEE International Pulsed Power Conference.

Vaze, Nachiket D, Arjunan, Krishna P, Gallagher, Michael J, Vasilets, Victor N, Gutsol, Alexander, Fridman, Alexander, & Anandan, Shivanthi. (2007). *Air and water sterilization using non-thermal plasma.* Paper presented at the Pulsed Power Conference, 2007 16th IEEE International.

Vaze, Nachiket D, Gallagher, Michael J, Park, Sin, Fridman, Gregory, Vasilets, Victor N, Gutsol, Alexander F, . . . Fridman, Alexander A. (2010). Inactivation of bacteria in flight by direct exposure to nonthermal plasma. *IEEE Transactions on Plasma Science, 38*(11), 3234-3240.

Vollenbroich, Dirk, Özel, Muhsin, Vater, Joachim, Kamp, Roza Maria, & Pauli, Georg. (1997). Mechanism of inactivation of enveloped viruses by the biosurfactant surfactin fromBacillus subtilis. *Biologicals, 25*(3), 289-297.

Wang, Fengyang, Wang, Shuxiao, Meng, Yang, Zhang, Lei, Wu, Qingru, & Hao, Jiming. (2016). Mechanisms and roles of fly ash compositions on the adsorption and oxidation of mercury in flue gas from coal combustion. *Fuel, 163*, 232-239.

Wang, Lingjuan, Buser, Michael D, Parnell, Calvin B, & Shaw, Bryan W. (2003). Effect of air density on cyclone performance and system design. *Transactions of the ASAE, 46*(4), 1193.

Wang, SX, & Hao, JM. (2012). Emissions of air pollutants from power plants in China: Tsinghua University, Beijing, China.
Wang, SX, Zhang, Lei, Li, GH, Wu, Y, Hao, JM, Pirrone, N, . . . Ancora, MP. (2010). Mercury emission and speciation of coal-fired power plants in China. *Atmospheric Chemistry and Physics, 10*(3), 1183-1192.
Watson, HE. (1908). A Note on the Variation of the Rate of Disinfection with Change in the Concentration of the Disinfectant. *The Journal of Hygiene, 8*. doi: doi:10.1017/s0022172400015
Weinstein, Robert A, Bridges, Carolyn Buxton, Kuehnert, Matthew J, & Hall, Caroline B. (2003). Transmission of influenza: implications for control in health care settings. *Clinical infectious diseases, 37*(8), 1094-1101.
Wheeler, SM, Ingraham, HS, Hollaender, Alexander, Lill, ND, Gershon-Cohen, Jacob, & Brown, EW. (1945). Ultra-violet light control of air-borne infections in a naval training center: preliminary report. *American Journal of Public Health and the Nations Health, 35*(5), 457-468.
White, WH, & Roberts, PT. (1977). On the nature and origins of visibility-reducing aerosols in the Los Angeles air basin. *Atmospheric Environment (1967), 11*(9), 803-812.
WHO. (2013). *Health effects of particulate matter. Policy implications for countries in eastern Europe, Caucasus and central Asia*. Copenhagen: Retrieved from http://www.euro.who.int/__data/assets/pdf_file/0006/189051/Health-effects-of-particulate-matter-final-Eng.pdf.
Woo, Myung-Heui, Hsu, Yu-Mei, Wu, Chang-Yu, Heimbuch, Brian, & Wander, Joseph. (2010). Method for contamination of filtering facepiece respirators by deposition of MS2 viral aerosols. *Journal of Aerosol Science, 41*(10), 944-952.
Wu, Qingru. (2018, May 22, 2018). *Evaluation of the effect of multiple air pollutants control in China's coal combustion units and future reduction recommendations.* Paper presented at the The 13th Mercury and Multi-Pollutant Emission from Coal, Krakow, Poland.
Wu, Yan, Liang, Yongdong, Wei, Kai, Li, Wei, Yao, Maosheng, Zhang, Jue, . . . Björkroth, J. (2015). MS2 Virus Inactivation by Atmospheric-Pressure Cold Plasma Using Different Gas Carriers and Power Levels. *Applied and Environmental Microbiology, 81*(3), 996-1002. doi: 10.1128/aem.03322-14
Wu, Ye, Wang, Shuxiao, Streets, David G, Hao, Jiming, Chan, Melissa, & Jiang, Jingkun. (2006). Trends in anthropogenic mercury emissions in China from 1995 to 2003. *Environmental science & technology, 40*(17), 5312-5318.
Wu, Zhijun, Zhu, Zhiyong, & Huang, Zhen. (2006). An experimental study on the spray structure of oxygenated fuel using laser-based visualization and particle image velocimetry. *Fuel, 85*(10-11), 1458-1464.
Xia, T., Kleinheksel, A., Wigginton, K.R., & Clack, H. L. (2018). Suspending Viruses in an Airstream Using a Consumer-grade Ultrasonic Humidifier. *Journal of Applied Microbiology, submitted, under review.*
Xiao, Gang, Xu, Weiping, Wu, Rongbing, Ni, Mingjiang, Du, Changming, Gao, Xiang, . . . Cen, Kefa. (2014). Non-thermal plasmas for VOCs abatement. *Plasma Chemistry and Plasma Processing, 34*(5), 1033-1065.
Xu, Peng, Kujundzic, Elmira, Peccia, Jordan, Schafer, Millie P, Moss, Gene, Hernandez, Mark, & Miller, Shelly L. (2005). Impact of environmental factors on efficacy of upper-room

air ultraviolet germicidal irradiation for inactivating airborne mycobacteria. *Environmental science & technology, 39*(24), 9656-9664.
Xu, Zheng, Xue, Likun, Wang, Tao, Xia, Tian, Gao, Yuan, Louie, Peter KK, & Luk, Connie WY. (2015). Measurements of peroxyacetyl nitrate at a background site in the Pearl River delta region: production efficiency and regional transport. *Aerosol and Air Quality Research, 15*(1), 833-841.
Yamamoto, Nobuto, Hiatt, CW, & Haller, Wolfgang. (1964). Mechanism of inactivation of bacteriophages by metals. *Biochimica et Biophysica Acta (BBA)-Specialized Section on Nucleic Acids and Related Subjects, 91*(2), 257-261.
Yamamoto, Toshiaki, & Sparks, Leslie E. (1986). Numerical simulation of three-dimensional tuft corona and electrohydrodynamics. *IEEE transactions on industry applications*(5), 880-885.
Yang, Linjun, Bao, Jingjing, Yan, Jinpei, Liu, Jinhui, Song, Shijuan, & Fan, Fengxian. (2010). Removal of fine particles in wet flue gas desulfurization system by heterogeneous condensation. *Chemical engineering journal, 156*(1), 25-32.
Yang, Yingju, Liu, Jing, Shen, Fenghua, Zhao, Lipeng, Wang, Zhen, & Long, Yan. (2016). Kinetic study of heterogeneous mercury oxidation by HCl on fly ash surface in coal-fired flue gas. *Combustion and Flame, 168*, 1-9.
Yehia, Ashraf, & Mizuno, Akira. (2013). Ozone generation by negative direct current corona discharges in dry air fed coaxial wire-cylinder reactors. *Journal of Applied Physics, 113*(18), 183301. doi: 10.1063/1.4804065
Yelverton, Tiffany LB, Hays, Michael D, Gullett, Brian K, & Linak, William P. (2014). Black carbon measurements of flame-generated soot as determined by optical, thermal-optical, direct absorption, and laser incandescence methods. *Environmental Engineering Science, 31*(4), 209-215.
Ylätalo, Sampo I, & Hautanen, Jukka. (1998). Electrostatic precipitator penetration function for pulverized coal combustion. *Aerosol science and technology, 29*(1), 17-30.
Yu, Ignatius TS, Li, Yuguo, Wong, Tze Wai, Tam, Wilson, Chan, Andy T, Lee, Joseph HW, . . . Ho, Tommy. (2004). Evidence of airborne transmission of the severe acute respiratory syndrome virus. *New England Journal of Medicine, 350*(17), 1731-1739.
Yule, AJ, Seng, C Ah, Felton, PG, Ungut, A, & Chigier, NA. (1982). A study of vaporizing fuel sprays by laser techniques. *Combustion and Flame, 44*(1-3), 71-84.
Zender, Charlie. (2008). Particle size distributions: theory and application to aerosols, clouds, and soils.
Zhang, Qi, Jimenez, JL, Canagaratna, MR, Allan, JD, Coe, H, Ulbrich, I, . . . Sun, YL. (2007). Ubiquity and dominance of oxygenated species in organic aerosols in anthropogenically-influenced Northern Hemisphere midlatitudes. *Geophysical Research Letters, 34*(13).
Zhang, Xinqiu, Turpin, Barbara J, McMurry, Peter H, Hering, Susanne V, & Stolzenburg, Mark R. (1994). Mie theory evaluation of species contributions to 1990 wintertime visibility reduction in the Grand Canyon. *Air & Waste, 44*(2), 153-162.
Zhang, Yi, Yang, Jianping, Yu, Xuehai, Sun, Ping, Zhao, Yongchun, Zhang, Junying, . . . Zheng, Chuguang. (2017). Migration and emission characteristics of Hg in coal-fired power plant of China with ultra low emission air pollution control devices. *Fuel Processing Technology, 158*, 272-280.

Zhang, Yu-yin, Yoshizaki, Takuo, & Nishida, Keiya. (2000). Imaging of droplets and vapor distributions in a Diesel fuel spray by means of a laser absorption–scattering technique. *Applied Optics, 39*(33), 6221-6229.

Zhao, Lin, & Adamiak, Kazimierz. (2008). Numerical simulation of the electrohydrodynamic flow in a single wire-plate electrostatic precipitator. *IEEE Transactions on Industry applications, 44*(3), 683-691.

Zhao, Pusheng, Zhang, Xiaoling, Xu, Xiaofeng, & Zhao, Xiujuan. (2011). Long-term visibility trends and characteristics in the region of Beijing, Tianjin, and Hebei, China. *Atmospheric Research, 101*(3), 711-718.

Zhao, XJ, Zhao, PS, Xu, J, Meng, W, Pu, WW, Dong, F, . . . Shi, QF. (2013). Analysis of a winter regional haze event and its formation mechanism in the North China Plain. *Atmospheric Chemistry and Physics, 13*(11), 5685-5696.

Zheng, Cheng-hang, Wang, Li, Zhang, Yong-xin, Weng, Wei-guo, Zhao, Hai-tao, Zhou, Jin-song, & Gao, Xiang. (2018). Co-benefit of hazardous trace elements capture in dust removal devices of ultra-low emission coal-fired power plants. *Journal of Zhejiang University-SCIENCE A, 19*(1), 68-79.

Zheng, Chenghang, Wang, Li, Zhang, Yongxin, Zhang, Jun, Zhao, Haitao, Zhou, Jinsong, . . . Cen, Kefa. (2017). Partitioning of hazardous trace elements among air pollution control devices in ultra-low-emission coal-fired power plants. *Energy & Fuels, 31*(6), 6334-6344.

Zhou, Hao, Zhou, Chuanlong, Lynam, Mary M, Dvonch, J Timothy, Barres, James A, Hopke, Philip K, . . . Holsen, Thomas M. (2017). Atmospheric mercury temporal trends in the northeastern United States from 1992 to 2014: are measured concentrations responding to decreasing regional emissions? *Environmental Science & Technology Letters, 4*(3), 91-97.

Zhou, Jinsong, Luo, Zhongyang, Zhu, Yanqun, & Fang, Mengxiang. (2013). *Mercury emission and its control in chinese coal-fired power plants*: Springer.

Zhou, Lei, Wang, Zichun, Ding, Yuping, Ge, Xinna, Guo, Xin, & Yang, Hanchun. (2015). NADC30-like strain of porcine reproductive and respiratory syndrome virus, China. *Emerging infectious diseases, 21*(12), 2256.

Zhou, Lei, & Yang, Hanchun. (2010). Porcine reproductive and respiratory syndrome in China. *Virus research, 154*(1-2), 31-37.

Zhou, Y-J, Hao, X-F, Tian, Z-J, Tong, G-Z, Yoo, D, An, T-Q, . . . Wei, T-C. (2008). Highly virulent porcine reproductive and respiratory syndrome virus emerged in China. *Transboundary and emerging diseases, 55*(3-4), 152-164.

Zhou, Zi-Jian, Liu, Xiao-Wei, Zhao, Bo, Chen, Zhen-Guo, Shao, Hai-Zhong, Wang, Le-Le, & Xu, Ming-Hou. (2015). Effects of existing energy saving and air pollution control devices on mercury removal in coal-fired power plants. *Fuel Processing Technology, 131*, 99-108.

Zhu, Chuanyong, Tian, Hezhong, Cheng, Ke, Liu, Kaiyun, Wang, Kun, Hua, Shenbing, . . . Zhou, Junrui. (2016). Potentials of whole process control of heavy metals emissions from coal-fired power plants in China. *Journal of Cleaner Production, 114*, 343-351.

Zhuang, Ye, Kim, Yong Jin, Lee, Tai Gyu, & Biswas, Pratim. (2000). Experimental and theoretical studies of ultra-fine particle behavior in electrostatic precipitators. *Journal of electrostatics, 48*(3-4), 245-260.